

Electronic Thesis and Dissertation Repository

8-19-2020 2:00 PM

Electromagnetic Metasurface Fabricated by Printed Electronics and Its Applications

Jishu Gao, *The University of Western Ontario*

Supervisor: Jun Yang, *The University of Western Ontario*

A thesis submitted in partial fulfillment of the requirements for the Master of Engineering Science degree in Mechanical and Materials Engineering

© Jishu Gao 2020

Follow this and additional works at: <https://ir.lib.uwo.ca/etd>

Recommended Citation

Gao, Jishu, "Electromagnetic Metasurface Fabricated by Printed Electronics and Its Applications" (2020). *Electronic Thesis and Dissertation Repository*. 7178.
<https://ir.lib.uwo.ca/etd/7178>

This Dissertation/Thesis is brought to you for free and open access by Scholarship@Western. It has been accepted for inclusion in Electronic Thesis and Dissertation Repository by an authorized administrator of Scholarship@Western. For more information, please contact wlsadmin@uwo.ca.

Abstract

Recently, metasurface plays significant roles in manipulation of electromagnetic waves. The main fabrication methods are MEMS (Microelectromechanical systems) technology and PCB (Printed circuit board) technology. Both methods face the challenges of complex fabrication processes, high cost, and severe pollution. In this thesis, the digitalized reaction on demand (DRoD) method, as a new printed electronic technology, was proposed to address the problems. In this method, the substrate was coated by PVA and nanoparticle composite to form a mesoporous ink absorption layer, followed by reduction functionalization. A novel silver ink was formulated to solve the problems of low conductivity, nozzle blocking, and complex preparing processing. As a demonstration, EM metasurface was fabricated via digitally and precisely control of silver reduction reaction. Moreover, a roll to roll process of metasurface printing via DRoD method was demonstrated. The developed technology provides a solution to produce metasurface with low cost, high quality, and large scale.

Keywords

Printed electronic, metasurface, low-cost fabrication, conductive ink, roll to roll process

Summary for Lay Audience

Electromagnetic (EM) wave is the fundamental element in the modern society. The manipulation of the EM wave, mainly including selective absorption and reflection, will play an essential role in the development of many applications, like high-frequency communication, Internet of Things, and human-machine interface. The metasurface is the artificial structure with the period patterns. The manipulation of the EM wave via metasurface is realized by the resonance frequency of metasurface. The performance of the manipulation performance of the metasurface is greatly affected by the manufacturing process. The MEMS (Microelectromechanical systems) technology and PCB (Printed circuit board) technology take the dominate position for the fabrication of the metasurface. MEMS technology requires complex fabrication processes, expensive equipment, and long preparation period. PCB technology has the limitation of low flexibility and high pollution in the whole fabrication process. To solve the problems above, a new printed electronics technology, digitalized reaction on demand (DRoD) method, was proposed and demonstrated. In the DRoD method, the substrate was treated to form a mesoporous ink absorption layer in the first step. Then, the reduction coating layer functionalized the substrate via Mayer rod coating. High concentration silver salt ink was formulated to simplify the preparation process, reducing the production cost, and avoiding pollution. Inkjet printing was applied to form the metasurface with high conductivity by the digitally controlled *in situ* reduction reaction of silver salt ink. Such an approach shows great potential in the roll to roll production process. The primary step of the roll to roll printing system was realized, and a novel system for the roll to roll printing based DRoD method was designed. The developed technology in this thesis provides a creative way to produce metasurface with high efficiency, low cost, high quality, and large scale.

Co-Authorship Statement

This master thesis has been prepared according to the regulations for an integrated article format thesis stipulated by the Faculty of Graduate and Postdoctoral Studies at the University of Western Ontario and has been co-authored as follows:

Chapter 2: Numerical study of metasurface

All the numerical studies in chapter 2 were finished by Jishu Gao. Dr. Xiaobing Cai and Dr. Dongxing Zhang provide beneficial discussion. Dr. Xiaobing Cai helped to revise the manuscript.

Chapter 3: Fabrication of metasurface with printing electronics

All the experiments and analyses are conducted by Jishu Gao. Dr. Tengyuan Zhang supported the experiment design. Dr. Yang and Dr. Qiuquan Guo provided beneficial suggestions in the revising process.

Chapter 4: Performance and extended application of printed metasurface

All the theoretical analysis was conducted by Jishu Gao. All the experiments were conducted by Jishu Gao with the assistance of Bei Ouyang. Dr. Dongxing Zhang offered supports in the setting up of the testing equipment.

Acknowledgments

First of all, I have to show my appreciation to my supervisor, Prof. Jun Yang. He gave me great support during my master's stage. He created a warm group where we can always get help from each other and have beneficial discussions. I also learned how to improve myself from Dr. Yang. He can always point out my mistake and give me suggestions about how to improve my research. All the suggestions mean a lot for me. I got encouragement from him and I will keep working with his great guide.

Dr. Xiaobing Cai, Dr. Tengyuan Zhang and Dr. Dongxing Zhang helped me during my whole research process. I received many suggestions from them, including experiment plan and results discussion. It is my honor to learn and work with them. I would also thank to Yiyuan Zhang, Busheng Zhang and Junfeng Xiao. We spent long time together in the lab and office.

Thanks to my teammates, classmates and friends in London. It is my great experience to learn, research and live in this beautiful city. I feel relaxed to live here. All the projects, assignments, and activity add colors to my life.

Last but no least, I would say "thanks" to my families. My mom and dad always believe in me and encourage me to pursue my goals. Without them, I can't be here.

Table of Contents

Abstract.....	ii
Summary for Lay Audience.....	iii
Co-Authorship Statement.....	iv
Acknowledgments.....	v
Table of Contents.....	vi
List of Tables.....	ix
List of Figures.....	x
Chapter 1.....	1
1. Introduction.....	1
1.1 Introduction of printed electronics.....	1
1.2 Introduction of Electromagnetic (EM) metasurface.....	7
1.3 Application of Electromagnetic Metasurface.....	9
1.3.1 Application of metasurface in EM wave selective reflection.....	9
1.3.2 Application of metasurface in EM wave absorption.....	16
1.4 Fabrication of Electromagnetic Metasurface.....	24
1.5 Research Objective.....	26
Chapter 2.....	27
2. Numerical Study of Metasurface.....	27
2.1 Design of EM wave selective absorption metasurface.....	27
2.2 Parameters optimization of metasurface absorber.....	29
2.2.1 Optimization of the square width.....	29
2.2.2 Optimization of the metasurface thickness.....	30
2.2.3 Optimization of the conductivity.....	32
2.3 Numerical study of EM wave selective reflection metasurface.....	34

2.3.1	The design of the EM wave selective reflection metasurface.....	34
2.3.2	The simulation results as PCE	37
2.3.3	The influence of conductivity	38
2.3.4	The influence of roughness	39
2.3.5	The Influence of the thickness	41
Chapter 3	42
3.	Fabrication of metasurface with printing electronics.....	42
3.1	Fabrication of EM wave selective reflection metasurface via DRoD method.....	43
3.1.1	Preparing of the ink absorption layer.....	44
3.1.2	Preparing of the reduction functional layer	45
3.1.3	Printing of the Ag salt ink.....	48
3.2	Printing results and characterization	50
3.2.1	Measurement of conductivity	56
3.2.2	The influence of Ag loading on the conductivity	57
3.2.3	The influence of Vc concentration.....	60
3.2.4	The influence of the ink absorption layer	61
3.2.5	Modification of the silver ink	63
3.2.6	Stability of the printed metasurface	64
3.2.7	Demonstration of the roll to roll printing based on DRoD method	69
3.3	Fabrication of metasurface EM wave absorber with 3D printing	72
3.3.1	Preparing of conductive PLA.....	72
3.3.2	Printing of conductive PLA	73
3.3.3	Printed Metasurface EM wave absorber	74
Chapter 4	76
4.	Performance and extended application of printed metasurface	76
4.1	Measurement of EM wave selective reflection metasurface	76

4.1.1	Measurement setup	76
4.1.2	EM wave selective reflection performance of the printed metasurface....	78
4.2	Applications of metasurface on food safety.....	81
Chapter 5	86
5	Summary and perspective	86
5.1	Thesis summary	86
5.2	Perspective	88
Reference	89
Curriculum Vitae	96

List of Tables

Table 1 Parameter of the Mayer rod used in coating	47
Table 2 Basic parameters of the printed metasurface	52
Table 3 Influence of the solid content on the printing results.....	62
Table 4 The parameters of the high loading silver ink	63
Table 5 Conductivity during water treatment test.....	67
Table 6 Conductivity during steam bath test	68
Table 7 Specific parameter of the horn antenna @Ta =25 °C	77

List of Figures

Figure 1 (a) Flexible electronics pressure sensor with resistance layer, posts and electrodes produced by screen printing. (b) Flexible pressure sensor with bump structures on the top film (Reprint from[9] with permission).	2
Figure 2 Schematic of Piezoelectric Drop-on-demand inkjet printer (Reprint from Ref. [10] with permission).....	3
Figure 3 (a) Configuration of “bottom-gate” and “top-contact” structure of a ZnO-NPs TFT with the polymer gate dielectric. (b) TFT device with inkjet printed polymer insulator(Reprint from Ref. [13] with permission).	4
Figure 4 3D printed QD-LEDs. (A) Direct 3D printing of QD-LEDs on a curve substrate. (B) Structure and components of QD-LED (Reprint from Ref.[21] with permission).	6
Figure 5 Four classical types of EM filter metasurface. (a) Band stop (b)Band pass (c)Low pass (d) High pass. The brown color stands for conductive part (Reprint from Ref.[34] with permission).....	10
Figure 6 Configuration of the metasurface, (a) 3-D view, (b) the metallic ring unit cell, (c) the middle metallic layer unit cell (Reprint from Ref. [33] with permission).	11
Figure 7 (a) Equivalent circuit model of the proposed metasurface (bandpass filter). (b) Equivalent circuit model of the top and bottom metallic layers. (c) Equivalent circuit model of the middle metallic layer (Reprint from [33] with permission).....	11
Figure 8 Transmission coefficients comparison of full-wave simulation, equivalent circuit model, and free space measurement. ($f_{z1}-f_{z3}$: the frequency values when S_{21} comes to minimum. $f_{p1}-f_{p2}$: the frequency values when S_{21} comes to the maximum. Reprint from [33] with permission).....	12
Figure 9 (a) Geometry of the designed metasurface. (b) Measured and simulated performance of the printed metasurface (Reprint from [35] with permission).	14

Figure 10 Measured transmission of printed metasurface on tattoo and PEL paper sintered by thermal, photonic, and plasma means(Reprint from [36] with permission). 15

Figure 11 The general processes of an incident EM wave through an EM absorber. 16

Figure 12 Structure, simulation and performance of a classical metasurface EM wave absorber. (a) Electric resonator and (b) cut wire. The unit cell is shown in (c) with axes indicating the propagation direction. (d) shows the simulated (red) and measured (blue) lines. The dashed line is a Gaussian weighted average which approximates assembly error. The inset shows the simulated angular dependence of the $A(\omega)$ at ω_{\max} (Reprint from Ref.[38] with permission)..... 18

Figure 13 Unit cell design of the metasurface absorber. A square array of cross and cylinder with 16 resonant elements: $l_1 = 200$ nm, $l_2 = 180$ nm, $l_3 = 160$ nm and $l_4 = 140$ nm; $w = 50$ nm; $d_1 = 140$ nm, $d_2 = 120$ nm, $d_3 = 100$ nm and $d_4 = 50$ nm (Reprint from [39] with permission). 19

Figure 14 (a) SEM image of the fabricated metasurface absorber. The inset represents an expanded view of the unit cell. (b) Experimentally measured extinction for s- and p-polarizations at a 20° angle of incidence. Inset to (b) is a comparison of results between experiments and simulations (Reprint from [39] with permission). 20

Figure 15 Structure design of the 3D metasurface absorber. (a) Unit cell diagram. (b) View of the unit cell in the plane of x-z and x-y. (c) Honeycomb sample for compressive test and (d) sample of the 3D metasurface (Reprint from Ref.[40] with permission). 21

Figure 16 Simulation and experiment results of reflectivity for vertical incident waves (Reprint from [40] with permission). 21

Figure 17 (a) Unit cell schematic of the proposed metasurface EM wave absorber. (b) Flow diagram of the laser ablation process (Reprint from Ref. [41] with permission). 22

Figure 18 (a)Fabricated sample of the proposed dual-band flexible metasurface absorber. (b) Simulated and measured absorption properties of the dual-band flexible metasurface absorber(Reprint from [41] with permission). 23

Figure 19 (a) Unit cell for the metasurface absorber in snake structure and (b) photo of the fabricated sample. (c) The flexibility of the Metasurface absorber. (d) measure absorption by the length, m (Reprint from Ref.[42] with permission).....	23
Figure 20 Printed Circuit Board Working flow (Reprint from GESP Technology).....	24
Figure 21 Metasurface EM wave absorber. Top(b) and side(c) view of the unit cell.	28
Figure 22 Simulation results of absorption efficiency with 0.7-0.95 mm width change.....	29
Figure 23 The influence of the thickness on the absorption efficiency.	30
Figure 24 Simulation results of electric field distribution on metasurface with different sizes. (a) d=0.3 mm (b) d=0.7 mm.	31
Figure 25 Simulation results of the absorption efficiency at the resonating frequency with conductivity range from 10-950 S/m.	32
Figure 26 Optimization of the conductivity from 250 to 340 S/m.	33
Figure 27 Illustration of the metasurface (a). The unit cell structure of the period metasurface(b). Side view of the unit cell structure(c). Transparent metasurface with metalize surface structure (d).	35
Figure 28 Simulated transmission efficiency (S_{21}) of the PCE based metasurface.	37
Figure 29 S_{21} curves of the metasurface under different conductivity	38
Figure 30 Simplification of the roughness of metasurface. (a) no roughness. (b) slight roughness. (c) high roughness.....	39
Figure 31 The influence of the roughness on the transmission performance of the metasurface.	40
Figure 32 The influence of thickness on the transmission performance of the metasurface..	41
Figure 33 Schematic of Mayer rod coating.....	44

Figure 34 Mayer rod coating machine (TMAX-XT-200CA, Xiamen Tmax Battery Equipment Limited).....	45
Figure 35 Wet film of the Vc coating with the mirror-like surface.....	46
Figure 36 Xanthan gum solution.....	47
Figure 37 Vortex mixer from VWR (left) and prepared AgNO ₃ ink (right).	48
Figure 38 Ink cartridge from Epson. 59 nozzles are integrated into color print head. The black print head has 180 nozzles.	49
Figure 39 Epson C88+ printer.	50
Figure 40 Printed metasurface on transparent PET substrate	51
Figure 41 Printed metasurface on the paper substrate	51
Figure 42 Printed metasurface structure and conductivity test unit on the silicon rubber substrate.	52
Figure 43 Optical microscopy image of printed metasurface unit cell.....	53
Figure 44 SEM images of the surface morphology of silver flake on PET substrate.....	54
Figure 45 SEM images of the surface morphology of silver flake on paper substrate.....	54
Figure 46 SEM image of the cross-section of the silver-polymer layer, which has the thickness of ~4.5 μm.....	55
Figure 47 Model 2450 SourceMeter SMU Instrument with the Lucas/Signatone Corporation (Gilroy, CA), Model SP4 4-Point Probe Head and S-302 Test Stand measuring the conductivity of a sample.	56
Figure 48 The influence of the Ag ink concentration on the conductivity of the metasurface.	57

Figure 49 Surface morphology of the metasurface when silver nitrate concentration is 0.1 g/ml.	58
Figure 50 Surface morphology of the metasurface when silver nitrate concentration is 0.8 g/ml.	58
Figure 51 Surface morphology of the metasurface when silver nitrate concentration is 1.2 g/ml.	59
Figure 52 The influence of the Vc concentration on the conductivity of the metasurface.	60
Figure 53 Surface crack induced by the high silica content after solvent evaporation.	61
Figure 54 Improved surface morphology after the adjustment of the content of silica nanoparticles.	62
Figure 55 Conductivity of the printed metasurface stored in ambient condition.	64
Figure 56 X-ray diffraction (XRD) spectra of a) freshly prepared sample; b) after stored in air for 180 d (Reprint from [62] with permission).	65
Figure 57 SEM image of the metasurface unit cell after water treatment.	66
Figure 58 Silver nanoparticle generated after water treatment.	67
Figure 59 Surface morphology of the metasurface after the steam bath.	68
Figure 60 Demonstration of the R2R process for the DRoD method.	70
Figure 61 Roll sample of metasurface fabricated by the roll to roll process of DRoD method.	70
Figure 62 Surface morphology of the roll to roll printed metasurface sample.	71
Figure 63 Noztek Pro filament Extruder.	72
Figure 64 Prepared conductive PLA filament.	73
Figure 65 Printing process of Ender 3Pro desktop 3D printer.	73

Figure 66 (a) 3D model and (b) printed metasurface EM wave absorber.	74
Figure 67 Measurement setup for the metasurface, including Agilent 8722ES vector network analyzer and a pair of the horn antenna.	76
Figure 68 Radiation pattern in both E-plane and H-plane at 27.35 GHz.....	77
Figure 69 Comparison of S_{21} curve between the DRoD made sample, PCB made sample and simulation.....	78
Figure 70 Comparison of S_{21} curve between size modified DRoD made sample, PCB made sample and simulation.....	79
Figure 71 Comparison of S_{21} curve of size modified DRoD made sample before and after water treatment.....	80
Figure 72 Materials used in the test: (a) rice; (b) soft wheat; (c) food container; (d) metasurface.	82
Figure 73 Resonance frequency shift for rice with the water content (up) and the S_{21} parameter when 0 ml water was added (down).	83
Figure 74 Resonance frequency shift for soft wheat with the water content (up) and the S_{21} parameter when 10 ml water was added (down).	84
Figure 75 Roll to roll printing system based on DRoD method.	88

Chapter 1

1. Introduction

1.1 Introduction of printed electronics

Printed electronics is a rising technology since the end of the last century[1]. It is now a hot topic in both industry and academia society. Generally, printed electronics means the fabrication of electronic devices or electronic components via modern printing technology[2]. Compared with traditional silicon-based electronic technology, the printed electronic technology owns many advantages, including but not limited to the faster fabrication process, lower cost, eco-friendly, and a wide range of materials choices[3]. The combination of functional polymers and inorganic materials with modern printing technologies makes high performance, thin, low density, and cost-efficient flexible electronic systems possible[4]. Flexible printed electronics will take the dominate position in the whole market of printing electronics for their advantages like wider application area, better consumer experience, suitable for larger-scale production like roll to roll printing[5].

The printed electronics can be divided into three key components: functional ink, substrate, and printing method. Generally, there are two major approaches divided by the method to transfer ink to the substrate as contact and non-contact printing. In the contact printing process, printed structures were obtained by the physical contact of inked pattern surfaces with the substrate[6]. In a non-contact printing process, functional ink was dispensed through nozzles or openings and printed structures were printed by moving the substrate or printing head in a pre-programmed pattern[7]. Contact printing technologies include gravure printing, gravure-offset printing, and flexographic printing. The non-contact printing techniques main include slot-die coating, inkjet printing, and rotary screen-printing. Compared with the contact printing, the non-contact printing techniques received greater attractions in the printing electronics industry due to their advantages like simplicity, affordability, rapid working flow, adaptability to the fabrication process, few material wastages, and higher resolution of patterns[8].

Screen-printing is a popular and mature technology for printed electronics, especially to print metallic interconnection in the sensors and other electronic devices (shown in **Figure 1 (a)**)[9]. The screen printer is setting up with the screen, squeegee, press bed, and substrate. For the rotary screen printing system, the squeegee and ink are placed inside the tube and the web of the screen is folded, which can perform continuous printing process (**Figure 1 (b)**). The rotary screen printing can achieve a high speed, but the cost of rotary setup is high and the clean and maintenance is difficult. The high viscosity requirement for the ink limits the materials selections for future electronic devices. The expensive screen mask can only be used to print one specific pattern, which restricts the flexibility of the design process.

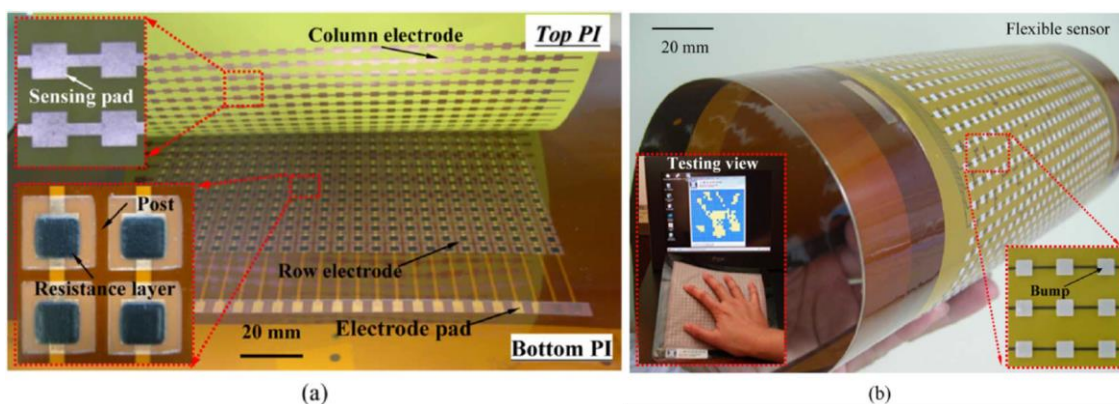


Figure 1 (a) Flexible electronics pressure sensor with resistance layer, posts and electrodes produced by screen printing. (b) Flexible pressure sensor with bump structures on the top film (Reprint from[9] with permission).

Inkjet printing is a rising technique for direct depositing solution-based materials with the digitalized pattern. The emerging of the inkjet printing breaks up many limitations of screen printing and some other traditional non-contact printing technologies, offers new solutions to many novel printing applications.

Inkjet technology was developed since the end of the nineteenth century. In 1833, Felix Savart started the liquid jet system governed by the laws of fluid dynamics[10]. Lord Rayleigh and Weber analyzed the droplet formation of inviscid and viscous liquid and built the model of a transient pressure pulse to the nozzle[11]. With above theoretical support,

the first commercial inkjet device was produced in 1951. Continuous Inkjet (CIJ) is the domain technology in the last century. In the CIJ system, the stream was induced by the applied force to break up liquid jet into a series of droplets with uniform size and spacing. The disadvantages of the system are complexity and a short lifetime. Drop-on-demand (DOD) inkjet printing was then developed. In this printing technology, droplets are formed and ejected with demand. The piezoelectric DOD printing system, shown in **Figure 2**, can meet the development of digitalization, elongate the system lifetime and save ink, which leads inkjet printing to become the most important printing technique in the publishing and graphics industry. Combined with hydrophobic surface treatments, the feature sizes of 5 μm can be realized with high-resolution piezoelectric DOD inkjet printing head[12]. More advanced print head or nozzle are designed to meet the need of novel printing materials, like quantum dots ink, which needs precise volume control in the whole printing process. Based on the advanced inkjet printing technology, thin-film transistor (TFT), was successfully realized with the cooperation of some vacuum processes, like sputtering or evaporation(**Figure 3**)[13].

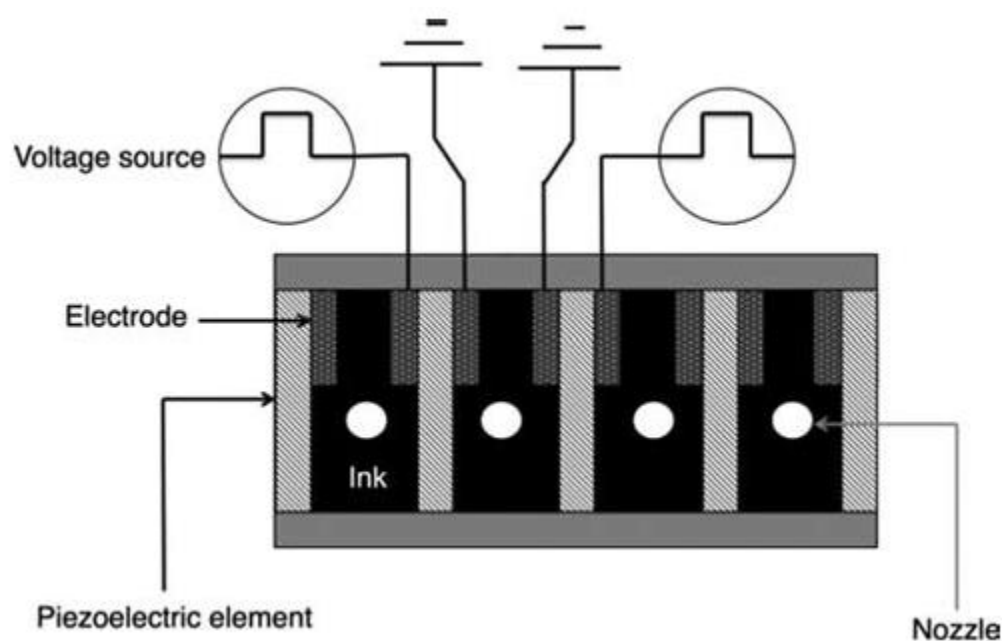


Figure 2 Schematic of Piezoelectric Drop-on-demand inkjet printer (Reprint from Ref. [10] with permission).

The rapid developments printed electronics is promoted by two driven forces: the mature of the printing technology and the development of the materials research. With the raising of nanomaterials like metal nanoparticles, carbon nanotubes, graphene, nanowire and other materials with special nanostructure, the choices of conductive ink are greatly expanded. Due to their ultra-high conductivity, it is promising to apply them to advanced electronic devices. The main types of conductive inks include colloidal suspensions of nanoparticles, organometallic compounds in solution, conductive polymers and novel nanomaterials ink. In order to make a useful ink formulation, many issues need to be considered, include printability, adhesion to the substrates, resolution, printer maintenance, cost and stability. For the printability, the viscosity, surface tension, and wettability are the main concern. The particle concentration and solvent system are critical for proper ejection to avoid blocking the nozzle.

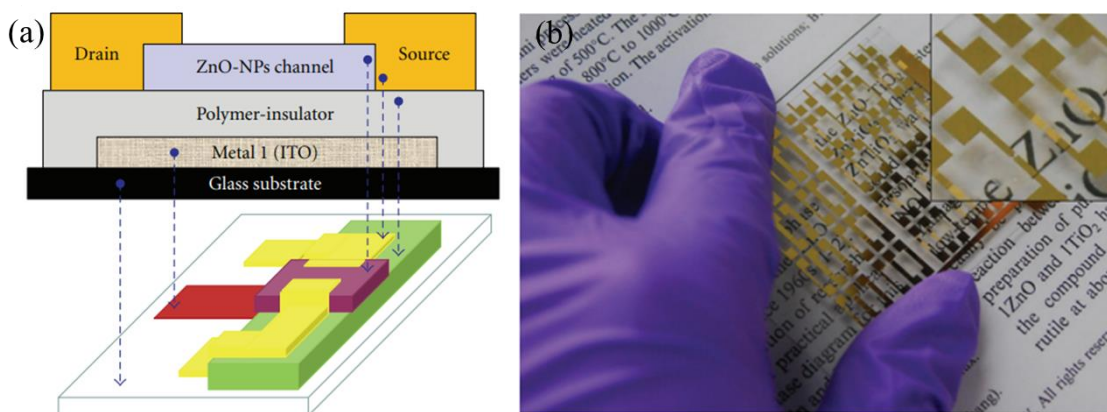


Figure 3 (a) Configuration of “bottom-gate” and “top-contact” structure of a ZnO-NPs TFT with the polymer gate dielectric. (b) TFT device with inkjet printed polymer insulator(Reprint from Ref. [13] with permission).

Direct writing technology was developed to provide an effective method to fabricate the flexible electronics circuit with the advantages of simple operation, low cost and high portability[14]. There are many choices of writing tools, like ball pen[15], marker pen[16], fountain pen[17], even brush pen[18], which provide broad access for direct writing technology. Due to the natural properties pen writing, all the ink can be transferred to the substrate, generate the pattern as desired. Conductive metal nanoparticle ink took the

domination position in direct pen writing. However, the hand-controlled in-situ reduction reaction was realized by direct writing of metal salt ink on the reduced functional substrate[19]. It is significant to improve the conductivity through increase the metal loading in ink. Compared with the traditional direct pen writing technology, the ink preparation is simple and no post-treatment process was needed. To overcome the limitation of low resolution, the digitalization system with precise physical control can be induced.

3D printing is a highly digitalized method in the printed electronics area. The mechanism of 3D printing is to physicalize the output files from computer-aided design software into tangible objects using pattern-generating tools that move along multiple directions[20]. These tools can be light sources that solidify resins or fuse powders, or nozzles that deposit materials directly. Some 3D structure electronic systems were fabricated via 3D printing. Quantum-dot-based LEDs (QD-LEDs) were printed on the curve surface and integrated arrays of the diodes in 3D matrices by the 3D-printing method based on extruding various materials (**Figure 4**)[21]. A highly stretchable sensor was created by 3D printing of a carbon-based resistive ink embedded within an elastomeric matrix[22]. This new method was designed to extrude viscoelastic inks through nozzles directly into an elastomeric reservoir. The ink forms a resistive sensing unit, while the reservoir turns into a matrix material. Based on the cases above, the development of extrusion modeling technology offers great potential to fabricate electronics devices or functional structures.

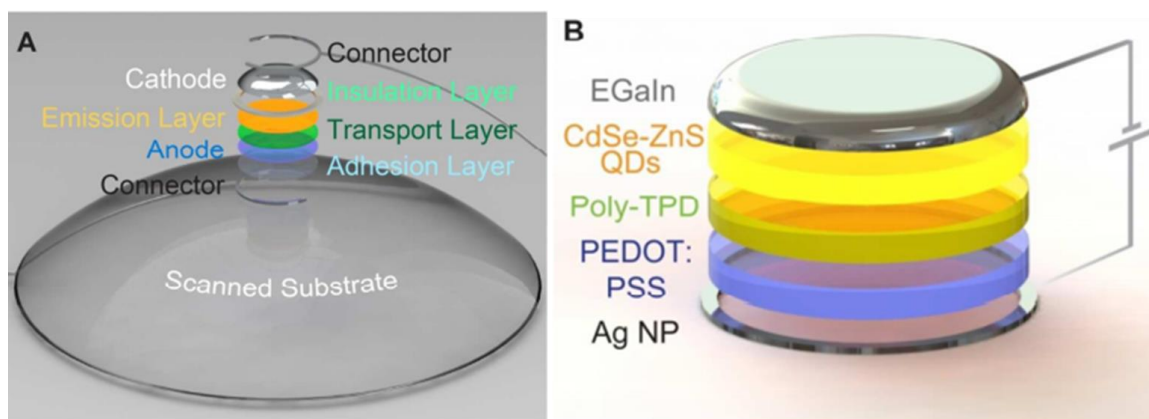


Figure 4 3D printed QD-LEDs. (A) Direct 3D printing of QD-LEDs on a curve substrate. (B) Structure and components of QD-LED (Reprint from Ref.[21] with permission).

More advanced printing technologies will be developed to meet the new opportunity and challenges of the printing electronics industry. Lots of functional materials showed their potential in future electronic applications, like quantum dot, graphene and carbon nanotube due to their special light, electric or mechanical properties. Printing technology can lead the functional materials to show their function at the device level.

To further extend the application of printing electronics, some issues need to be solved. First, the conductivity of the printed sample should be controllable to meet the more precise division of applications. Second, the cost of conductive ink is still high due to the complex formulating process. Third, the requirement of printing patterns with the finer feature is rising. Strategy innovation, including the ink formulation innovation and printing process innovation need to be combined to achieve better performance of printed electronics devices.

1.2 Introduction of Electromagnetic (EM) metasurface

Owing to the high digitalization and rapid prototyping capability, printing electronics technology is gradually applied in the research and development of the metasurface. The metasurface is built with periodic subwavelength metal/dielectric artificial structures that resonantly couple to the electric and/or magnetic components of the incident electromagnetic fields, exhibiting super nature properties. The metasurface is becoming a hot research topic in recent 20 years due to its potential in the application of cloaking[23], controlling propagation behavior of EM waves[24], sensing, superlens and negative and zero refraction areas[25][26].

The research of metasurface started in 1902 when Robert Wood was exploring the reflection spectra of subwavelength metallic grating[27]. He noticed that when light is incident from the normal side, a small change of wavelength, like $1/1000$ of wavelength, can cause the illumination in the spectrum to change from a maximum to almost zero. Traditional diffraction grating theory at that time was hard to explain such a phenomenon. Such a phenomenon was named “Wood’s anomaly”. After then, he found that the occurrence of unexpected narrow bright and dark bands was dependent on the polarization of the incident light. In the same year, Levi-Civita proposed the boundary relations for a metallic sheet with thin thickness. The resonance effect was present to explain the Wood’s anomaly later by A. Hessel and A. Oliner. They led the discovery of the scattering by periodically modulating reactance surfaces in 1965[28]. Periodically modulate reactance surfaces is a planar surface which presents an idealization of a variety of scattering structures. They include metallic reflection gratings with different depth of grooves, dielectric-coated metallic gratings with different dielectric constant, periodically grooved dielectric layers structures, and so on. From the experiment results, the wave frequency, angle of incidence, position on the surface, etc., as variables of the surface, can lead the difference of the reactance of the surface, which we call it surface impedance. It is the specific characteristic of the surface structures. Surface impedance analysis of the periodic structure contributed to clarify the nature of the resonance anomalies and then promote the development of metasurface with complex structures.

A. Hessel and A. Oliner revealed that that surface impedance $Z^S(x)$ is a periodic reactance function which we shall assume to be representable within a given period d by the Fourier series expansion[28]:

$$Z^S(x) = \sum_{v=-\infty}^{\infty} Z_v^S e^{i\left(\frac{2\pi}{d}\right)vx} \quad (1)$$

It is valid for most of the period structures, such as grooved gratings fabricated by metal or dielectric.

The numerical study was widely used in the study of the metasurface based on the research of approximate boundary conditions with the work of T. Senior in 1981[29]. In his review, he stated the conditions, criteria, and validity of the simulation of materials and surfaces systematically. More metasurface phenomena can be explained in a theoretical way.

The model of the metasurface is becoming more and more complex nowadays. The finite element method (FEM) is applied for solving partial differential equations in two or three space variables in the propagation of the EM wave in the interface of the metasurface. The FEM subdivides a large and complex system into many smaller, simpler parts that are called finite elements. It shows a significant advantage in the metasurface's period structure. The simplification is achieved by a particular space discretization in the space dimensions, which can be realized via forming mesh for the object. The mesh means the numerical domain for the solution, which has a finite number of points. The simple equations that model these finite elements are calculated and then assembled into a more extensive system of equations or matrix that standard for the entire problem.

COMSOL Multiphysics is a widely used platform of finite element analysis, solver, and multi-physics simulation. The study of the metasurface is an important part of the radio frequency module of COMSOL. In this thesis, COMSOL was used to design the metasurface and simulate the physical process.

1.3 Application of Electromagnetic Metasurface

Many applications inspired by metasurface have been developed, such as microstrip transmission line, microstrip antenna[30], frequency selective surface, polarization manipulator and optical vortex[31], which have been used in designing of cutting edge equipment and also in daily life. In this thesis, we focus on the application of EM wave manipulation, including the EM wave selective reflection and absorption.

1.3.1 Application of metasurface in EM wave selective reflection

EM wave selective reflection can be applied in future communication technology. In the incoming industry 4.0 era, large-scale machine to machine connection, brain to machine communication will be realized, which can reshape the production and living style. The future communication technology provides high-capacity and high-rate data transmissions, thus supporting a variety of devices and services interaction. IoT (Internet of Things) technology is a basic component of Industry 4.0 society and based on strong communication technology[32]. IoT technology pushes the development of advanced antenna radomes with a wide passband, low insertion loss, high selectivity, and sufficient signal shielding outside the working band[33]. One of the critical issues is the near-field electromagnetic interference (EMI) at the working frequency band.

The EM metasurface can be applied to solve the above problem. The EM metasurface will interact with the incident wave during the propagation from different angles. The unit cell of the periodic structure of the metasurface can be regarded as the dipole element. The dipole element will resonate when the half wavelength of the incident wave equal to the length of the dipole element. The dipole array can be divided into the active array and passive array with the difference of excitation mode. For passive array, it is excited by the energy of the incident wave. And for the active array, individual generator active the whole structure. For each configuration of the EM metasurface, a resonance frequency can be determined. Such a frequency can be called as the characteristic frequency for the EM metasurface. Due to the EM wave selectivity property given by the resonance frequency, EM metasurface can work as the spatial filters for the incoming EM wave. There are four types of basic filtering behavior for the frequency selective metasurface, including band

pass, band stop, low pass and high pass, shown in **Figure 5**. The frequency selective metasurface is a typical application of the EM metasurface. In communication fields, it has been widely used in microwave EMI shielding, antenna radomes and different kinds of communication systems. The specific reflection and transmission of the EM metasurface can be designed and assembled with the frequency responding behaviors requirement in a specific frequency band.

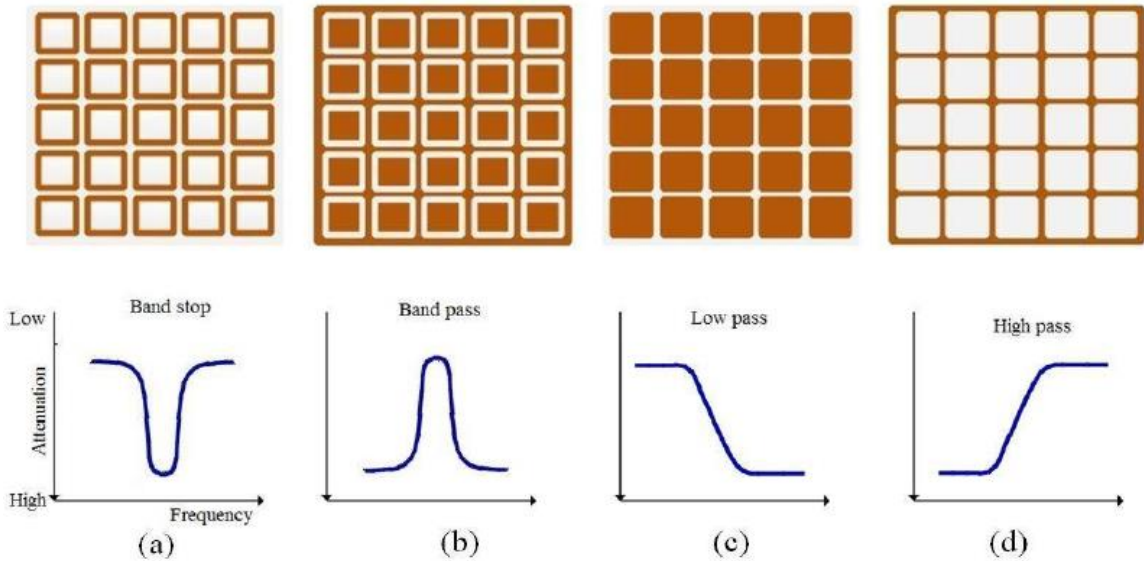


Figure 5 Four classical types of EM filter metasurface. (a) Band stop (b)Band pass (c)Low pass (d) High pass. The brown color stands for conductive part (Reprint from Ref.[34] with permission).

Da li et al. presented a metasurface structure consists of three metallic patterned layers with unit cell of rings and two thin dielectric substrates. The thickness of each layer is 0.07λ (wavelength in GHz band)[33]. Based on the EM wave propagation theory, the metallic ring structure leads a more stable EM responding system to the incident wave from different incident angles. The function of four Z-shaped centrosymmetric patterns as the unit cell of the middle metallic layer is to make metasurface has stable performance under the different polarization modes. The square loop S_1 was designed to form a transmission zero in the band edge, as a stopband. It can sharpen the band edges and improve the EMI shielding efficiency (shown in **Figure 6**).

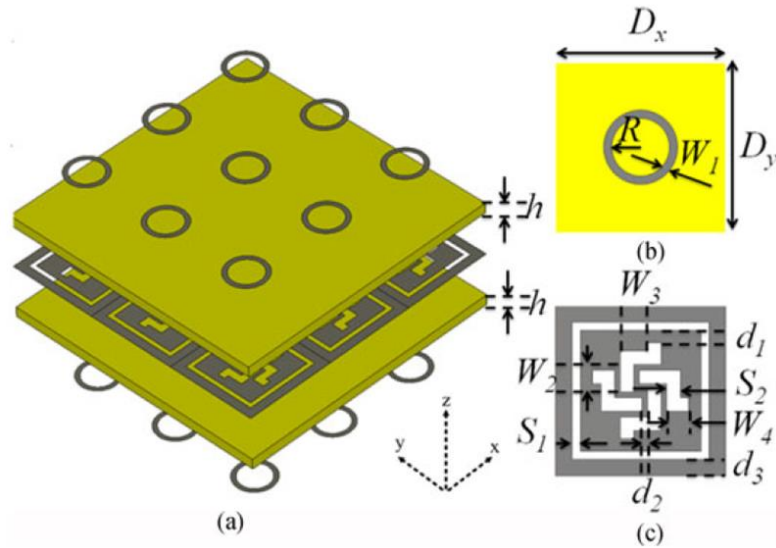


Figure 6 Configuration of the metasurface, (a) 3-D view, (b) the metallic ring unit cell, (c) the middle metallic layer unit cell (Reprint from Ref. [33] with permission).

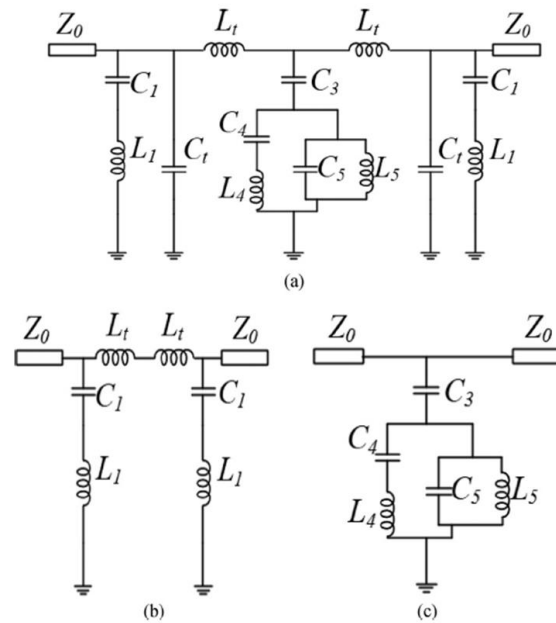


Figure 7 (a) Equivalent circuit model of the proposed metasurface (bandpass filter). (b) Equivalent circuit model of the top and bottom metallic layers. (c) Equivalent circuit model of the middle metallic layer (Reprint from [33] with permission).

Based on equivalent circuit analysis, two ring layers on the top and the bottom metallic can be modeled as the same serial LC resonator (L_1C_1 in **Figure 7**). The dielectric substrate can be modeled as the transmission line with length equals the thickness of the substrate. The equivalent inductance L_t and capacitance C_t can be calculated as $L_t = \mu_0\mu_r h$, $C_t = \epsilon_0\epsilon_r h/2$. The middle metallic layer can be equivalented as a parallel L_5C_5 resonator in parallel to series L_4C_4 resonators.

Theoretically, we can calculate the performance of metasurface from the equivalent circuit model. However, in most cases, the model is too complex to make a precise analysis. Simulation is still the primary method for us to optimize the design parameters. We can make a further understanding of the simulated results with the help of the equivalent circuit model.

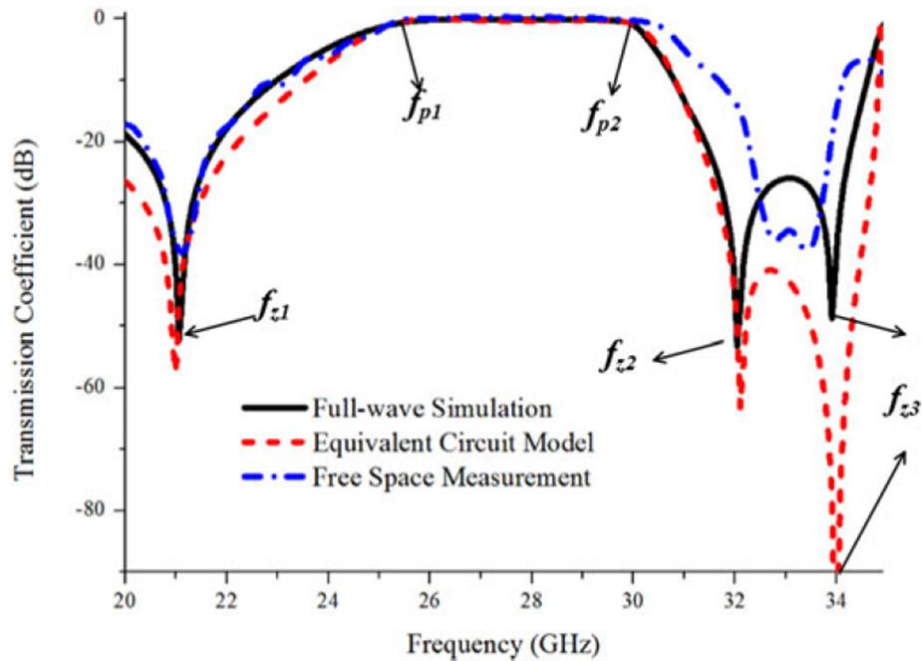


Figure 8 Transmission coefficients comparison of full-wave simulation, equivalent circuit model, and free space measurement. (f_{z1} – f_{z3} : the frequency values when S_{21} comes to minimum. f_{p1} – f_{p2} : the frequency values when S_{21} comes to the maximum. Reprint from [33] with permission).

According to **Figure 8**, the full-wave simulation results show good agreement with the equivalent circuit model. The metasurface was fabricated by using the traditional PCB process and substrate bonding techniques. The EM response of the metasurface was obtained by using the free space measurement method. From the measured results, the metasurface can effectively build a stopband from 32 to 34 GHz with more than 20 dB shielding coefficient. In this work, the design of the metasurface structure is sophisticated and the production cost in the whole process is high.

W. Whittow et al. developed a frequency selectivity metasurface on the textile via printing technology[35]. The unit cell structure of the metasurface is a single square ring, shows in **Figure 9 (a)**. The length of the square is 28mm and the designed bandstop frequency is 3 GHz. The fabrication process includes screen printing and inkjet printing. An interface layer with a thickness of 150 μm was realized via screen printing on polyester cotton after the UV curing. Then, silver nanoparticle ink is printed directly on top of the interface layer to form the conductive layer.

From **Figure 9 (b)**, the difference of the frequency filtering performance between the measured and simulated results is noticeable. The main reason is the conductivity of the printed sample is lower than expected. The roughness of the textile will decrease the printing resolution, bringing the shift of the resonance frequency. In order to fabricate the metasurface with high-performance, the method with high conductivity and competitive resolution needs to be developed.

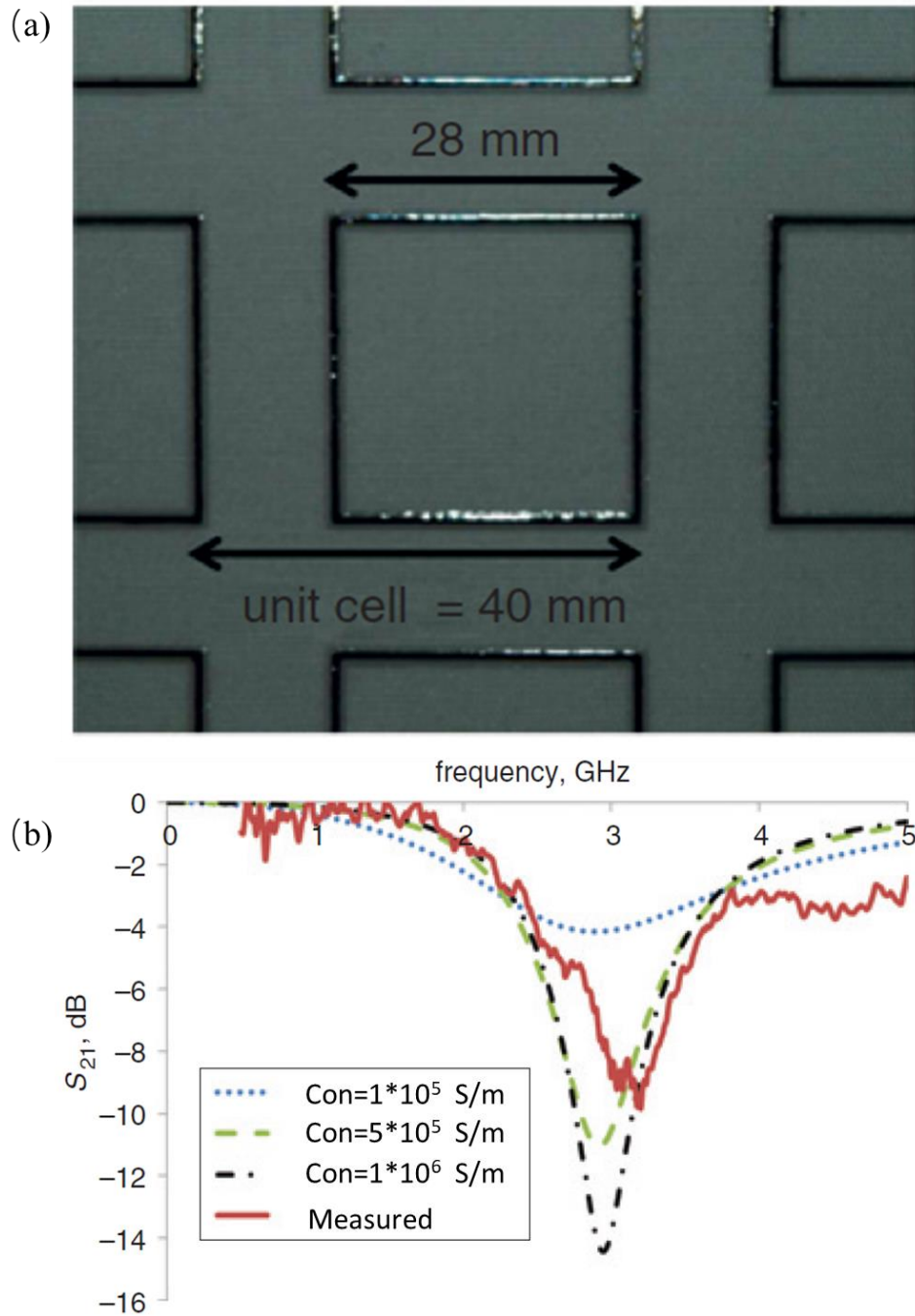


Figure 9 (a) Geometry of the designed metasurface. (b) Measured and simulated performance of the printed metasurface (Reprint from [35]).

Veronica Sanchez-Romaguera et al. fabricated the metasurface on the paper substrate with a resonance frequency at 13 GHz via inkjet printing. The printed metasurface demonstrated the performances in wireless communication, which requirements a forward transmission parameter depth greater than -20 dB(**Figure 10**)[36].

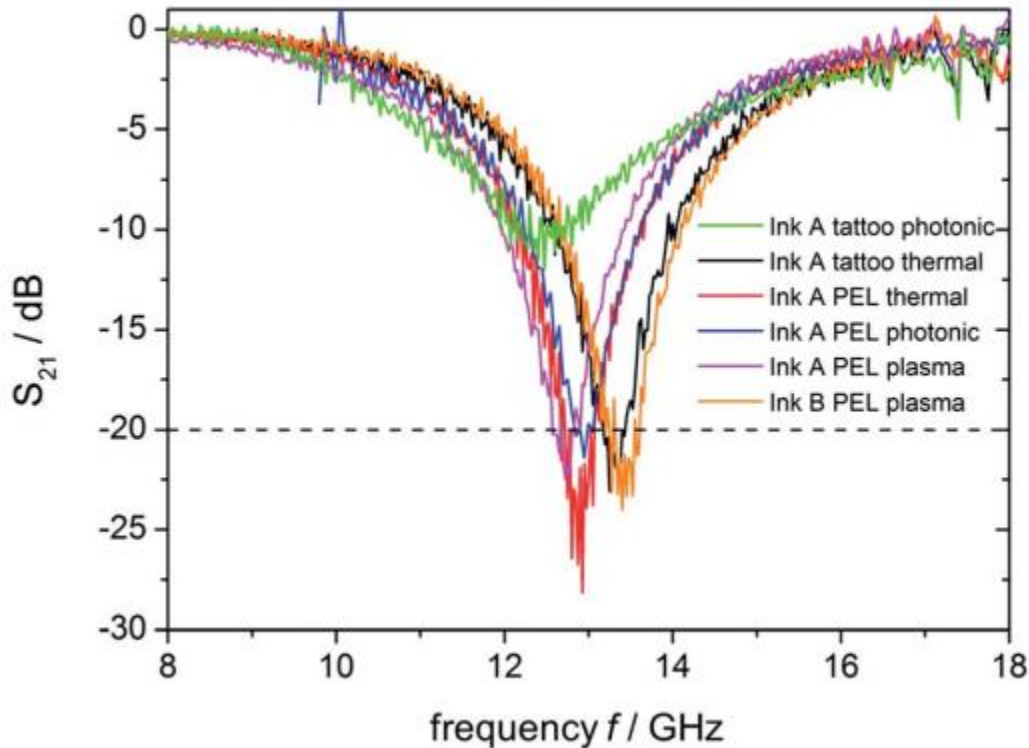


Figure 10 Measured transmission of printed metasurface on tattoo and PEL paper sintered by thermal, photonic, and plasma means(Reprint from [36] with permission).

The glycol-based dispersion limited the silver loading. The lowest resistance of the printed metasurface is 110 m Ω /sq after photonic or plasma sintering. The resistance is still high, and the post-treatment process is complicated. To improve the performance of the printed metasurface, we need to improve the silver loading in ink. The post-treatment process will increase the fabrication time and raise the cost. It is expected to develop a post-treatment free process to fabricate metasurface by printed electronics method.

1.3.2 Application of metasurface in EM wave absorption

Absorption is another basic manipulation application of the EM wave. There is a considerable market for EM wave absorption in modern society due to the increase of EM radiation pollution. EM wave absorber can play a vital role in promoting Industry 4.0 production, avoiding EM wave disturbance, and maintaining human health. More applications can be expected under the incoming technology revolution period.

A perfect EM wave absorber should be designed with high EM wave absorption, thin thickness, lightweight, broad width, tunable absorption frequency, and multi-functionality. EM wave absorption is an energy depletion and transformation process. To realize energy absorption without reflection and transmission, the energy of the EM wave should be depleted and then transformed into thermal energy or other kinds of energy (**Figure 11**).

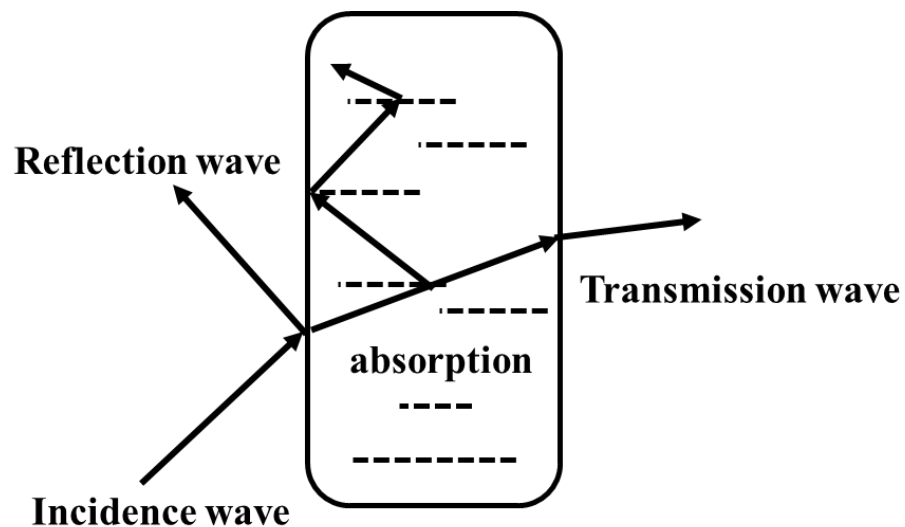


Figure 11 The general processes of an incident EM wave through an EM absorber.

Two prerequisites need to be satisfied to produce an ideal EM wave absorber. First, to reduce reflection, the impedance between free space and the material surface must be matched, requiring the complex permittivity of the material close to complex permeability; Second, materials must show strong magnetic or/and dielectric loss of the EM wave, which

can absorb more incident waves inside of absorbers. Normally, we use reflection loss (R_L) to indicate EM wave absorption ability[37]:

$$R_L = -20 \log \frac{|Z_{in-1}|}{|Z_{in+1}|} \quad (2)$$

Wherein:

$$Z_{in} = \sqrt{\frac{\mu' - j\mu''}{\varepsilon' - j\varepsilon'' / (\omega\varepsilon_0)}} \cdot \text{th} \left(jd \sqrt{\frac{(\mu' - j\mu'')(\varepsilon' - j\varepsilon'' - \frac{j\sigma}{\omega\varepsilon_0})}{c}} \right) \quad (3)$$

$$\text{And } \omega = 2\pi f \quad (4)$$

Where Z_{in} : impedance of incident wave;

μ' : real part of permeability; μ'' : image part of permeability;

ε' : real part of permittivity;

ε'' : image part permittivity; ε_0 : permittivity of vacuum; σ : conductivity; f : frequency of EM wave; d : thickness of material; c : the light of speed. (symbols are applicable for equation (2) - (6))

There are two main energy depletion mechanisms: magnetic loss and dielectric loss. Eddy current loss is a key type of magnetic loss. Eddy current loss occurs when an induced current is produced inside the conducting material under an alternating magnetic field. The induced current would dissipate the energy of the EM wave. We apply e to represent the eddy current loss coefficient[37]:

$$e = \frac{4\pi^2 \mu_0 d^2 \sigma}{3} \quad (5)$$

To increase the eddy current loss coefficient, we should increase the thickness and conductivity of the absorber material based on equation (5). But the high conductivity will cause fluctuating permeability at high frequency, thus limit the working band into low frequency and narrow bandwidth.

Conductance loss is the main part of dielectric loss. Like the phenomenon of eddy current loss, conductive absorber will generate conductance current under an alternating electric field. It can be expressed by conductance loss tangent, $tg\delta_c$ [37]:

$$tg\delta_c = 1.8 \times 10^{10} \frac{\sigma}{f\epsilon_r} \quad (6)$$

The determining factor of the conductance loss tangent is conductivity from equation (6).

In the band of infrared to ultraviolet, the resonance loss was observed. Resonance effect induced by the vibration of atoms, ions, or electrons can be well utilized to develop perfect metasurface EM absorber. We can manipulate the resonance effect in μ and ϵ independently to absorb both the incident electric and magnetic field as much as possible. Also, by matching μ and ϵ , metasurface can be impedance-matched to free space, which will minimize reflectivity. W. Padilla's group designed a metasurface EM wave absorber includes of two distinct metallic elements[38]. Shown in **Figure 12**, the unit cell of the metasurface was made up of two split ring metal resonators connected by the inductive ring parallel to the split-wire. Such a metasurface structure shows great absorption performance mainly for the dielectric losses, which occurs between the two metasurface elements due to the high electric field.

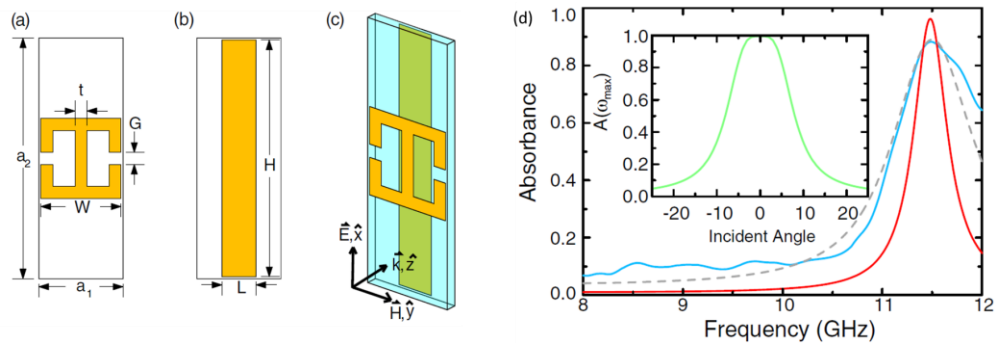


Figure 12 Structure, simulation and performance of a classical metasurface EM wave absorber. (a) Electric resonator and (b) cut wire. The unit cell is shown in (c) with axes indicating the propagation direction. (d) shows the simulated (red) and measured (blue) lines. The dashed line is a Gaussian weighted average which approximates assembly error. The inset shows the simulated angular dependence of the $A(\omega)$ at ω_{max} (Reprint from Ref.[38] with permission).

In the visible and near-infrared spectrum, metasurface absorber was designed and fabricated with the advantages of broadband, polarization-independent, and wide-angle. Absorption efficiency of more than 90% was realized in the visible and near-infrared spectrum[39]. The metasurface' unit cell consists of eight pairs of gold nano-resonators. A thin silicon dioxide layer separates the gold resonators with a gold plane (**Figure 13**).

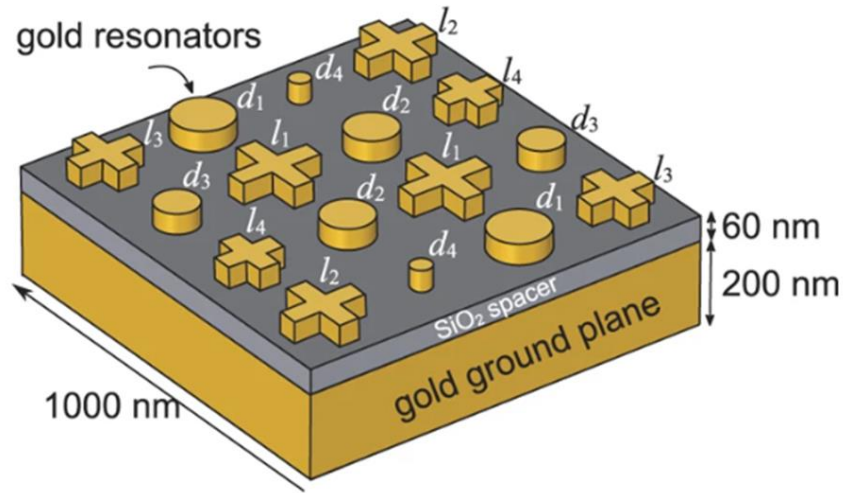


Figure 13 Unit cell design of the metasurface absorber. A square array of cross and cylinder with 16 resonant elements: $l_1 = 200$ nm, $l_2 = 180$ nm, $l_3 = 160$ nm and $l_4 = 140$ nm; $w = 50$ nm; $d_1 = 140$ nm, $d_2 = 120$ nm, $d_3 = 100$ nm and $d_4 = 50$ nm (Reprint from [39] with permission).

The metasurface absorber was fabricated via electron beam lithography method, metal deposition and a lift-off process. The 200 nm thickness of the gold ground plane reduces the EM wave transmittance through the structure to almost zero. Parameters were optimized to realize an idea absorption efficiency and a desirable absorption spectrum band, like the dimensions of the resonators, the spatial distribution of resonators and the thickness of the dielectric spacer (**Figure 14**).

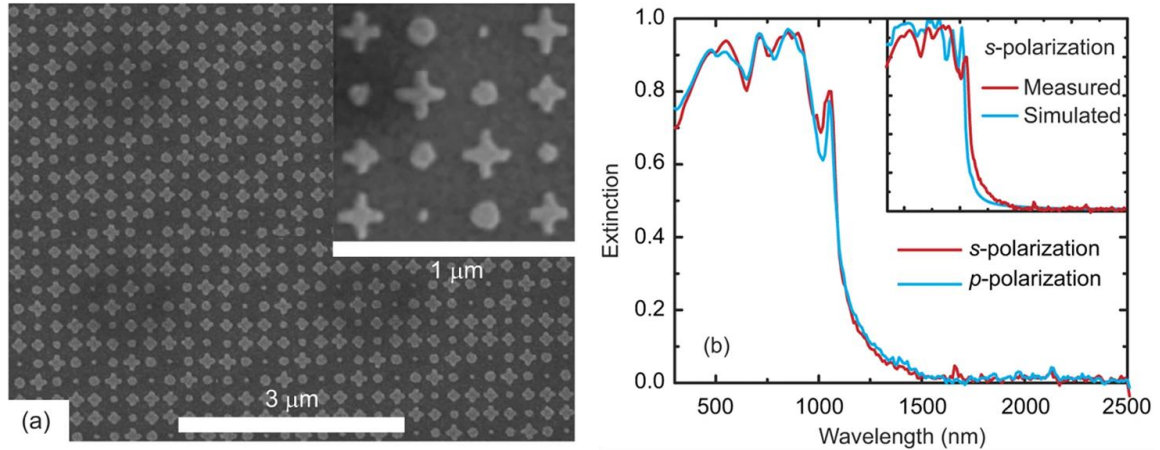


Figure 14 (a) SEM image of the fabricated metasurface absorber. The inset represents an expanded view of the unit cell. (b) Experimentally measured extinction for s- and p- polarizations at a 20° angle of incidence. Inset to (b) is a comparison of results between experiments and simulations (Reprint from [39]with permission).

Despite metallic materials, metasurface EM absorber based on conducting polymer was also proposed and developed. From the previous research, there are many characteristics for conducting polymers, like low density, tunable conductivity, even controllable magnetic properties, which enable a high wave absorption potential in the high absorption efficiency, controllable absorbing spectrum, and a broad absorption range. Conductive polymer based EM metasurface also has advantages in the fabrication. 3D printing can be applied to fabricate high feature metasurface with digitalization, low cost and large scale.

Jiang Wei et al. designed a 3D metasurface absorber consisting of the honeycomb structure and resistive films (**Figure 15**)[40]. Such a design was realized through 3D printing and silk-screen printing technology with an absorption efficiency of more than 90% in a broadband of 3.53–24.00 GHz (**Figure 16**). In this structure, the folded resistive patches extend the absorption band and contribute to the wide-angle absorbing characteristic. High mechanical performance was also achieved with low density and high compressive stress of 10.7 MPa, which extends its application in aerospace engineering.

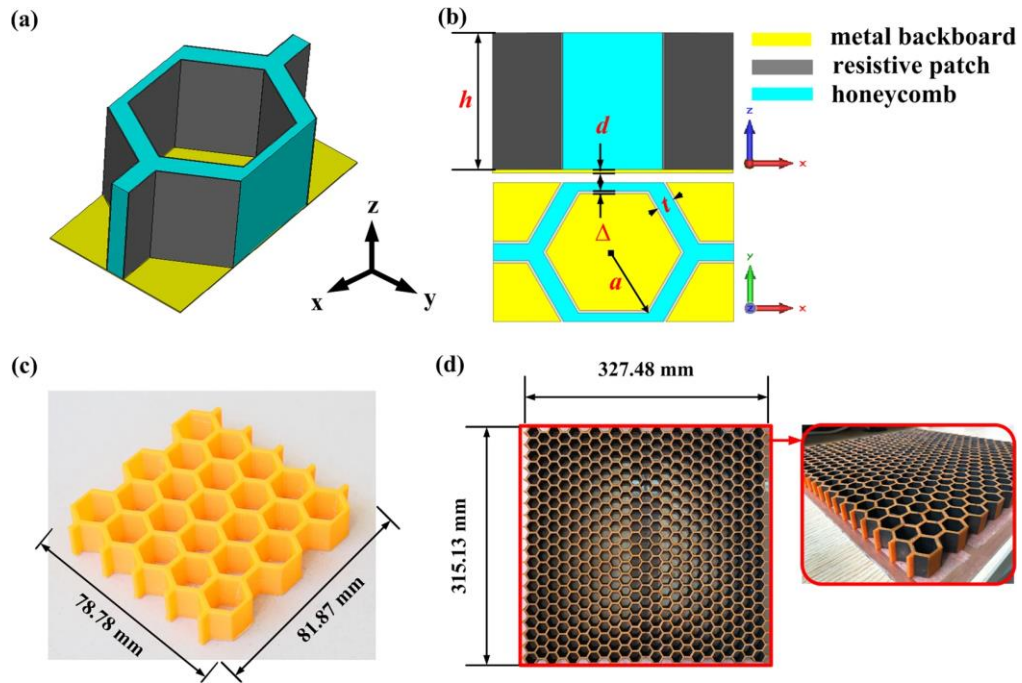


Figure 15 Structure design of the 3D metasurface absorber. (a) Unit cell diagram. (b) View of the unit cell in the plane of x-z and x-y. (c) Honeycomb sample for compressive test and (d) sample of the 3D metasurface (Reprint from Ref.[40] with permission).

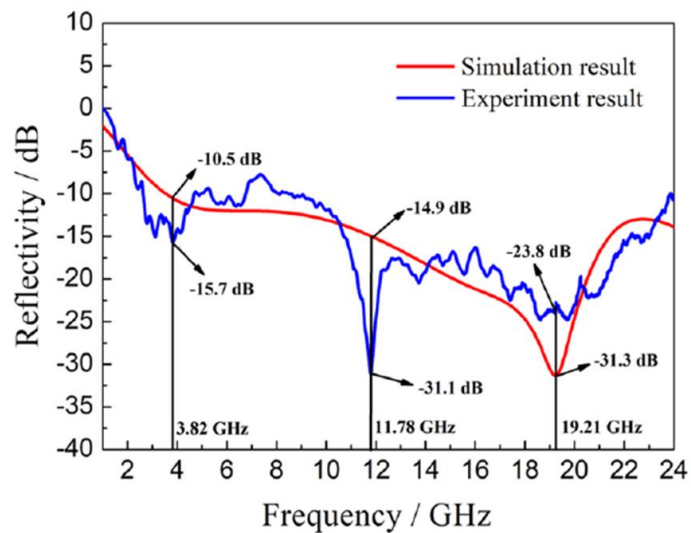


Figure 16 Simulation and experiment results of reflectivity for vertical incident waves (Reprint from [40] with permission).

Flexible metasurface EM wave absorbers share many advantages over their non-flexible counterparts in the application. They are suitable for roll-to-roll production, much lighter in weight, smaller in size, much more durable, and excellent flexible and conformal ability. Flexible metasurface EM wave absorbers were typically fabricated using flexible dielectric films like polyimide, polydimethylsiloxane (PDMS) and Teflon which can be easily conformed to the desired surfaces such as the cylindrical, pyramid, and spherical.

Wang Xin et al. designed and experimentally proved a flexible dual-band metasurface EM wave absorber with the unit cell of single T-shaped copper patches on the flexible polyimide (PI) layer (**Figure 17**)[41]. The parameter of the geometric, like the thickness, was optimized with CST simulation. An ultrathin thickness of 0.2403 mm, which is only 1/74 and 1/40 of the wavelength for the working frequency of 16.7 and 30.92 GHz, was realized via the laser ablation process.

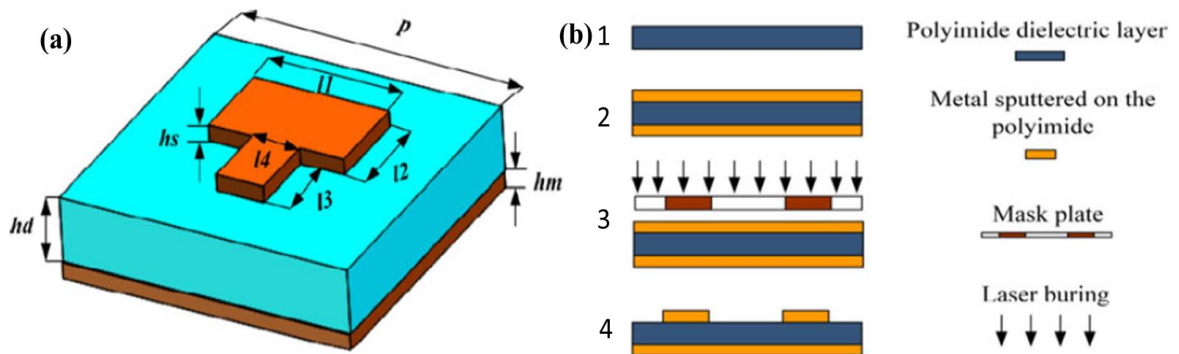


Figure 17 (a) Unit cell schematic of the proposed metasurface EM wave absorber.

(b) Flow diagram of the laser ablation process (Reprint from Ref. [41] with permission).

From the simulation, the proposed metasurface EM wave absorber can also be used to detect and filter the incidence EM wave. The designed metasurface EM wave absorber has a broad range of the incidence angle for the incidence EM wave. From the test results, two distinct absorption peaks at 16.85 GHz and 30.79 GHz with the absorption ratio of 98.6% and 96.2% were found (**Figure 18**).

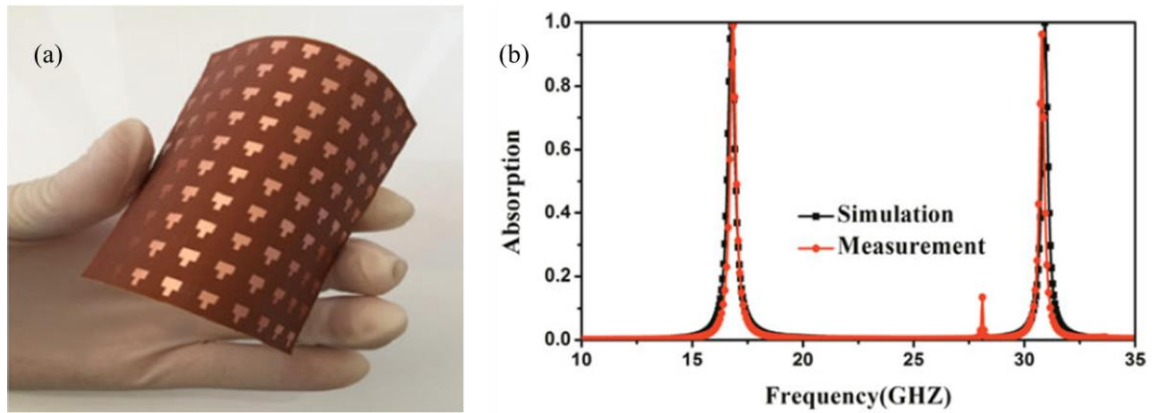


Figure 18 (a) Fabricated sample of the proposed dual-band flexible metasurface absorber. (b) Simulated and measured absorption properties of the dual-band flexible metasurface absorber (Reprint from [41] with permission).

As a very popular commercial polymer, the Teflon can also be a candidate of dielectric substrate for the GHz range metasurface EM wave absorber, with the properties of thin, flexible, and elastic. Y. Yoo et al. designed a snake-shaped unit cell on the Teflon substrate to realize the thin and, and flexible metasurface absorber with high absorption efficiency [42]. From the simulation result, the geometry parameter of the snake structure influences the surface current flows and can control the resonance absorption peak (**Figure 19**).

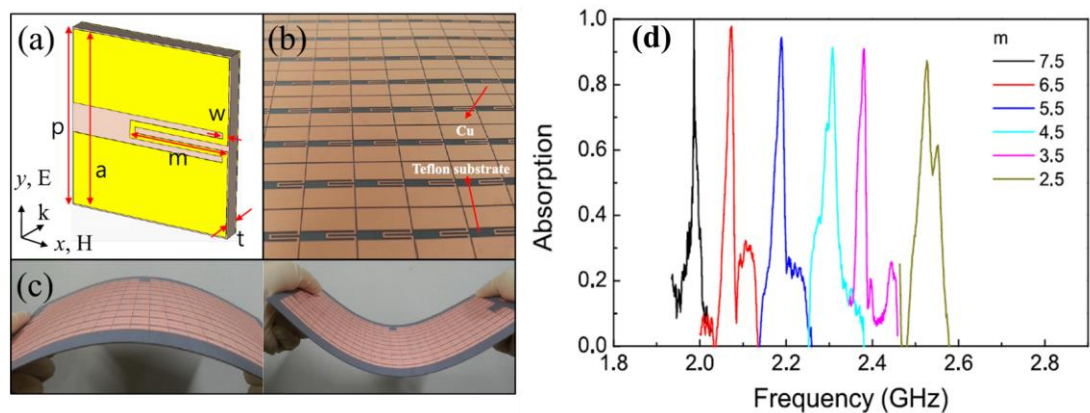


Figure 19 (a) Unit cell for the metasurface absorber in snake structure and (b) photo of the fabricated sample. (c) The flexibility of the Metasurface absorber. (d) measure absorption by the length, m (Reprint from Ref.[42] with permission).

1.4 Fabrication of Electromagnetic Metasurface

Different kinds of fabrication technologies can be applied according to the feature requirement of the metasurface. In the microwave frequency band, the line width of the metasurface should be larger than 10 microns, which means that the classical mechanical or optical approaches can be applied. The most important one is the printed circuit board (PCB) technology (shown in **Figure 20**). This technology is based on mechanical drilling, etch, and laser ablation method. Such technology has enormous advantages in large-scale production, with the characterization of low cost and high-speed production. However, the flexibility of technology is limited. The cost will be expensive in small scale production with high prototype fees. More and more environmental concerns were noticed due to the pollution of the chemical processing.

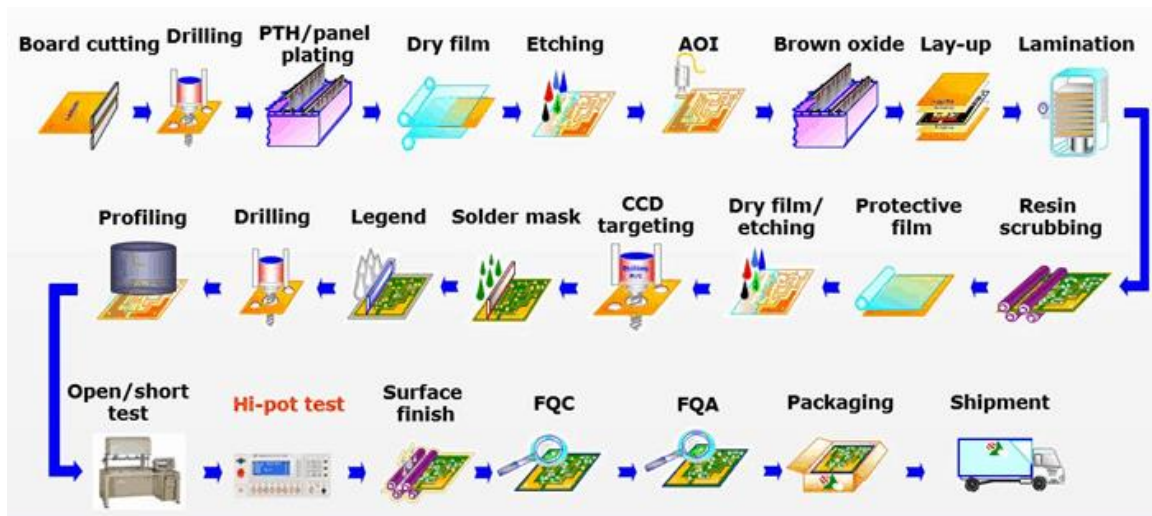


Figure 20 Printed Circuit Board Working flow (Reprint from GESP Technology)

With the increase of the frequency, the feature size of the metasurface which applied in terahertz to mid-infrared band decreases to 1-10 micro. To realize the fabrication in this scale, we can apply the photolithography[43], laser ablation and laser direct writing[44].

In the near-infrared and visible band, the feature of metasurface reaches the nanometer scale. Due to the limitation of the traditional method, advanced nano-fabrication technologies were applied, like electron beam lithography (EBL) and focused ion beam milling (FIB)[45]. A mature commercialized process has been built to design and fabricate

the metasurface, but the cost of the whole process is still high. More and more edging technologies are proposed to fabricate specific metasurface. UV laser is a powerful tool to operate periodic structures on the scale of 100 nm. Interference lithography also has huge potential to produce periodic patterns, like dot array and grating, but the size of the devices is limited. The plasmonic lithography technique, like the surface plasmon interference technique, overcomes problems above. It is one of the most promising choices to fabricate large-area simple periodic structures. But it is also hard to fabricate the complex pattern and limited in period structure. The reflective plasmonic lens was designed to curve the pattern with high fidelity, contrast and enhanced depth[46].

In this thesis, we focus on solving the current fabrication issues of the metasurface. First, the resolution of the fabricated pattern has to meet the working frequency band requirement. We can also improve the pattern design and structure modeling to reduce the complexity of physicalizing. Second, the production cost can be decreased by simplifying the fabrication process. Third, in engineering applications, the production process needs to be scalable and controllable. Roll to roll process can be built to form a scalable way of metasurface fabrication. Fourth, the green process should be developed to create a healthy fabrication environment and avoid pollution from waste and toxic.

1.5 Research Objective

The metasurface can play critical roles in future society. Printed electronics technology has been applied to the fabrication of metasurface. Some problems still need to be solved, like conductivity control of the printed sample, cost of conductive ink, simplification of printing process and scalability. The objective of this thesis is to develop high efficiency, fast prototype, low cost, environment-friendly methods to fabricate the metasurface for the application of EM wave manipulation, including EM wave selective reflection and absorption.

Chapter 1 introduced the printed electronics technology and the background of the metasurface, from the mechanism, fabrication to the applications. The printed electronics technology provides opportunity to overcome the limitations of traditional fabrication methods of metasurface.

Chapter 2 presents the numerical study of the metasurface, consist of configuration design, parameter optimization in the application of EM wave selective reflection and absorption. The numerical study results were applied to guide the fabrication process.

Chapter 3 focuses on the digital reaction on demand (DRoD) method to fabricate the metasurface. The core parameters of printed metasurface were measured and discussed.

Chapter 4 evaluates the performance of the DRoD method prepared metasurface. The application of the EM metasurface was extended to food safety monitoring.

Chapter 5 provides a summary of the thesis and presents the perspective for the future work.

Chapter 2

2. Numerical Study of Metasurface

The printed electronics technology is a powerful tool to fabricate the metasurface. Before the fabrication process, a numerical study should be conducted to optimize the parameters in the structure design. The infinite element method based on the COMSOL is applied to simulate the device performance in the full EM wave environment. In this chapter, the modeling and simulation of the metasurface were discussed.

2.1 Design of EM wave selective absorption metasurface

The EM wave selective absorption metasurface can be realized by eliminating the reflection wave and the transmission wave through the conductive and dielectric losses. For a metasurface absorber, the absorption efficiency can be expressed as follows[41]:

$$A = 1 - |S_{11}|^2 - |S_{21}|^2 \quad (7)$$

where A represents absorption efficiency, S_{11} represents reflection efficiency (the ratio of the amplitude of the reflected wave to that of the incident wave) and S_{21} represents transmission efficiency (the ratio of the amplitude of the transmitted wave to that of the incident wave)[47]. The metallic sheet can stop the transmission of the EM wave. In this work, like most of EM wave absorber study, S_{21} is trending to 0 due to the ground plane is fully covered with the metallic sheet. Ultra-low reflection efficiency can be achieved by matching of the permittivity (ϵ) and permeability (μ) of the metasurface, adjusting the conductivity and geometry parameters.

A double square structure was designed to meet the requirements of high absorption efficiency, wide bandwidth, polarization stability and high printability. The structure is simple and with few variable parameters. The unit cell of the metasurface absorber proposed in this thesis is illustrated in **Figure 21**. It consists of a double square resonance conductive composite unit, a metal ground plane and a dielectric layer in the middle. In this thesis, we use CNTs (Carbon nanotubes)/PLA (Polylactic Acid) conductive composite as the absorption functional material. CNTs are induced to control the conductivity and

adjust the permittivity, which can increase the current loss and expand the absorption bandwidth[48]. PLA is a mature material for the printing application with low density and proper permittivity. The copper with conductivity $\sigma = 5.5 \times 10^7$ S/m serves as a ground plane to eliminate the transmission wave. The transparent PET (Polyethylene terephthalate) with a relative permittivity of $\epsilon_r = 3.3$ and a loss tangent of 0.02 works as a flexible dielectric layer. In the double square structure, we have $w_1 = w_2$ to form a stable LC resonating unit. The length of the square side, L_1 and L_2 are calculated to meet the center frequency of 10 -10.1 GHz, which is a widely used frequency band in the communication. Both width w and thickness d will be optimized through the simulation.

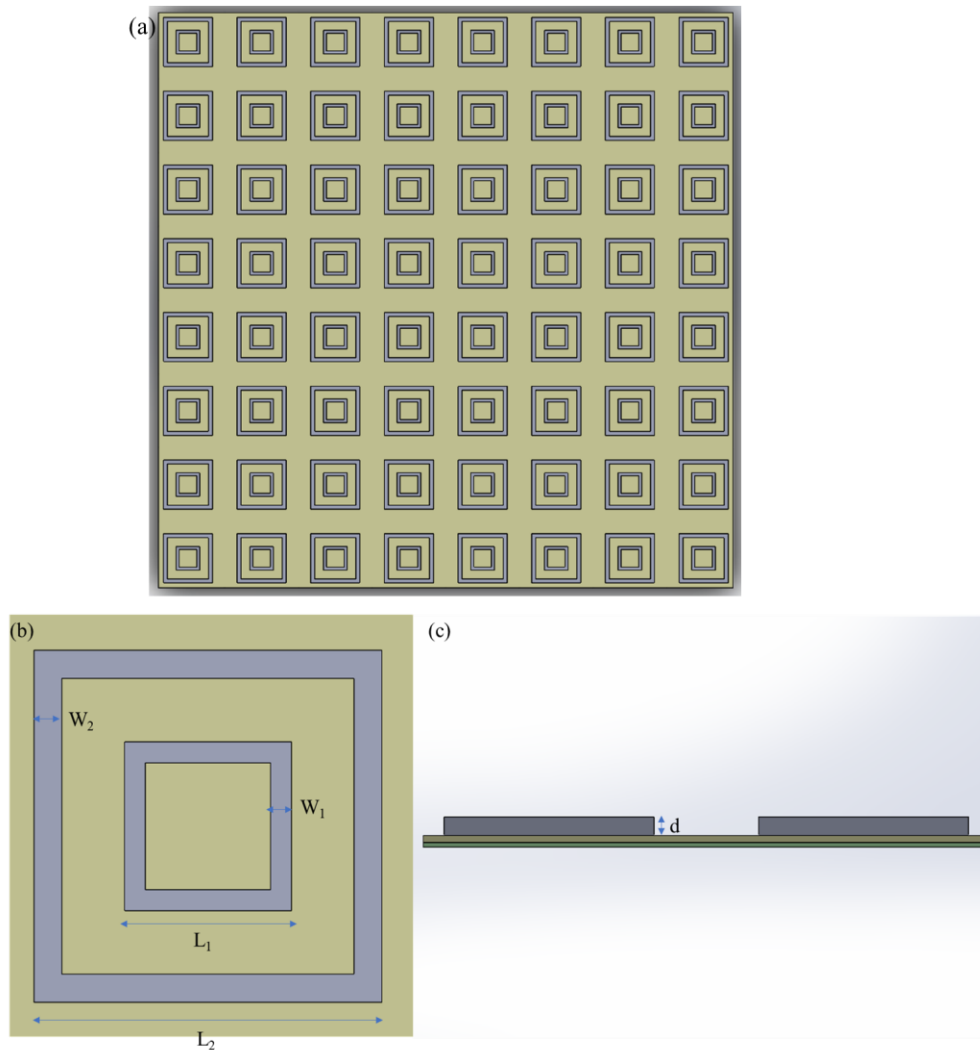


Figure 21 Metasurface EM wave absorber. Top(b) and side(c) view of the unit cell.

2.2 Parameters optimization of metasurface absorber

2.2.1 Optimization of the square width

From the classical equivalence circuit theory analysis, the width of the square ring can affect the surface electric field by changing the series-resonant circuits inductance and capacity in the equivalence circuit[49]. To achieve the desire absorption efficiency, the high capacitive coupling surface current density was realized, which requires a good balance of electric filed and surface area. In this case, we find that when the $w=0.8$ mm, the metasurface structure can have the best absorption performance, from the simulation results (**Figure 22**).

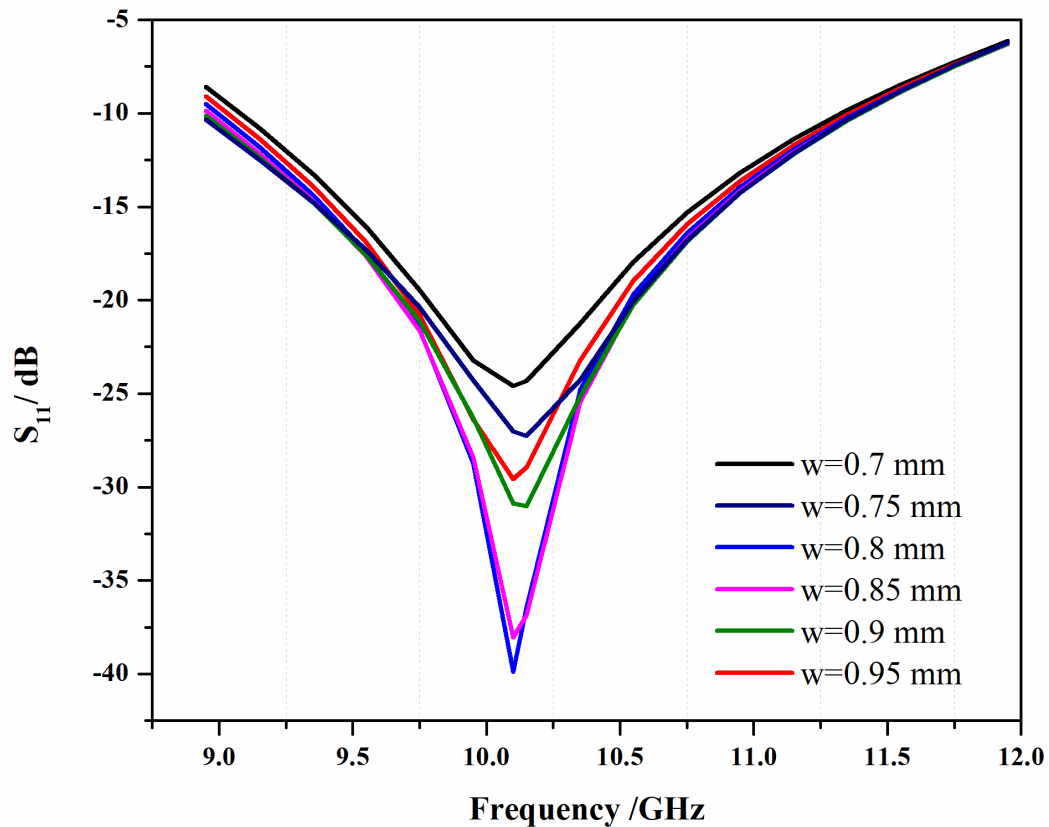


Figure 22 Simulation results of absorption efficiency with width from 0.7 to 0.95 mm.

2.2.2 Optimization of the metasurface thickness

From the simulation results shown in **Figure 23**, 0.8 mm is the ideal thickness for the metasurface the desired structure and absorption working frequency. With the increase of the thickness, the current loss generated by the eddy current flow will increase, then lead a better absorption. But the increasing of the thickness will result in resonance shift. The dielectric match of the whole structure is a critical point for the whole wave absorption process. When $d=1\text{mm}$, high absorption efficiency can still be realized, but the apparent shift of the resonance frequency is not desired.

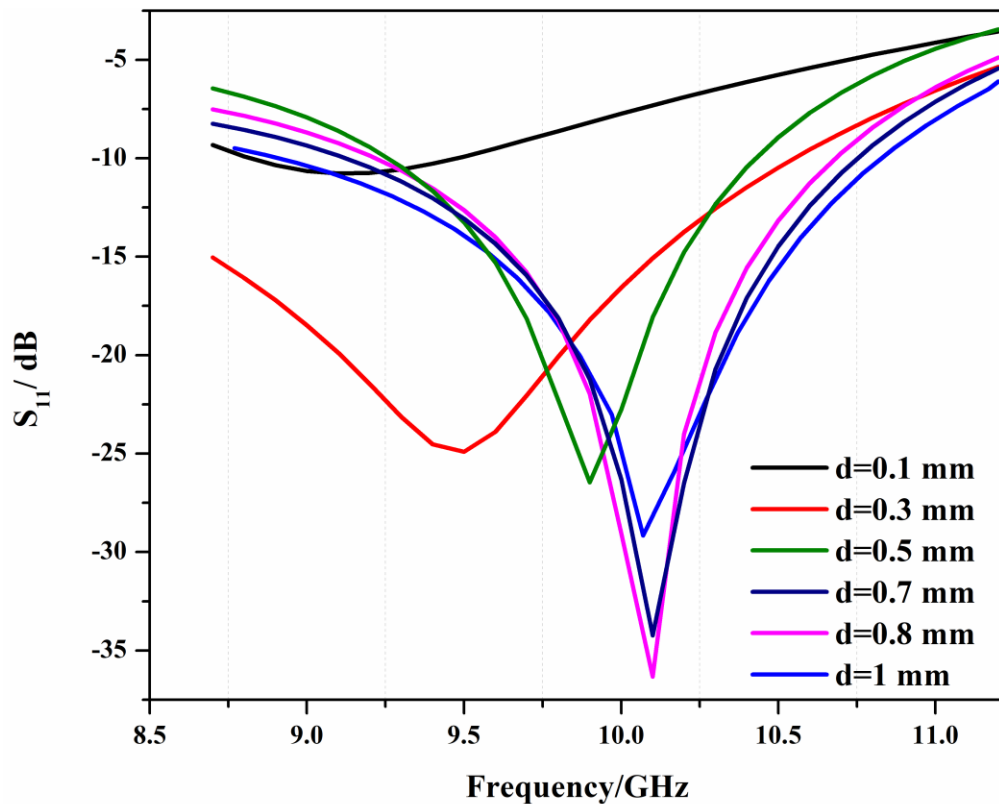


Figure 23 The influence of the thickness on the absorption efficiency.

From **Figure 24**, we can find the difference in electric field distribution between the thickness of 0.3 mm and 0.7 mm. Compared with the thickness of 0.3 mm, a higher electric field intensity was obtained when the thickness is 0.7 mm. The higher electric field can lead to larger surface current density then result in higher eddy current loss.

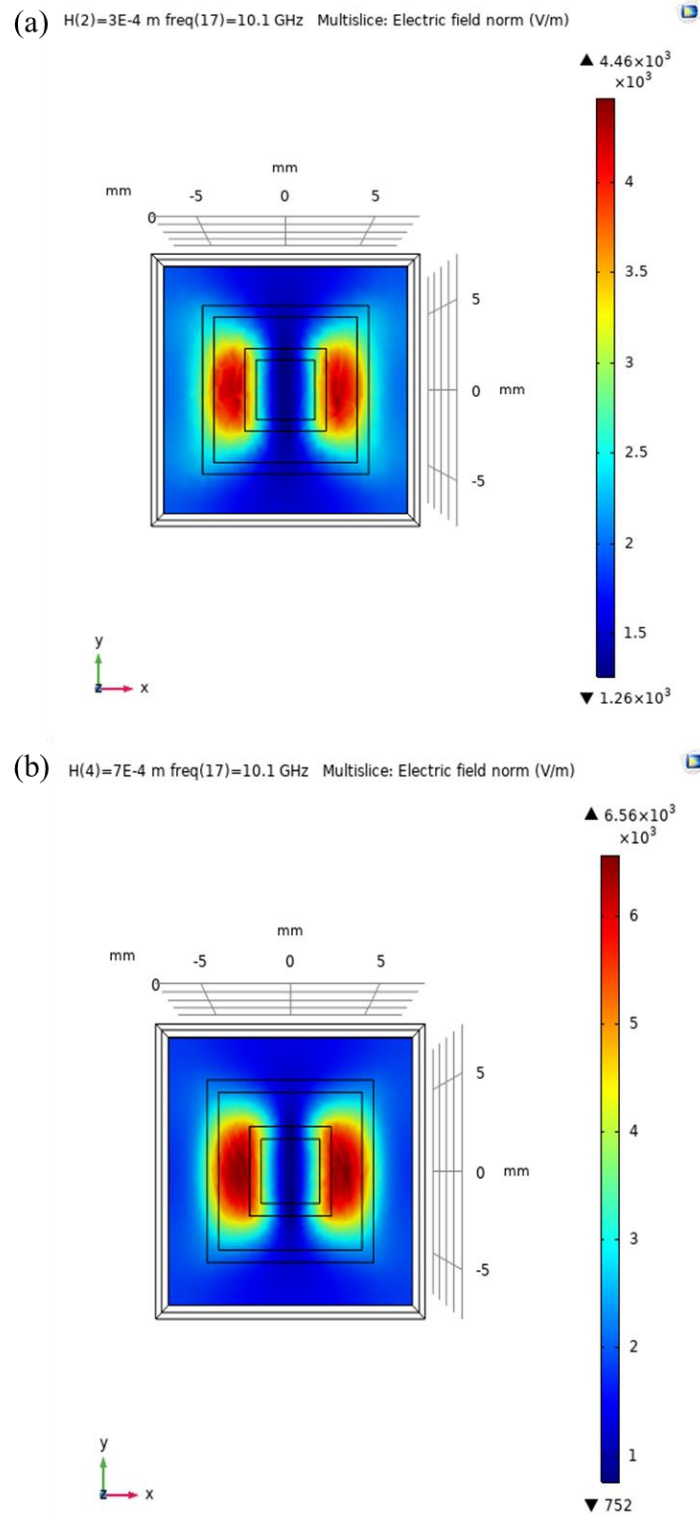


Figure 24 Simulation results of electric field distribution on metasurface with different sizes. (a) $d=0.3$ mm (b) $d=0.7$ mm.

2.2.3 Optimization of the conductivity

With the increase of the conductivity, the eddy current loss and conductance loss will increase, then the absorption will increase, shown in **Figure 25**. However, the higher conductivity will decrease the surface impedance. The reflection will increase with shallow absorption depth. Most of the EM wave will be reflected with the further increase of the conductivity.

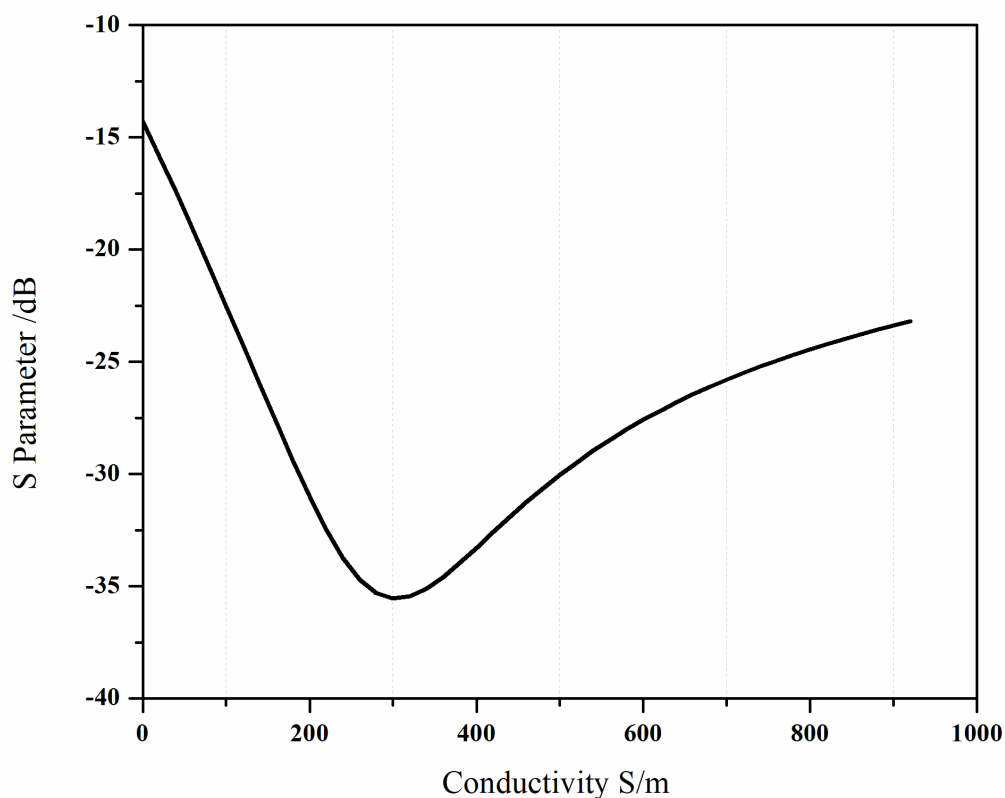


Figure 25 Simulation results of the absorption efficiency at the resonating frequency with conductivity range from 10-950 S/m.

According to **Figure 25**, conductivity from 250-340 S/m is the promising conductivity range with a perfect match of current loss and reflection effect. The further investigation shown in **Figure 26** reveals that the absorption efficiency can achieve the best performance when conductivity is 300 S/m.

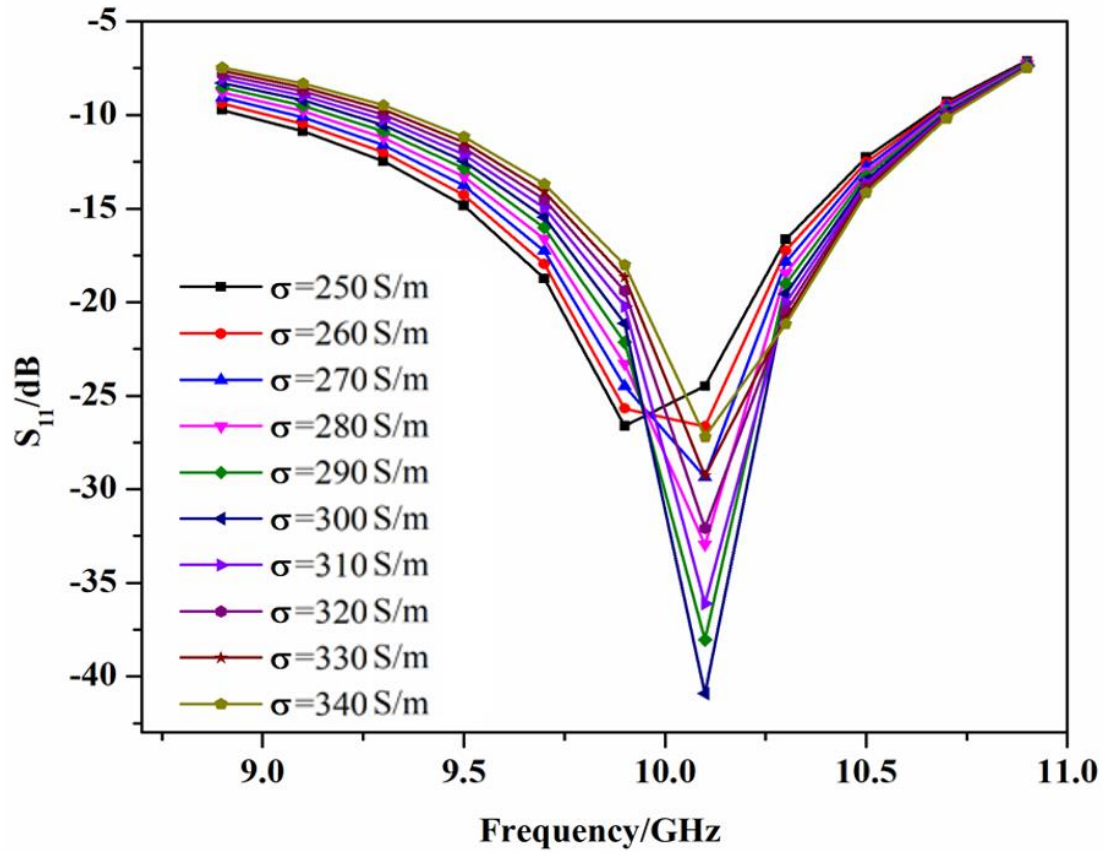


Figure 26 Optimization of the conductivity from 250 to 340 S/m.

2.3 Numerical study of EM wave selective reflection metasurface

In this thesis, a novel metasurface structure with high selectivity, sharp falling band edge for selective reflection applications at the center frequency of 29-31 GHz was proposed. The spectrum in the range of 29-31 GHz (millimeter-wave frequency band (MM-waves)) has been selected for the possible adoption of wireless communication[50]. The novel wideband metasurface used as the frequency selective engineering surface is designed to meet the extensive applications in future communication such as EM wave reflectors, electromagnetic interference (EMI) shielding surface, and radomes to system-level electromagnetic (EM) structures[51]. These types of applications, especially for the wave filtering function, are regarded as highly effective solutions for cellular networks that are promising to provide a cleaner EM wave environment and higher data transformation rates[52].

2.3.1 The design of the EM wave selective reflection metasurface

Various metasurface structures have been applied in the EM wave selective reflection applications, for example, dipole[53], slot[54], loop[55], Jerusalem cross[56], rings[57] and many other combination structures. Among all the structures, the loop structure has the advantage of angular stability, cross-polarization level and larger bandwidth. However, the size of the traditional loop is still large, which is more sensitive than the smaller elements in the incident wave angle. The meandered loop structure with the convoluted square as shown in **Figure 27 (a, b)**, can reduce the unit size significantly[58]. The equivalent inductance will increase with the reducing of unit size, and the equivalent capacitance will decrease[59]. The resonance frequency will stay in our desired level after the meandering process.

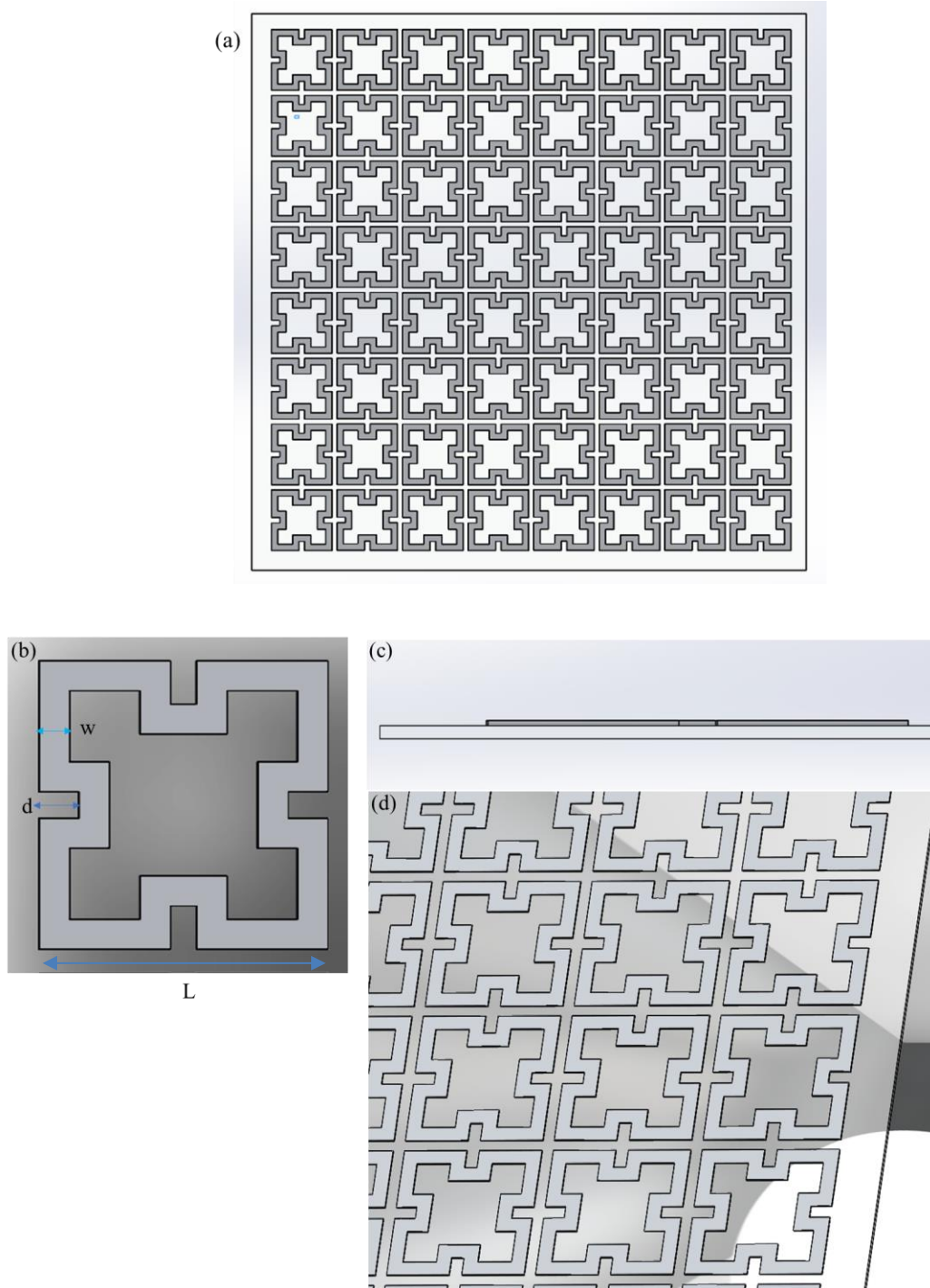


Figure 27 Illustration of the metasurface (a). (b)The unit cell structure of the period metasurface, $d = 0.39$ mm, $w = 0.22$ mm, $L = 2.4$ mm. Side view of the unit cell structure(c). Transparent metasurface with metalized surface structure (d).

The side length of the unit cell, L , is about $1/4\lambda$. The width of the square ring structure w is 0.2 mm. 4 symmetric rectangles convex structure was designed to form broadband filtering, with depth d equal to 0.39 mm. The miniaturized metasurface was printed on a polyethylene terephthalate (PET) sheet with a thickness of 0.16 mm via printed electronics method (**Figure 27(c)**). A high conductivity as 1.0×10^7 S/m was realized. The PET substrate offers high transparency and excellent flexibility for the metasurface, which can extend the application of the metasurface to the smart window and green building (shown in **Figure 27(d)**).

2.3.2 The simulation results as PCE

In the simulation of the metasurface, we assumed that the proposed metasurface is an infinite periodic structure, with the repetition of perfect conducting element (PCE) unit cell along the x- and y-axes.

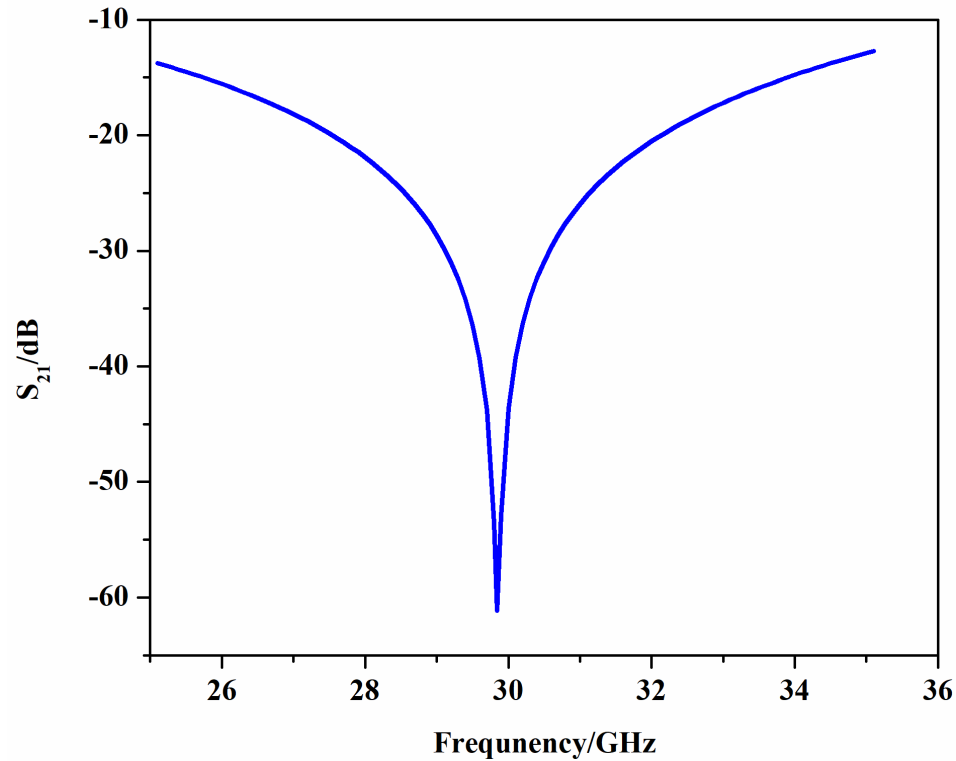


Figure 28 Simulated transmission efficiency (S_{21}) of the PCE based metasurface.

When the metasurface is the perfect conducting surface, which means an ultra-high conductivity and full reflection for the incident EM wave, the transmission efficiency is close to -60 dB. It is an excellent selective reflection performance in ideal conditions. In reality, the conductivity of the metasurface is limited. The surface roughness and defect of the metasurface will suppress the selective reflection performance and bring about resonance frequency shift.

2.3.3 The influence of conductivity

The conductivity can perform a significant impact on the transmission of the metasurface, illustrated in Figure 29. When the conductivity of the metasurface is high enough (more than 106 S/m), the shift of resonance frequency is negligible. The peak value of the transmission curve decreases with the decrease of conductivity, which means that the filtering performance will be weaker with lower metasurface conductivity. With the further decrease of the conductivity, the center filtering frequency changes obviously. The shape of the S_{21} curve turns from sharp to gentle. It can be predicted that when the conductivity is lower than 104, the metasurface will lose the EM wave filtering function. Based on the results and discussion above, it can be concluded that a high conductivity is needed to maintain the high performance of metasurface.

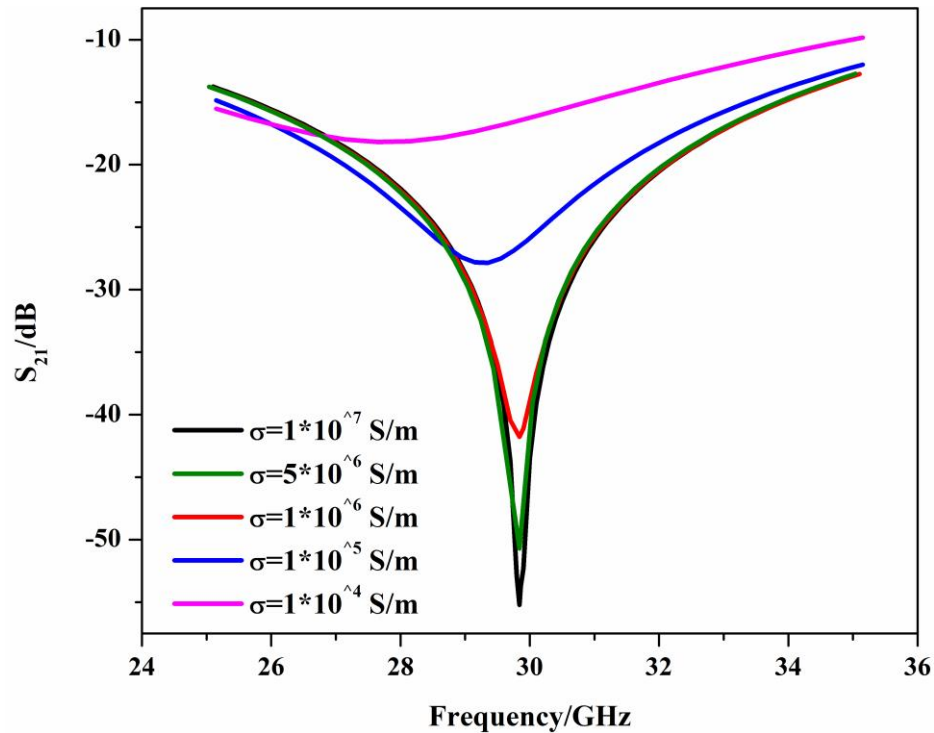


Figure 29 S_{21} curves of the metasurface under different conductivity

2.3.4 The influence of roughness

In the fabrication process of the metasurface, the defect or roughness is hard to avoid. For laser printing, many parameters like distribution of laser power, scan speed, mechanical stability, substrate properties, even scan strategy have significant influences on the formation of defects. For the inkjet printing, the nonuniform distribution of droplet can directly cause the roughness in geometry. The defect and roughness are hard to be depicted in 3D modeling. We simplified the roughness as the particle with the radius of $20\ \mu\text{m}$ [60]. The roughness can be analysed by the particles at the edge of printed line. And we separate the roughness into three levels: no roughness (ideal situation), slight roughness (little amount of extra particles or defects are formed at certain side of unit cell), and high roughness (larger number of extra particles or defects are formed at every side of unit cell), shown in **Figure 30**. In the simulation, the conductivity is set as $1.0 \times 10^7\ \text{S/m}$.

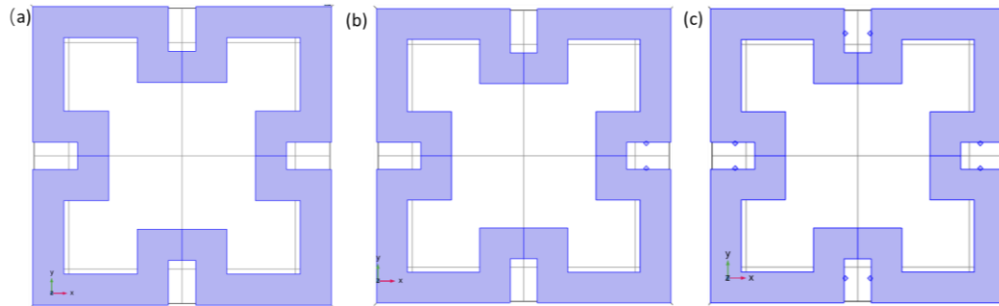


Figure 30 Simplification of the roughness of metasurface. (a) no roughness. (b) slight roughness. (c) high roughness.

Based on **Figure 31**, it can be found that the high roughness distorts the transmission curve. The roughness will break the resonate structure and shift the center filtering frequency. With slight roughness, the frequency shift is still in acceptable level. The transmission strength decreases with the roughness and the transmission curve remains flat. To ensure a high wave filter performance, the requirement for resolution of the unit cell pattern is high. The tolerance of the defect density is slight, which forces us to improve the printing quality in the printing process.

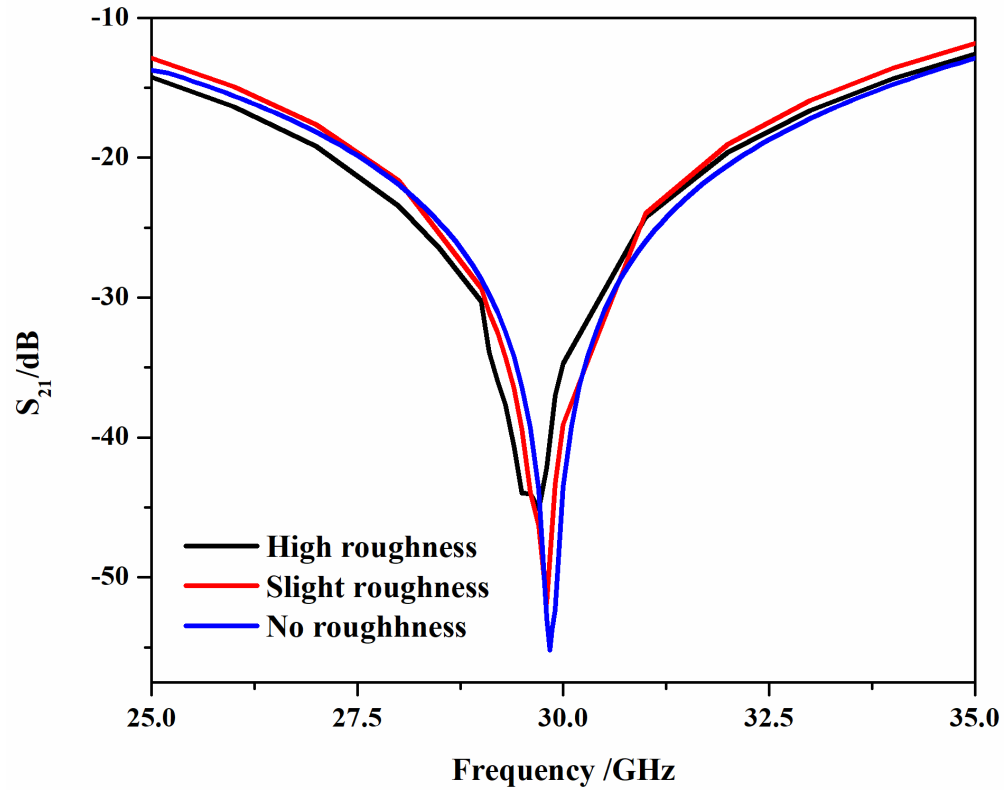


Figure 31 The influence of the roughness on the transmission performance of the metasurface.

2.3.5 The Influence of the thickness

In the simulation process, the conductivity was set as 10^7 S/m. In order to simplify the process, we assume that there is no roughness. From the results, we can find that the transmission performance decrease with the thinner the metasurface. The resonating frequency will shift gradually with the decrease of the thickness. Compared with the roughness, the shape of the transmission curve remains sharp, which means that the impact of the thickness various is relatively weaker than the roughness if the conductivity is high and stable.

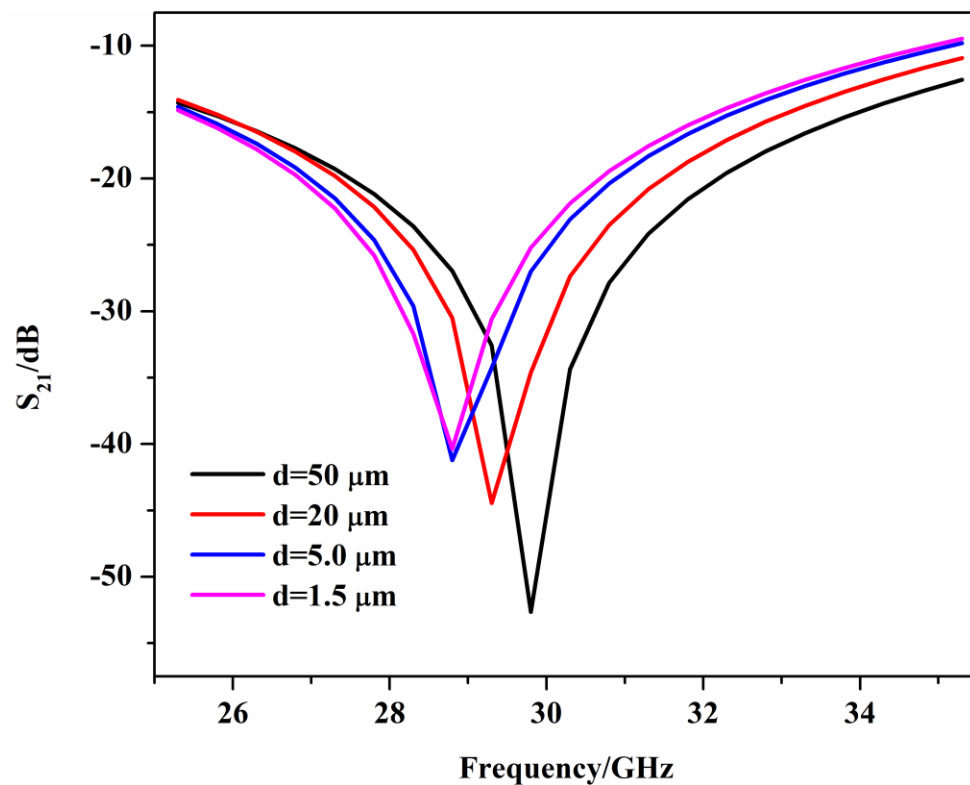


Figure 32 The influence of thickness on the transmission performance of the metasurface.

Chapter 3

3. Fabrication of metasurface with printing electronics

In this chapter, the fabrication of the metasurface will be discussed. Digitalized reaction on demand (DRoD) method, a low cost, high through output and fast prototyping method has been applied to realize the designed metasurface and overcame some challenges of current printing electronic technology.

The core idea of printed electronics technology is to produce circuitries and electronics elements, just like paper printing in the printing industry. The printed electronic technology is based on the basic equipment and manufacturing process of traditional printing technology, like inkjet printing, screen printing, gravure printing, transfer printing, extrusion printing and laser printing. However, new printing mechanisms, inks, substrate treatment, and post-treatment processes have been developed to generate customized, colorful, flexible, wearable, and stretchable electronic elements even devices. Due to the high adaptability and digitalization of the printing process, inkjet printing gained remarkable attention in the printed electronics industry.

Nanoparticle inks are a suspension of nanoparticles in liquid mediums, either in an organic solvent such as ethanol, toluene, ethylene glycol, or inorganic solvent like water[10]. The rapid development of the conductive metal nanoparticle inks which hold the advantage of relatively high conductivity promoted the inkjet printing to be a competitive technology in the production of electronic components. However, the applications of metal nanoparticle inks are subjected to the complex and strict production process, which resulted in high cost and limited production scale compared with the metal salt. During the printing process, agglomeration of the suspended particles will increase ink's viscosity and can result in clogging of the print head nozzles. To form patterns with good conductivity after the printing process, most of metal nanoparticle inks require various post-treatment, such as heat sintering in low or high temperature[61], laser annealing[62], and chemical sintering[63]. The post-treatment process extended the fabrication period and increased cost.

Drop on demand (DoD) inkjet printer is based on the concept that droplets are only formed and ejected when demanded. Every single droplet is under manipulation in this process. Inspired by this concept, the reduction reaction of the metal ions can also be realized in the droplet level. Every single droplet can perform as a reaction unit. When the substrate is treated by a proper reduction agent, the metalized pattern can be digitally physicalized through the printing of the metal salts solution. We call it the digitalized reaction on demand method (DRoD). This method is developed from Tengyuan Zhang's reaction on demand method, which is a simple but powerful approach to fabricate flexible electronics via direct writing technology[64]. As a fast prototyping technique, DRoD method will obtain popularity in flexible electronics for its high digitalization, low-cost, simplicity, scalability and commercialization potential.

3.1 Fabrication of EM wave selective reflection metasurface via DRoD method

The fabrication process of metasurface via the DRoD method consists of the following three steps. First, prepare a thin ink absorption layer of PVA/SiO₂ nanoparticle polymer composite solution through the Mayer rod coating on the PET and paper substrate. We can also choose PET or paper with pre-coated ink accepting layer for inkjet printing[65]. Second, using the Mayer rod coating to build a reduction layer to functionalize the ink absorption coating, ascorbic acid (Vitamin C, Vc) solution was applied here. Last, the metasurface was printed by inkjet printing of high loading silver nitrate ink to react with the reduction functional layer, instantly showing the designed pattern with a metal-polymer structure. Most of the silver nitrate ink was reduced into the non-toxic silver, which will not lead the environment issue in the application process.

3.1.1 Preparing of the ink absorption layer

Materials: PVA ($M_w \approx 40\,000$, 98-99% hydrolyzed) was purchased from Alfa Aesar; Aqueous alumina dispersions (solid content: 30%, pH:3.0-5.0, viscosity: <2000 mPa, density: 1.26 g/cm^3) and aqueous silica dispersions (solid content: 24%, pH:5.0-6.0, viscosity: <150 mPa, density: 1.15 g/cm^3) were purchased from AERODISP; DI water.

Preparation of Solution: PVA (2.5 g) was dissolved in DI water (47.5 mL) with continuous stirring with 200 rpm for 48 h at $80\text{ }^\circ\text{C}$ to form a clear, transparent solution with 5 wt%. The absorption coating solution is prepared by mixing the PVA with aqueous silica dispersions with the volume ratio of 1:4, then stirring for 2 hours at room temperature to form a uniform solution.

Coating of the ink absorption layer:

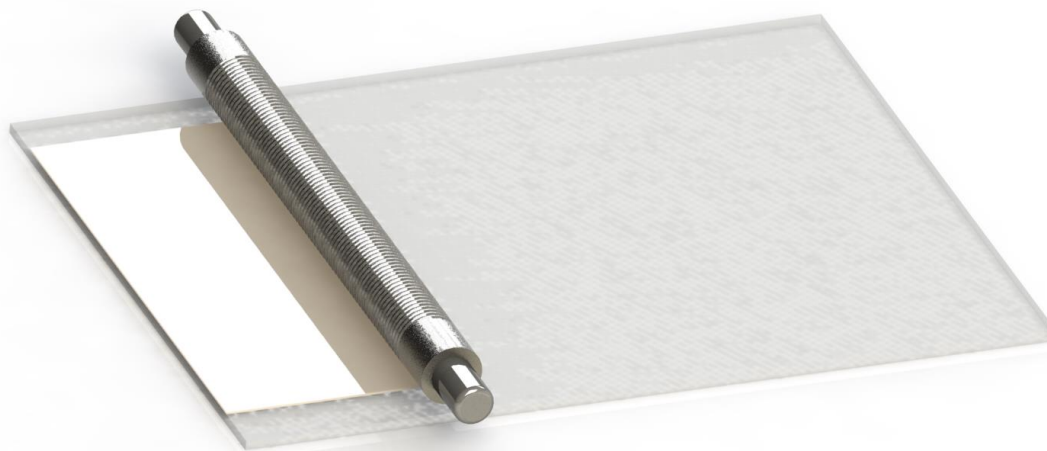


Figure 33 Schematic of Mayer rod coating.

The Mayer rod coating is illustrated by **Figure 33**. A uniform layer can be coated by the Mayer rod coating via the control of Mayer rod. The ink absorption solution was coated using the Mayer rod coating machine (TMAX-XT-200CA, Xiamen Tmax Battery

Equipments Limited, shown in **Figure 34**) with wires size from 0.2 to 0.8 mm (The Paul N. Gardner Company, Inc. (GARDCO)). The coating speed is 1.2 m/min. For the A4 size substrate, 2 ml of coating solution was used for every coating process. Then the coated films dried at 80 °C in the oven.



Figure 34 Mayer rod coating machine (TMAX-XT-200CA, Xiamen Tmax Battery Equipment Limited).

3.1.2 Preparing of the reduction functional layer

Materials: ascorbic acid (99%), xanthan gum ($(C_{35}H_{49}O_{29})_n$, 98%) were purchased from Sigma-Aldrich; Ethanol was purchased from the Greenfield Global; DI water.

Solution preparation: 0.4 g xanthan gum was dissolved in 200ml DI water with stirring for 8 h at 500 rpm on the hot plant at 120 °C to form a 0.2% (w/t) xanthan gum solution (**Figure 36**). Xanthan gum solution mixed with ethanol with 4:1 and Vc dissolved in the mixed solution with concertation of 0.25 g/ml followed by stirring for 20 min at 100 rpm at room temperature. The viscosity of the Vc solution is 418 mPa*s.

Coating of the reduction functional layer: Coating the Vc solution on the ink absorption layer by Mayer rod coating machine wires size from 0.2 to 0.81 mm. The thickness of the coated layer can be controlled by the Mayer rod size, shown in **Table 1**. The coating speed is 1 m/s. For every coating process, 2 ml Vc solution is used. A mirror like film can be generated by the Mayer rod coating. The coated wet film dries in the air in 2 hours (**Figure 35**).



Figure 35 Wet film of the Vc coating with the mirror-like surface.

Table 1 Parameter of the Mayer rod used in coating

Wire Size #	Metric (MM)	Maximum Wet Film Thickness (Microns)
8	0.20	20.6
16	0.41	42.2
24	0.61	61.5
32	0.81	82.0

**Figure 36 Xanthan gum solution.**

3.1.3 Printing of the Ag salt ink

Materials: silver nitrate (AgNO_3 , 99%) was purchased from Sigma-Aldrich; anhydrous glycerol ($\text{C}_3\text{H}_5(\text{OH})_3$, 99%) was purchased from Fisher Scientific. Dynol 604 Surfactant was purchased from Evonik; ethanol; DI water.

Ink preparation: DI water, glycerol and ethanol were mixed with the ratio of 112:70:8 to form a clean solution. 0.025% of Dynol 604 was added into the mixture solution above to form a base solution for the ink. 1.2 g silver nitrate was dissolved into the base solution by using the vortex mixer (VWR) with power level 8 for 10 minutes (**Figure 37**). The silver ink was filtered by a 0.2 μm nylon syringe filter.

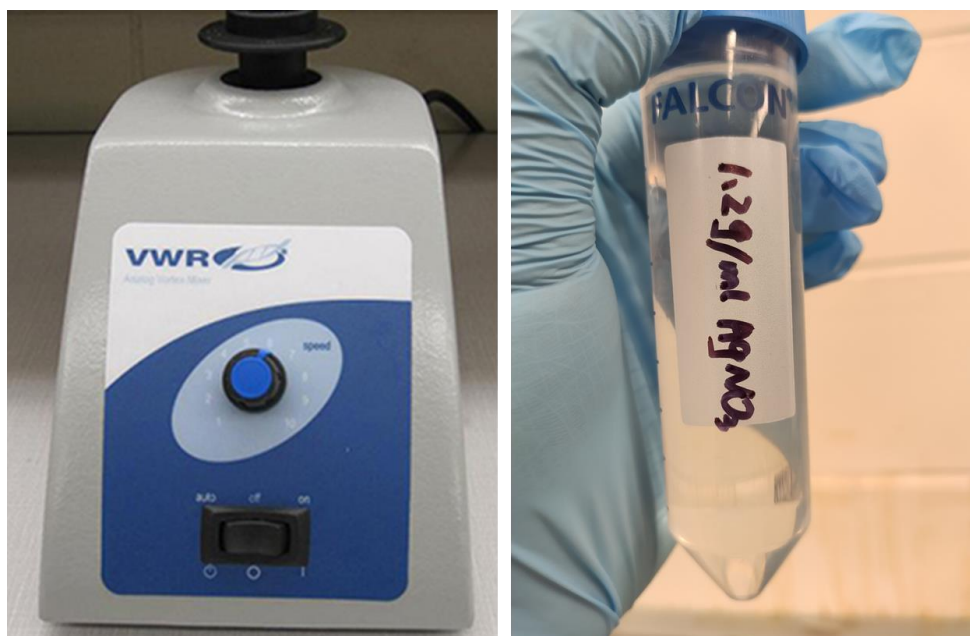


Figure 37 Vortex mixer from VWR (left) and prepared AgNO_3 ink (right).

Cartridge filling: empty replaceable ink cartridge was purchased Epson (**Figure 38**). The number of cartridge nozzle is depended on the function of “black” or “color”. The ink output can also be different. 8 ml silver ink was filled into the ink cartridge by syringe each time. Check the working condition of the cartridge before printing to avoid nozzle blocking.



**Figure 38 Ink cartridge from Epson. 59 nozzles are integrated into color print head.
The black print head has 180 nozzles.**

Printing: The printer Epson C88+ was purchase from Epson (**Figure 39**). It is based on the CMYK drop-on-demand Micro-Piezo inkjet technology. Minimum ink droplet size: 3 picoliters. Highest resolution: 5760 * 1440 dpi. The configuration of the metasurface is digitalized via CorelDraw X7. Put the reduction functionalized PET or paper substrate in the paper entrance position of the printer. Then, just click the “print” bottom. The printing speed is 2 pages per minute. A batch of 30 pieces of metasurface can be printed continuously in 15 minutes by simply clicking on the “print” bottom. The whole printing process is conducted under room temperature (20-25 °C), with a humidity level of 40-60%.

Post-treatment: no post-treatment is needed in the DROD method.

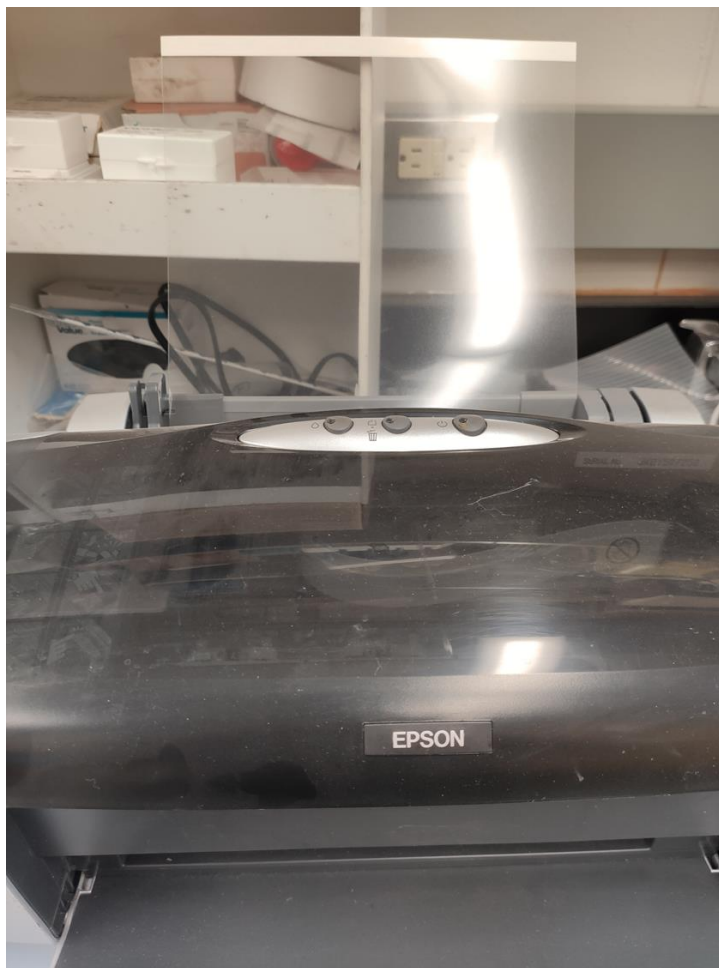


Figure 39 Epson C88+ printer.

3.2 Printing results and characterization

DRoD shows its advantage of high material efficiency, low cost, fast prototyping, scalability, and green process in the whole process. Such a method has high adaptability in different substrates, including transparent PET, paper even silicone rubber. High-performance metasurface was printed with similar conductivity and resolution on transparent PET (**Figure 40**), paper (**Figure 41**) and silicon rubber (**Figure 42**). The printed metasurface can maintain high performance in the air and after water treatment.

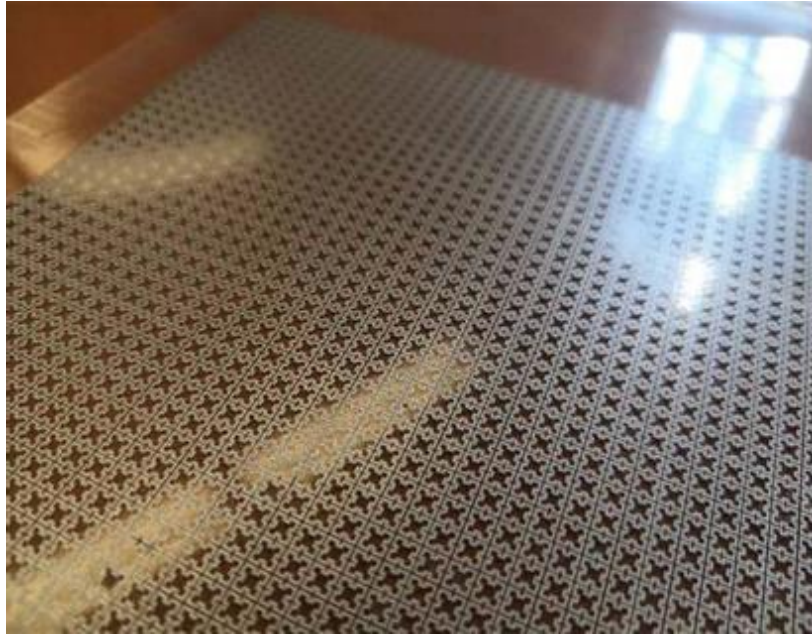


Figure 40 Printed metasurface on transparent PET substrate

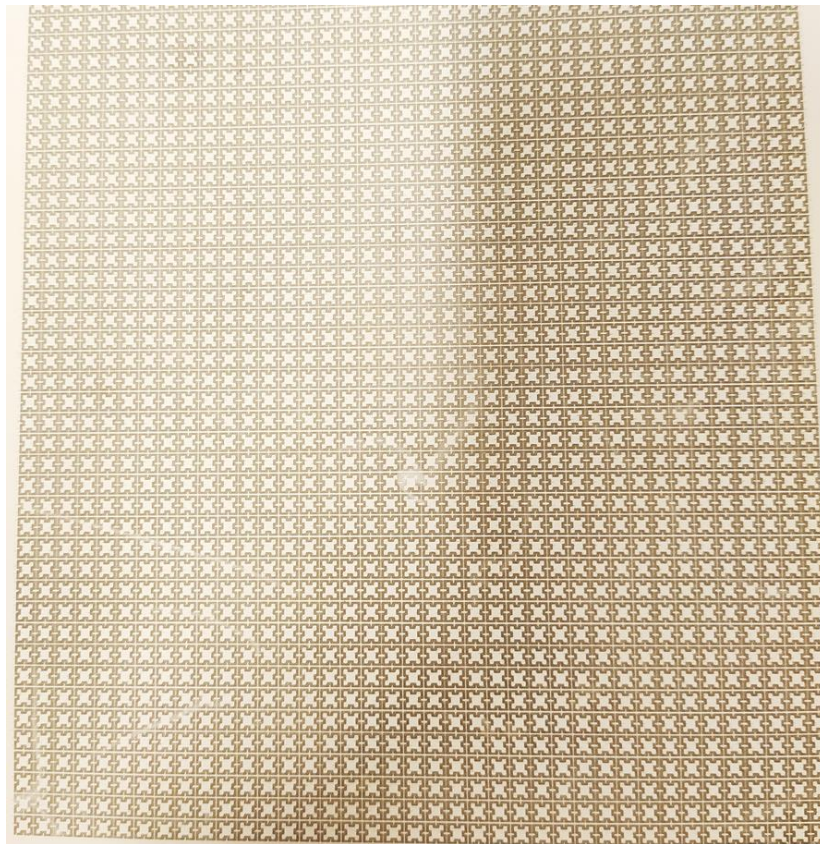


Figure 41 Printed metasurface on the paper substrate

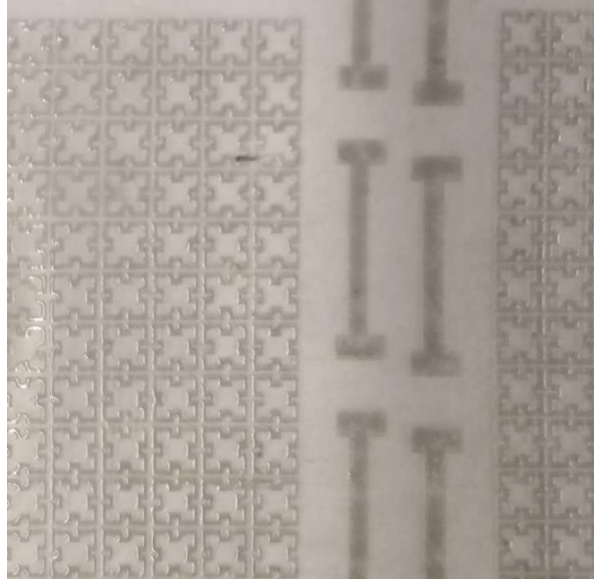


Figure 42 Printed metasurface structure and conductivity test unit on the silicon rubber substrate.

Table 2 Basic parameters of the printed metasurface

Parameter	Data
Film Thickness	~120 μm
Coating Thickness	~30 μm
Metasurface Thickness	~4.5 μm
Sheet Resistance	20.96 $\text{m}\Omega/\text{sq}$
Conductivity	$1.06 \times 10^7 \text{ S/m}$

The surface property of the substrate will affect the color of the printed patterns. For the transparent PET and silicon rubber substrate, the surface is smoother than the paper substrate, and metallic luster can be observed from the metasurface. For the paper substrate, due to the surface fiber structure, the reflection of the silver structure will be affected, which leads to a dark silver color.

The assistance structure was also printed for measurement and characterization (**Figure 42**). Basic parameters are shown in **Table 2**, including the conductivity, sheet resistance, substrate thickness (PET) and reduction layer thickness. The surface configuration was analyzed via Optical microscopy and scanning electron microscopy (SEM). In **Figure 43**, we find a good agreement between the designed and printed sample parameters. Due to the limitation of the printer, the roughness was observed in the y-direction. Resulted by the difference of surface properties, the surface morphology of printed metasurface on PET substrate (**Figure 44**) and paper substrate (**Figure 45**) is slightly different. The surface roughness of the paper substrate leads to a highly diverse distribution of size and configuration of the silver nanostructure compared with the PET substrate.

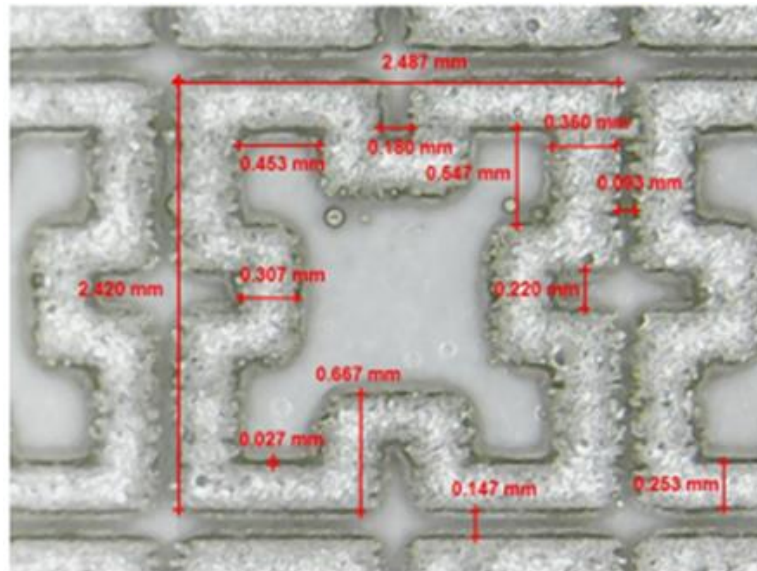


Figure 43 Optical microscopy image of printed metasurface unit cell.

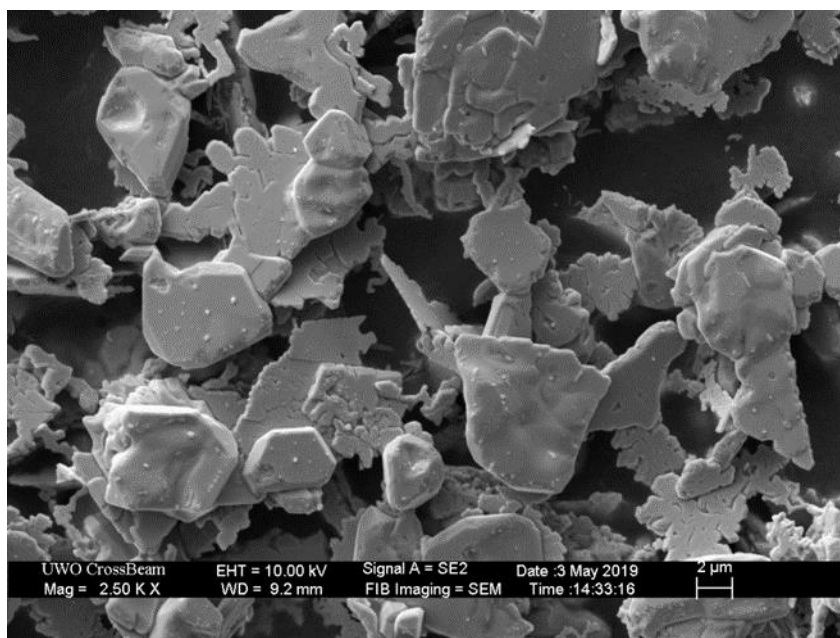


Figure 44 SEM images of the surface morphology of silver flake on PET substrate.

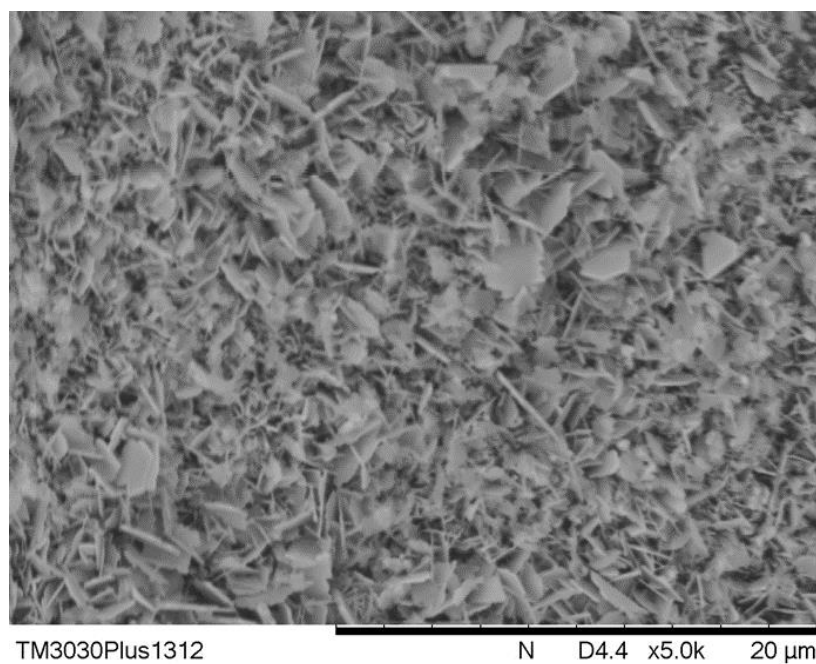


Figure 45 SEM images of the surface morphology of silver flake on paper substrate.

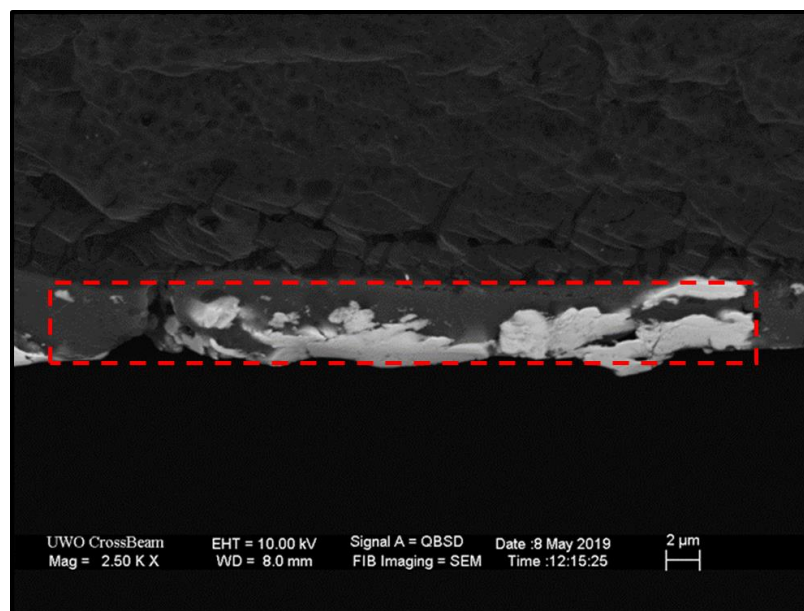


Figure 46 SEM image of the cross-section of the silver-polymer layer, which has the thickness of ~4.5 μm .

The water-swelling property of PVA provides space to accept the Mayer rod coated ascorbic acid solution. The silica nanoparticles can lead to a mesoporous structure in the reduction functional layer. The ink droplet can diffuse into the 3D reduction functionalized mesoporous structure immediately and trigger the reaction from the surface to the whole reduction film. A silver-polymer conductive layer can be generated rapidly (**Figure 46**). From the SEM image, we can find that the silver flakes with a diameter of more than 5 μm were densely distributed on the substrate. Interestingly, the silver wire was found due to the fiber structure on the surface of the paper substrate. The microfiber of the paper was covered by the reduced silver. The overlap and intercross of the silver nanofiber are beneficial to decrease the surface resistance.

3.2.1 Measurement of conductivity

From the simulation results, the conductivity of the metasurface is a key factor to influence transmission performance. The Four-point collinear probe method was applied to measure the conductivity (**Figure 47**)[66]. Due to the feature size limitation of the printed metasurface, the printed test units were also measured to obtain an accurate and reliable result.



Figure 47 Model 2450 SourceMeter SMU Instrument with the Lucas/Sigmatone Corporation (Gilroy, CA), Model SP4 4-Point Probe Head and S-302 Test Stand measuring the conductivity of a sample.

3.2.2 The influence of Ag loading on the conductivity

To figure out the influence of the Ag ink concentration, the saturate Vc solution as the reduction layer was coated. From the measured results from **Figure 48**, we find that the conductivity increases with the increasing loading of the silver ink. Three stages were observed in the whole process. The surface morphology and the thickness of the metal-polymer hybrid structure have huge impact on the conductivity.

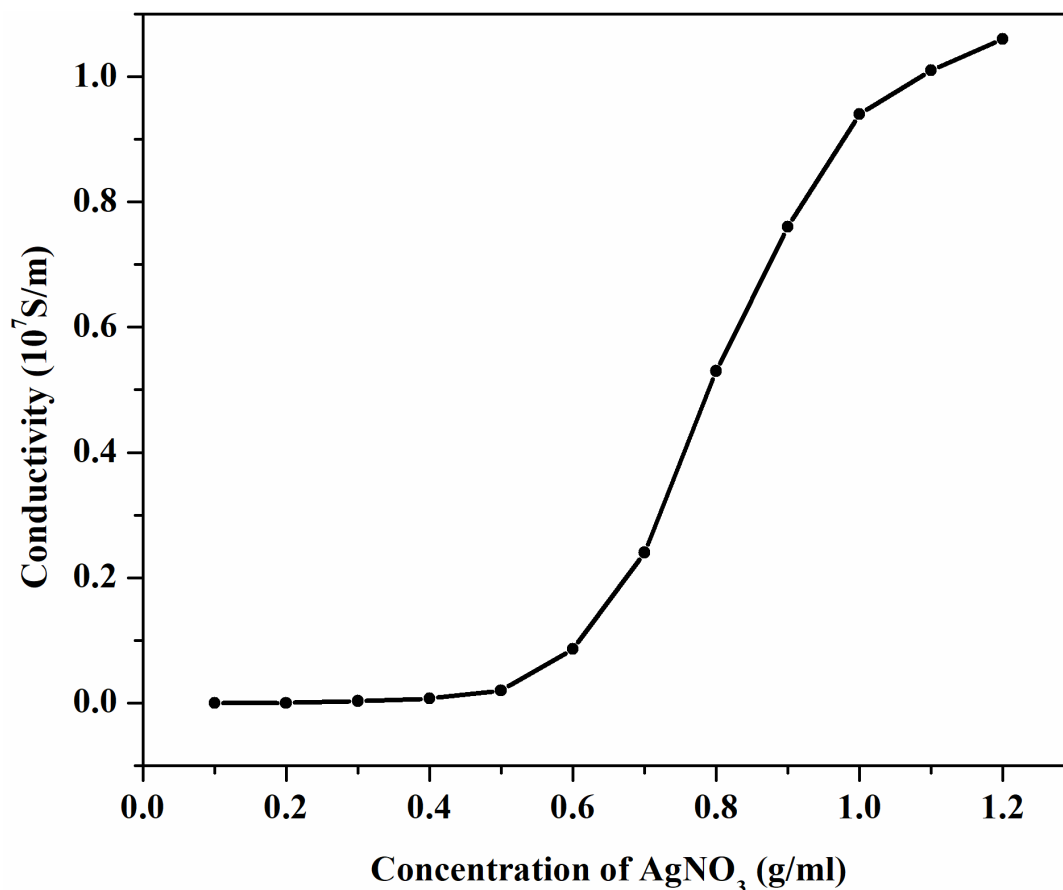


Figure 48 The influence of the Ag ink concentration on the conductivity of the metasurface.

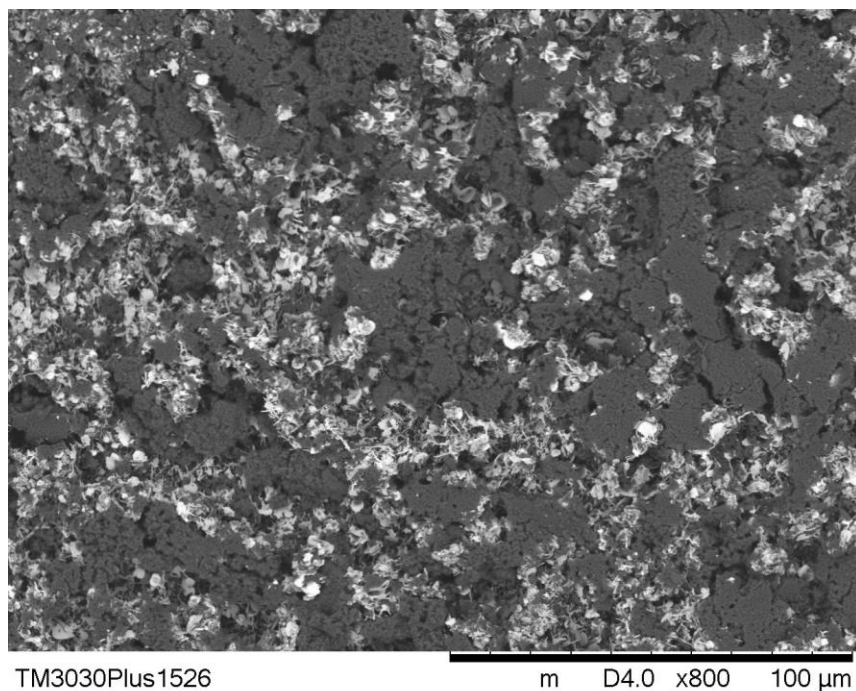


Figure 49 Surface morphology of the metasurface when silver nitrate concentration is 0.1 g/ml.

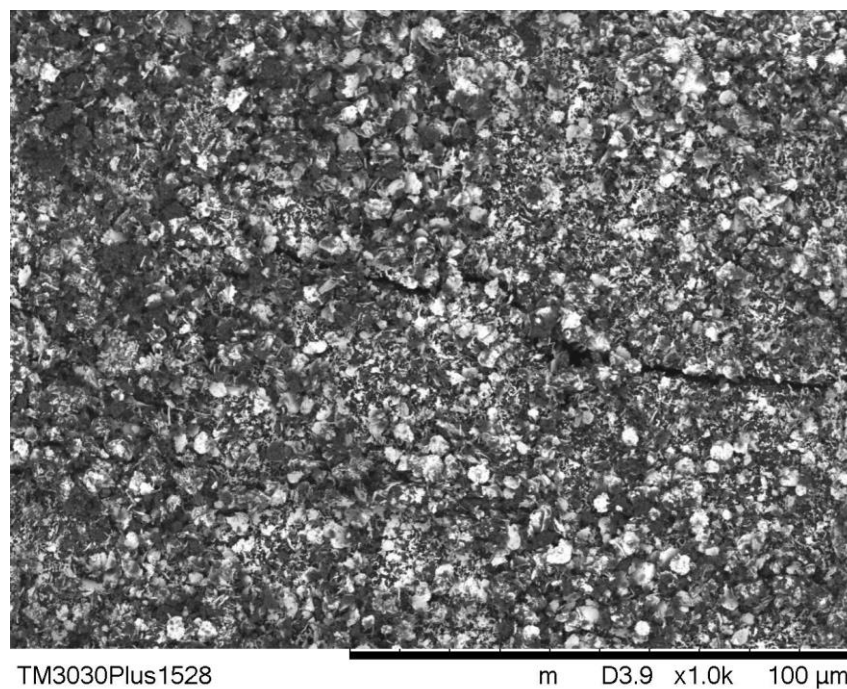


Figure 50 Surface morphology of the metasurface when silver nitrate concentration is 0.8 g/ml.

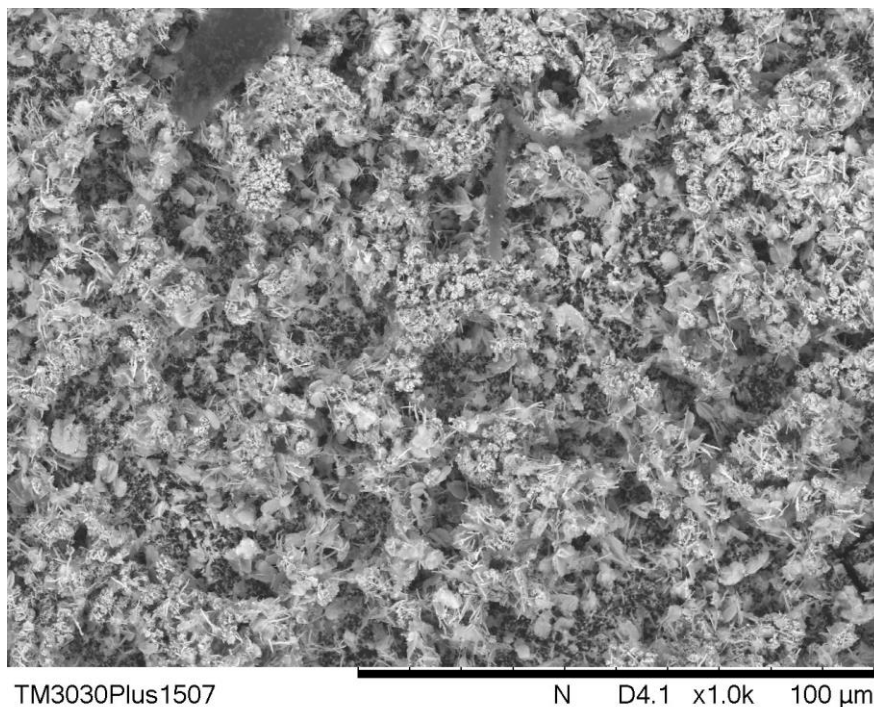


Figure 51 Surface morphology of the metasurface when silver nitrate concentration is 1.2 g/ml.

In the region of 0.1 to 0.5 g/ml, the increase of conductivity is slow. It is resulted by low silver loading can't generate continuous silver layer (**Figure 49**). Shown in **Figure 50**, with the further increase of the silver loading, the density of the silver flake is getting higher and the conductivity increasing rapidly with the thickness of the metal layer also getting higher. After the Ag^+ concentration is higher than 1 g/ml, the dense silver layer is formed, like in **Figure 51**. But the conductivity increasing gets slower with the further increase of silver concentration. For a high loading silver ink, ink droplets will perform the more dramatic reduction reaction and generate silver flakes more rapidly. Depended on the pattern design and printing mode, the printing head will scan each target point for specific times to jet the ink droplet as demanded. The silver plates formed in the beginning stage will naturally hinder the further reaction. As a strong electrolyte, the increasing concentration of silver nitrate will increase the surface tension of the ink, which limited the further increase of the silver loading to maintain good printability[67].

3.2.3 The influence of Vc concentration

As the functional material of the reduction layer, Vc will influence the reduction ability with different concentration. We set the gradient of Vc concentration from 0.05 g/ml to the saturated solution (0.33 g/ml at room temperature) to explore the influence of Vc concentration. In the printing process, the silver ink concentration was as 1.2 g/ml.

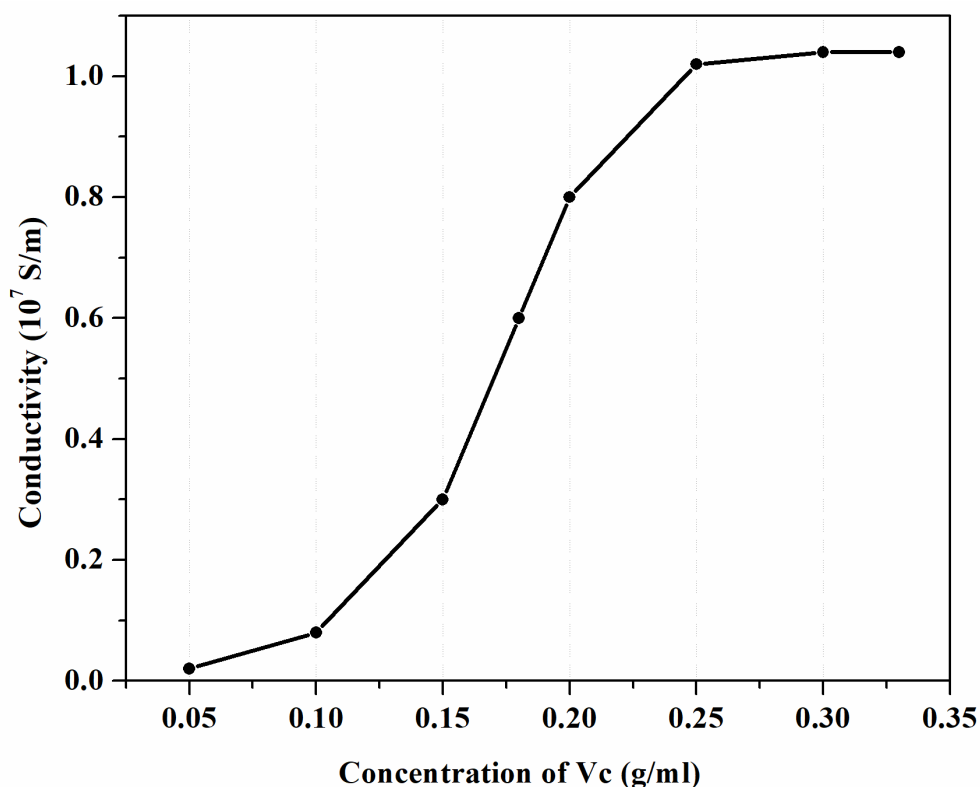


Figure 52 The influence of the Vc concentration on the conductivity of the metasurface.

From the results illustrated in **Figure 52**, we find that the increase of Vc concentration will improve the conductivity in low concentration level. A z-shape relationship was noticed. With the increase of Vc loading, the reduction reaction with the ink will be more thorough. When the concentration is higher than 0.25 g/ml, the improvement of the conductivity is negligible, which is resulted from no enough silver ink to react with the reduction layer. The remained Vc will have an oxidation reaction with oxygen in the air, which will cause

the yellow color on the surface. Based on the above results, the concentration of 0.25 g/ml is a proper choice to obtain low resistance, maintain stability and save raw material.

3.2.4 The influence of the ink absorption layer

The ink absorption layer consists of PVA and silica nanoparticles. The PVA extends the reaction depth from the surface to a 3D structure. The silica nanoparticles can enhance the ink absorption ability via the mesoporous structure, which can increase the thickness of the conductivity layer. But the crack can also be induced with the increased content of silica nanoparticles (**Figure 53**).

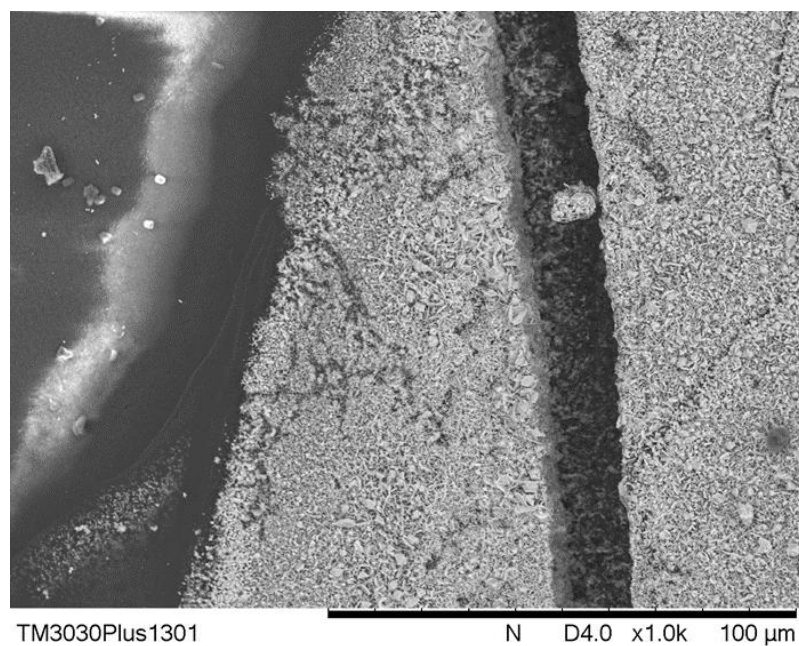


Figure 53 Surface crack induced by the high silica content after solvent evaporation.

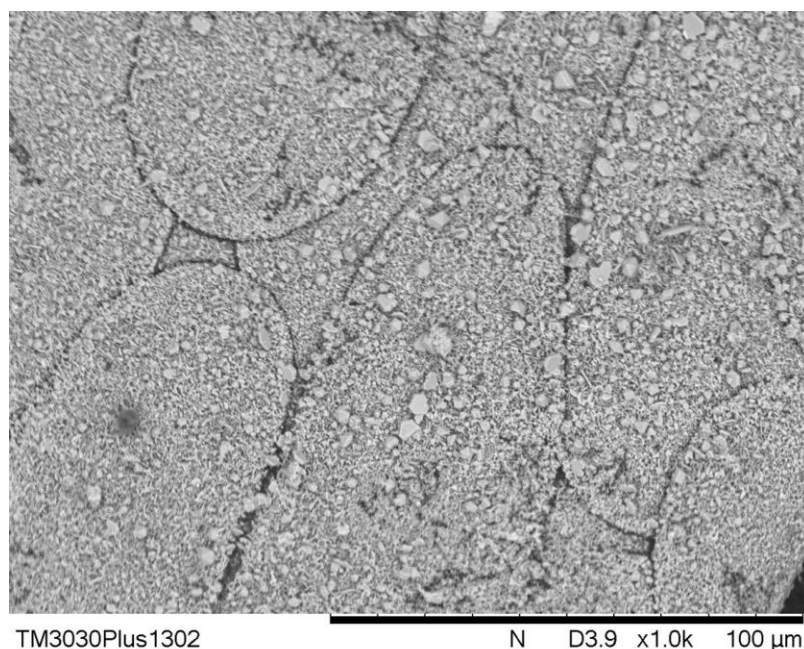


Figure 54 Improved surface morphology after the adjustment of the content of silica nanoparticles.

A series of experiments were conducted to explore the best formulation of the ink absorption layer. The ratio of the solid content will be the core idea since both PVA solution and silica dispersion are water solution (shown in **Table 3**).

Table 3 Influence of the solid content on the printing results

PVA:Silica	1:0.6	1:0.8	1:1
Conductivity (10^7 S/m)	0.85	1.02	0.92
Crack or not	Not	Not	Crack

From the conductivity measurement and the surface morphology characterization, we can get the conclusion that when the solid content ratio of PVA and silica equal to 1:0.8, we get the ideal results in both high conductivity and uniform surface morphology (**Figure 54**). As a flexible electronic device, the surface property can greatly influence the mechanical performance, especially for bending and aging.

3.2.5 Modification of the silver ink

To realize high-quality printing, some essential requirements must be met at the same time. First, the silver ink should be adaptable to the inkjet printers, which means ink formulation should match the required physical parameters like viscosity and surface tension to realize the best working condition[68]. Second, to improve the conductivity of printed metasurface, the conductive ink should have a high loading silver content. Third, the ink should be chemically stable in the air. The oxidation should be suppressed. Last, the ink should be environment friendly. No water or air pollution will be caused in the whole process, from ink preparation to printing and final products.

Due to the high silver nitrate solubility, water is the best solvent choice for the DRoD method. But the viscosity of the silver nitrate is lower than the requirement, and the surface tension is too high. Glycerol is a good choice to adjust the viscosity. A commercialized surfactant, Dynol 604 was dissolved in ethanol to form a surface tension adjusting solution. In the finalized ink formulation, 0.025% of Dynol 604 was used to further formulate the ink to have the competitive performance of the native packed ink for printers (shown in **Table 4**). The loading of the silver solution was maintained at 76.2% (w/v), which is higher than most of the silver ink in the market. A high silver concentration will increase the surface tension, but the high level of surfactant will induce the precipitate of the salt[69], which limits the further improvement of silver loading.

Table 4 The parameters of the high loading silver ink

Parameters	Data
Viscosity	3.2 cp
Surface tension	33.0 mN/m
Density	1.8 g/cm ³
Silver loading	76.2% (w/v)
Surfactant loading	0.025%

3.2.6 Stability of the printed metasurface

The stability of the printed metasurface will greatly influence their application in communication, especially for outdoor facilities. To evaluate the conductivity stability in the ambient condition, we measured the conductivity σ continuously for one month to compare with the initial conductivity σ_0 .

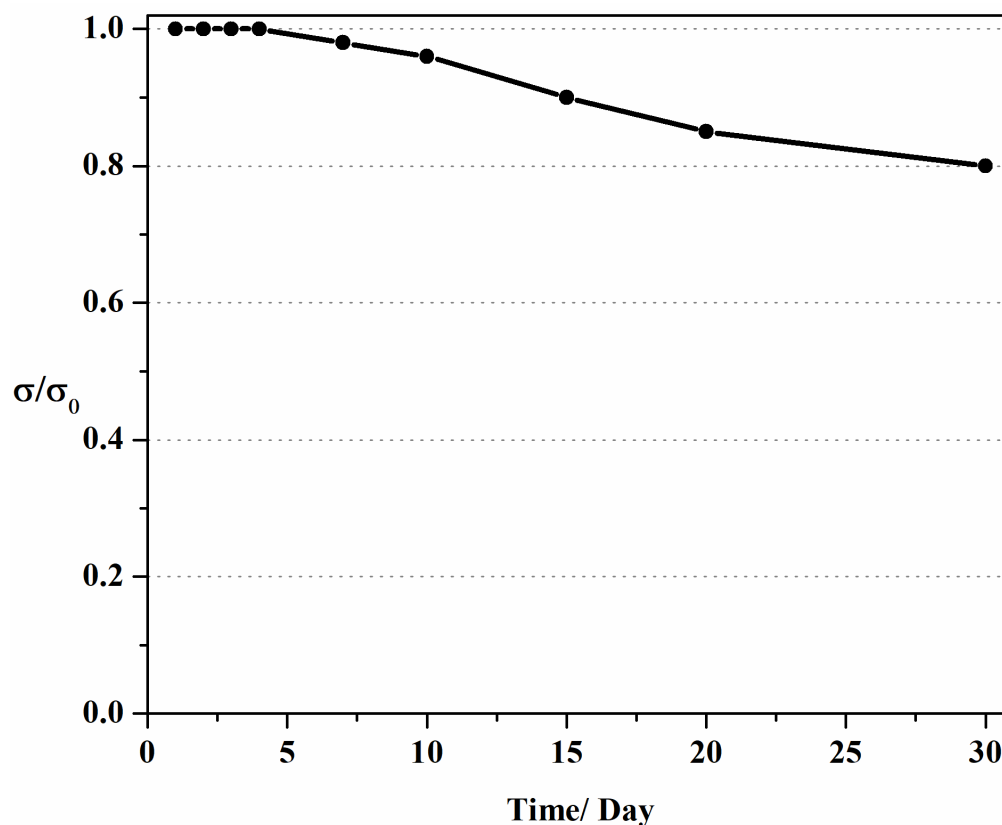


Figure 55 Conductivity of the printed metasurface stored in ambient condition.

From the results shown in **Figure 55**, we find that the conductivity remained high (80%) after one month. No decreasing was found in the first few days, which create a window to make the encapsulation for the large-scale applications in the future. The probable mechanism for conductivity degradation is the oxidation of the silver nanoparticle. From the XRD spectra of the freshly prepared sample and half year stored sample from the previous work, the peak of Ag_2O gets stronger after the long-term storage(**Figure 56**) [64]. The peak of Ag keeps strong in the whole process, which means that the silver-polymer structure can stay relatively stable in air.

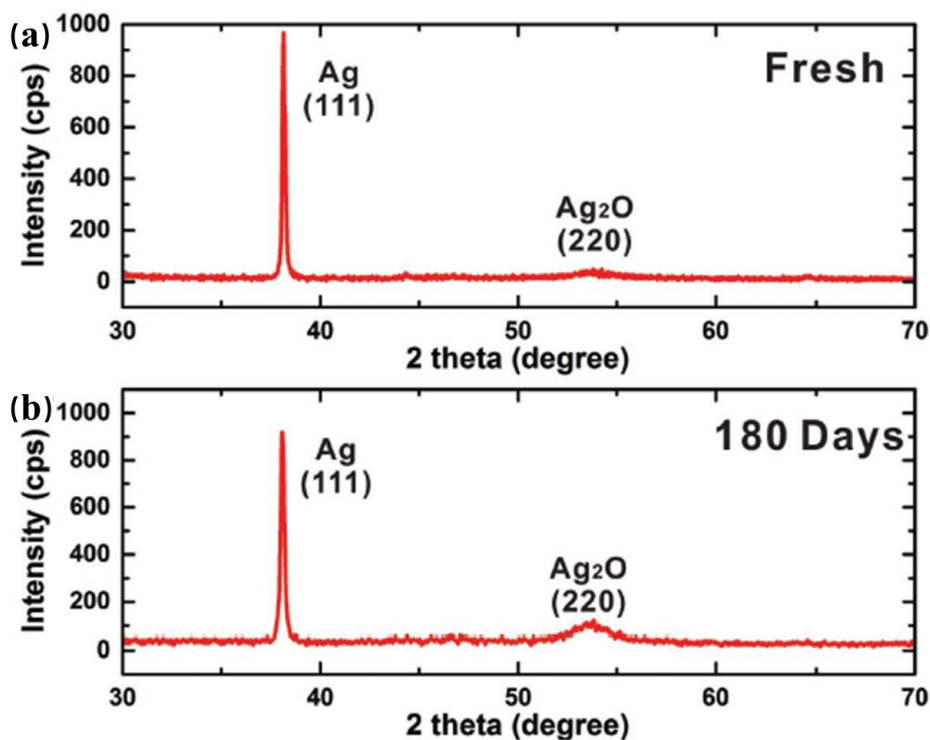


Figure 56 X-ray diffraction (XRD) spectra of a) freshly prepared sample; b) after stored in air for 180 d (Reprint from [64] with permission).

To meet the requirement of the outdoor applications, we tested the stability of the metasurface under the water and steam treatment to verify that the metasurface can remain working even the encapsulation failed.

For the water treatment, we coat a water film via Mayer rod coating to simulate the situation of water penetrate the encapsulation in the heavy rain. After the evaporation of the water, we measure the conductivity of the metasurface. The conductivity was recorded after one month.

The metasurface fabricated via DRoD exhibited strong stability in the water treatment test. After the water treatment, the silver-polymer structure wasn't washed away. Shown in **Figure 57**, the geometry of the printed metasurface didn't change. From the measured results in **Table 5**, we are surprised to find that the conductivity even increased after the water treatment. In **Figure 58**, we can find that silver nanoparticles were generated after the water treatment. As we discussed above, high loading silver ink can lead a little portion

of silver ink holding inside the silver layer. After the solvents were evaporated, the reaction stopped. The water treatment active the reaction via re-dissolve the remained silver nitrate molecule and Vc. Silver nanoparticles can be formed along with the preformed silver flake or silver covered fiber. The existence of water film is beneficial to the improvement of the conductivity instead of destroying the surface structure. One month after the water treatment, the conductivity decreases just like the untreated sample, even with slightly better performance.

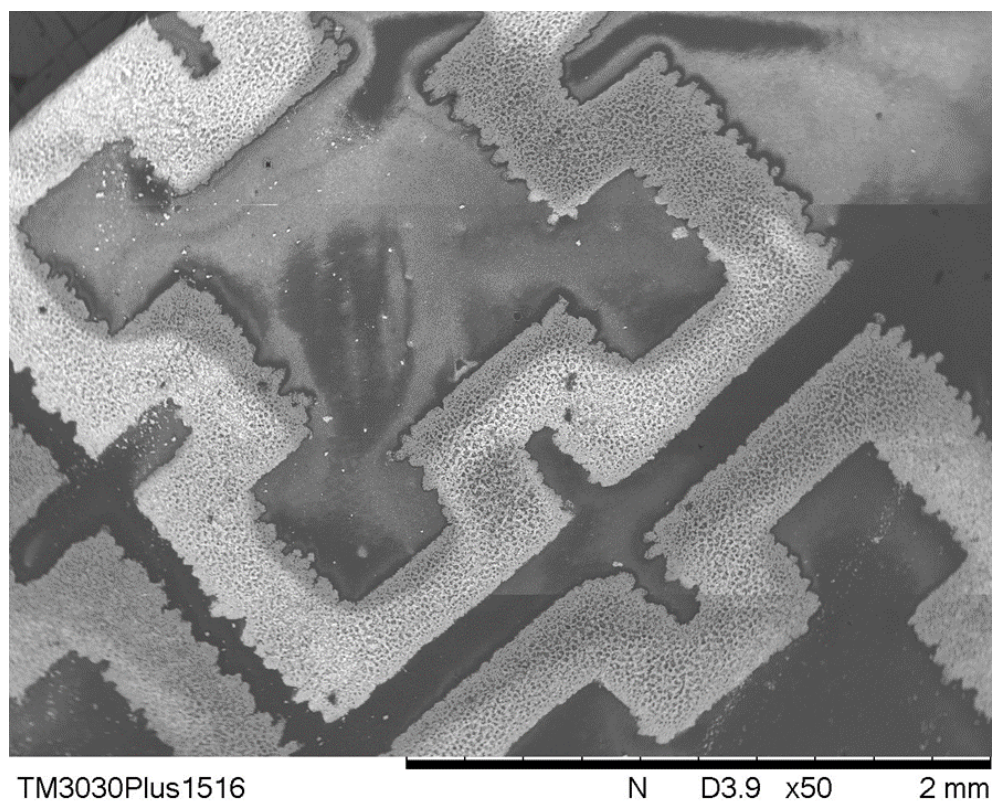
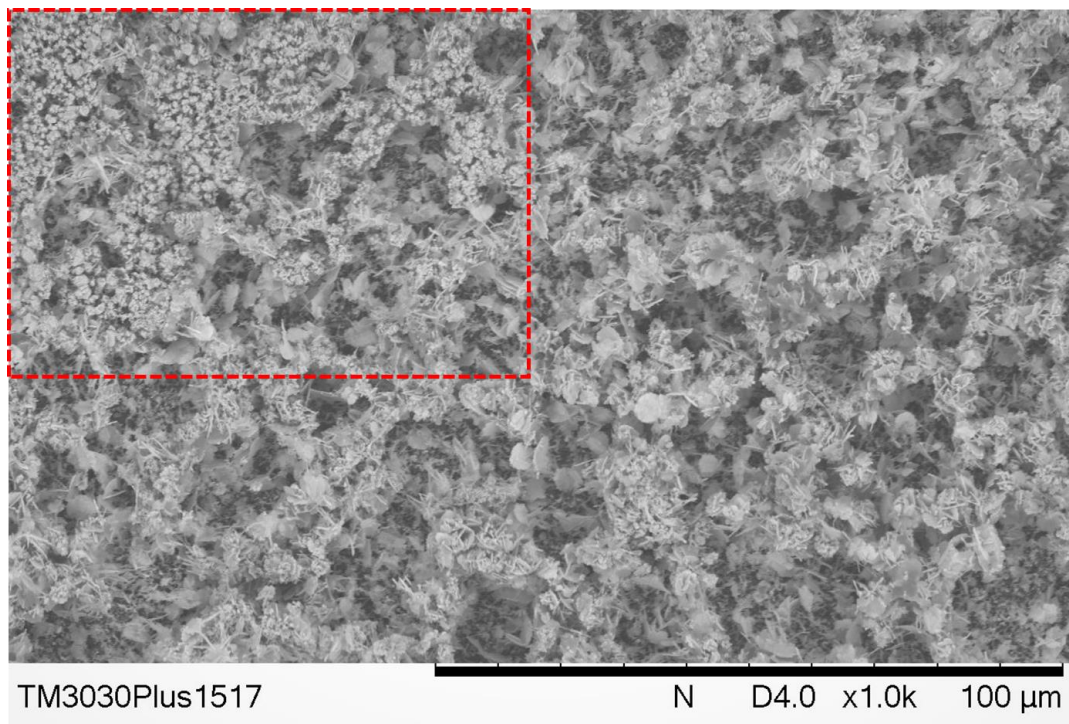


Figure 57 SEM image of the metasurface unit cell after water treatment.

Table 5 Conductivity during water treatment test

Stage	Before water treatment	1 hour after water treatment	1 month after water treatment
Conductivity (10^7 S/m)	1.02	1.06	0.82

**Figure 58 Silver nanoparticle generated after water treatment**

In the summer of the Great Lakes region, it is common to experience the high humidity outdoor environment. The steam treatment was designed to simulate the extreme working environment for the printed metasurface sample. We generate a steam environment by heating the water to 80 °C in the thermostatic water bath. The printed metasurface was treated by the hot steam for 3 minutes without protection. After the steam bath test, the surface morphology was recorded and the conductivity was measured.

During the high-temperature steam treatment, the surface structure of the metasurface stay stable and sliver flakes densely covered the substrate in the whole test process, shown in **Figure 59**. Similar to the water treatment test, the conductivity of the metasurface increase slightly after the steam bath test, which shows in **Table 6**. Compared with water treatment, the high-temperature steam bath can make the remained Vc on the substrate will decrease its reduction ability, which limited the further reduction reaction.

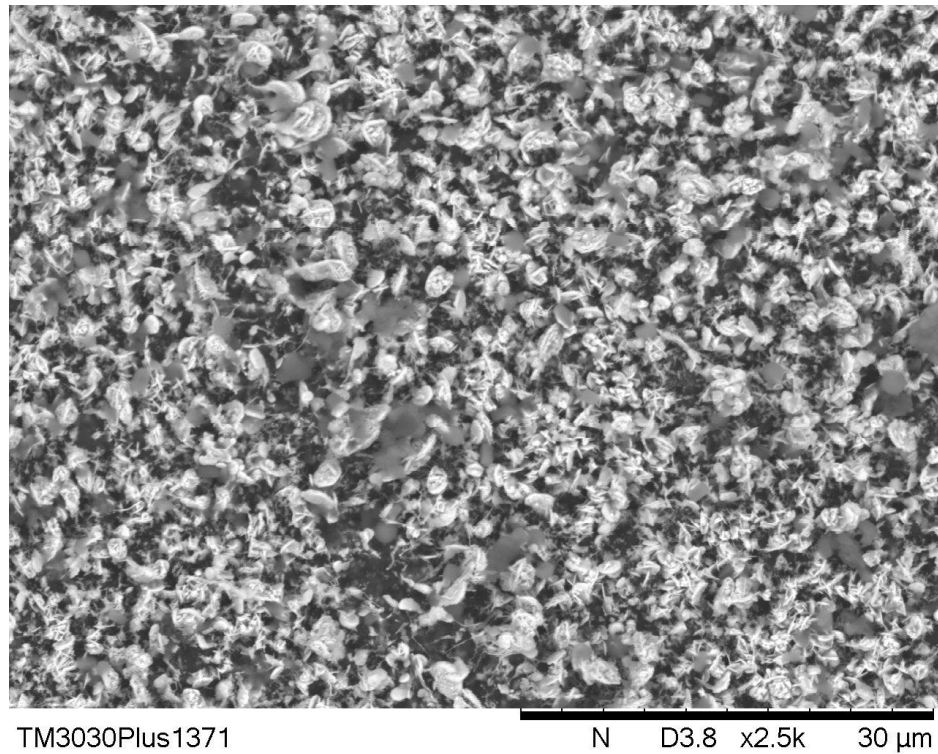


Figure 59 Surface morphology of the metasurface after the steam bath.

Table 6 Conductivity during steam bath test

Stage	Before steam bath	1 hour after steam bath	1 month after steam bath
Conductivity 10^7 S/m	1.02	1.03	0.81

Overall, the printed metasurface shows high performance in the stability test in the air and some extreme conditions, especially in the water related test. The raising of the conductivity with the participation of water film and steam is an interesting result. Further research can be conducted to make a better manipulation for the water assistance with the combination of the surface treatment, like hydrophobic or hydrophilic treatment, to design a novel printing method to fabricate the flexible electronics with high conductivity and finer feature.

3.2.7 Demonstration of the roll to roll printing based on DRoD method

Roll-to-roll (R2R) processes work as an advanced manufacturing platform that has great potential for continuous and large-scale production for the deposition of diverse materials on flexible substrate rolls[70]. It is regarded as the most promising fabrication technology for flexible electronics through the combination of multifunctional solution-based printing and coating processes[71]. Inkjet printing is ideal for the R2R process with the advantages of digitalization, controllable, and adaption for high volume manufacturing[72].

Based on the Mayer rod coating and inkjet printing, the DRoD method is a compatible method for the roll to roll printing. To demonstrate this concept, we build a roll system which can feed a roll of reduction functionalized PET substrate into the inkjet printer (**Figure 60**). Roll samples of metasurface with high performance were printed (**Figure 61**).



Figure 60 Demonstration of the R2R process for the DRoD method.

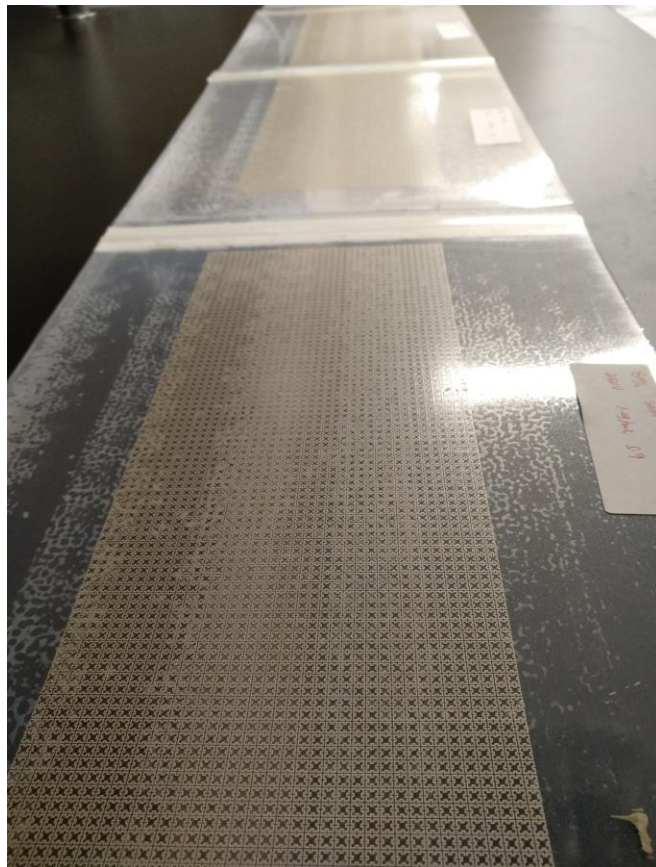


Figure 61 Roll sample of metasurface fabricated by the roll to roll process of DRoD method.

The roll to roll printed metasurface shows the almost the same surface morphology (**Figure 62**) and competitive performance with the piece to piece method, which proved the possibility of transferring the DRoD method from lab to fab.

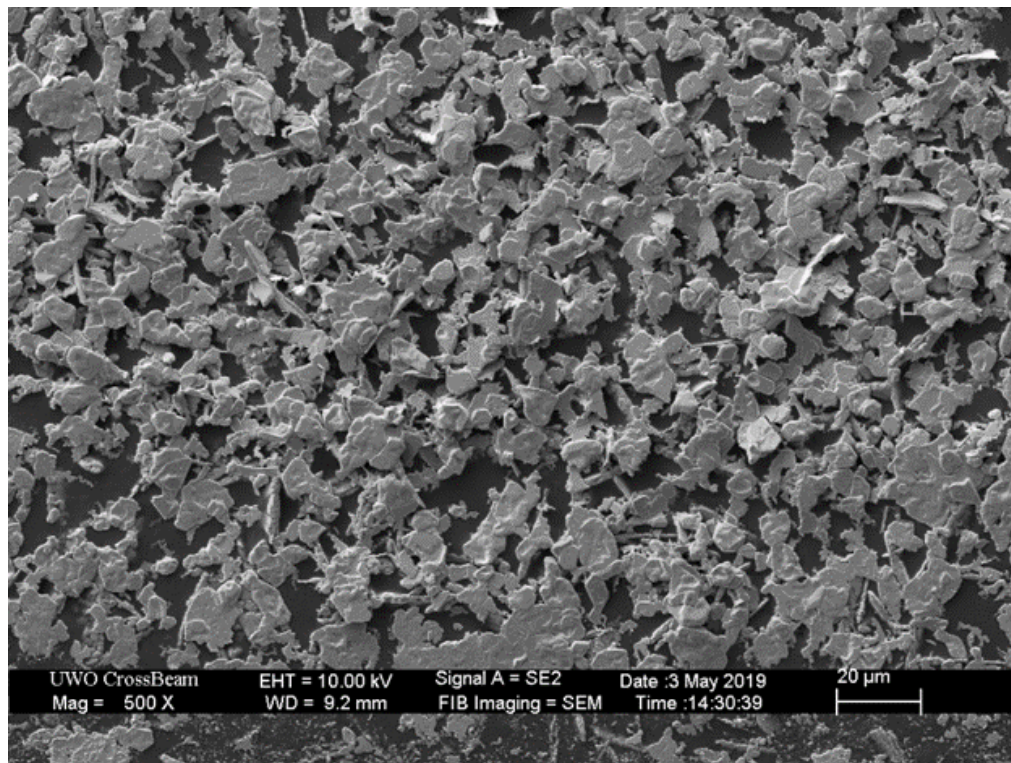


Figure 62 Surface morphology of the roll to roll printed metasurface sample.

3.3 Fabrication of metasurface EM wave absorber with 3D printing

3.3.1 Preparing of conductive PLA

Materials: PLA was purchase from Protoplant. Carbon nanotubes (CNTs) were purchased from Carbonrich graphene high technology company.

Equipment: Filament Extruder (Noztek Pro).



Figure 63 Noztek Pro filament Extruder

Process: every 100 g PLA was cut by grains with a length of 2 mm and mixed with CNTs with a mass ratio of 5%. For the mixing process, Noztek Pro Filament Extruder (**Figure 63**) was heated to 210 °C with a constant rotation speed of 200 rpm for 15 minutes. To achieve high homogeneity, the mixing process was repeated for 3 times. The filament was extruded with a diameter of 1.75 mm by the speed of 0.5 m/min (**Figure 64**).



Figure 64 Prepared conductive PLA filament

The prepared conductive PLA filament has a conductivity of 30 S/m. The conductivity stays stable after bending and washing.

3.3.2 Printing of conductive PLA

Equipment: Ender 3 Pro desktop 3D printer was purchase from Creality3D (**Figure 65**)

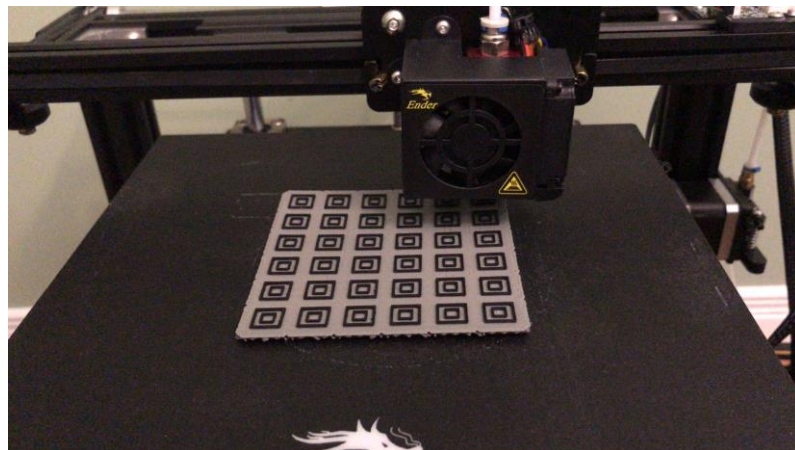


Figure 65 Printing process of Ender 3Pro desktop 3D printer

Printing: the printing head was heat to 200 °C, the printer substrate was cleaned and heat to 60 °C. The thickness of each layer is 0.2 mm. The printing speed is 40 mm/min.

3.3.3 Printed Metasurface EM wave absorber

The metasurface EM wave absorber, as a 6 by 6 array of the unit cell, was printed with a thickness of 0.8 mm, as the optimized parameter (**Figure 66**).

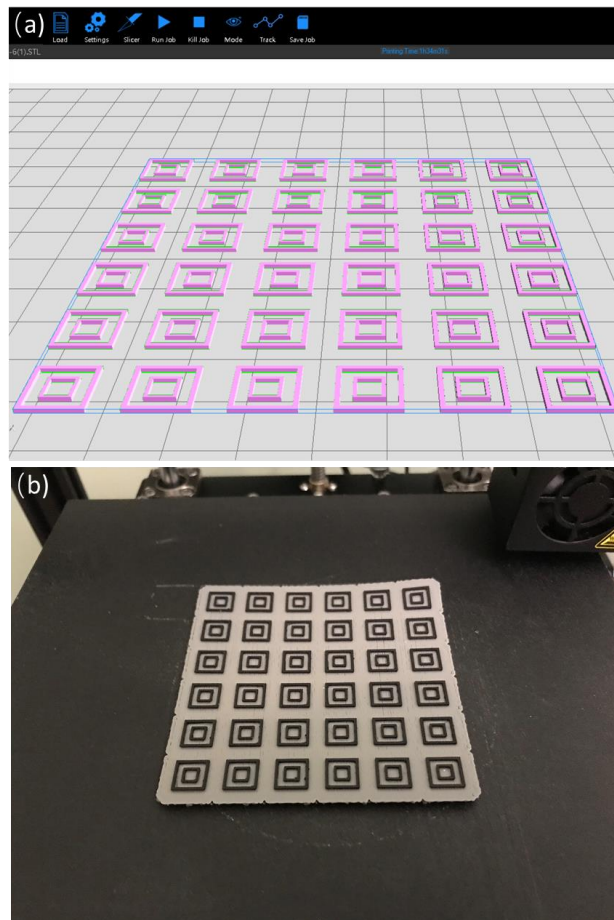


Figure 66 (a) 3D model and (b) printed metasurface EM wave absorber.

From the simulation results in chapter 2, an absorption performance of -17 dB can be expected at the designed resonance frequency. Compared with the traditional ways for the metasurface EM wave absorber, the 3D printing of the conductive polymer-CNTs composites has many advantages. First, the digitalization of the 3D printing creates great space for structure modification and printing parameters adjustment. Second, the conductivity of the conductive PLA can be controlled by changing the content of the CNTs. Third, all the operations in the whole process can be standardized. Large-scale production of the metasurface EM wave absorber can be realized rapidly. Forth, all the raw materials are low-cost and environmentally friendly. No waste was generated in the whole process.

Chapter 4

4. Performance and extended application of printed metasurface

In this chapter, the measurement results of the performance of the printed metasurface via vector network analyzer will be discussed. The novel application of the metasurface, like blood glucose concentration invasive detection and food safety supervision were proposed or demonstrate.

4.1 Measurement of EM wave selective reflection metasurface

4.1.1 Measurement setup

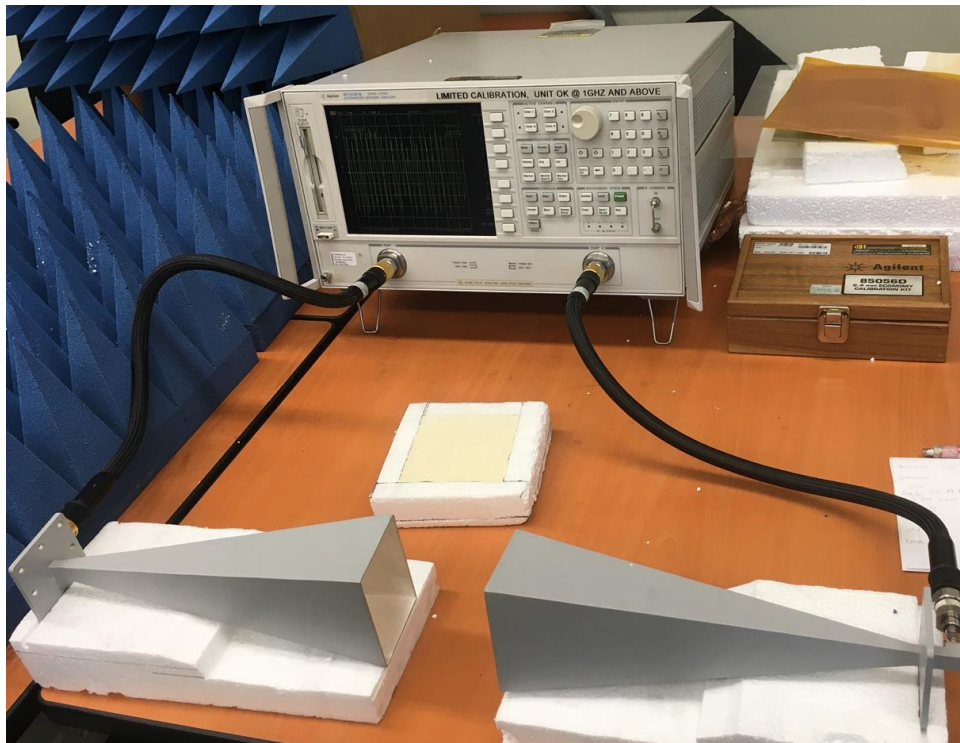


Figure 67 Measurement setup for the metasurface, including Agilent 8722ES vector network analyzer and a pair of the horn antenna.

In **Figure 67**, the Agilent 8720ES vector network analyzer integrates a microwave source, tuned-receiver, and transmission/reflection or S-parameter test. The available working

frequency for this equipment is 50 MHz to 40 GHz. The designed working temperature is 23 ± 3 °C. The uncertainty in transmission tracking is up to 0.05dB. The working frequency range of the waveguide Horn Antenna is 21.7-33 GHz. The center frequency of our metasurface is about 30 GHz. The feature of the horn antenna was provided in **Table 7** and **Figure 68**.

Table 7 Specific parameter of the horn antenna @Ta =25 °C

Parameter	Data
Frequency range	21.7-33 GHz
Gain	25 dB
Electrical specification	TA =25°
VSWR	1.5
Connector	2.92 k

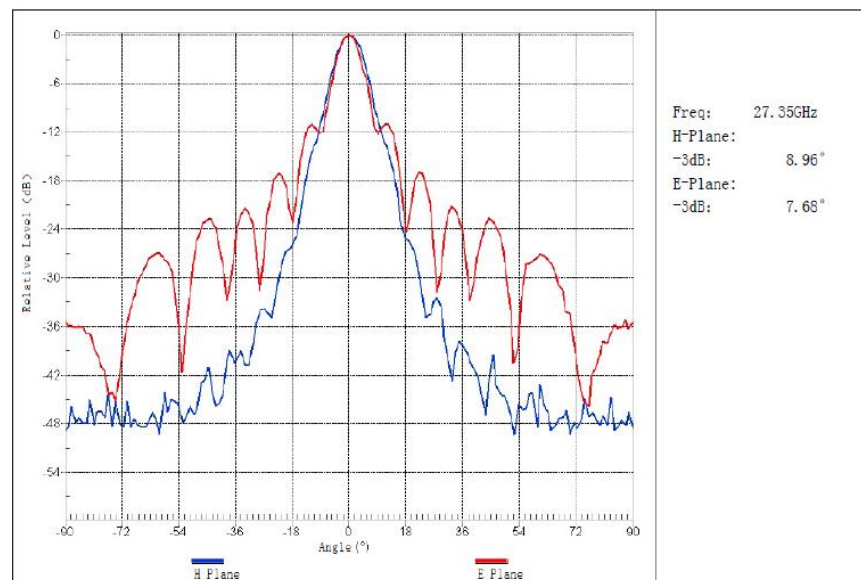


Figure 68 Radiation pattern in both E-plane and H-plane at 27.35 GHz

4.1.2 EM wave selective reflection performance of the printed metasurface

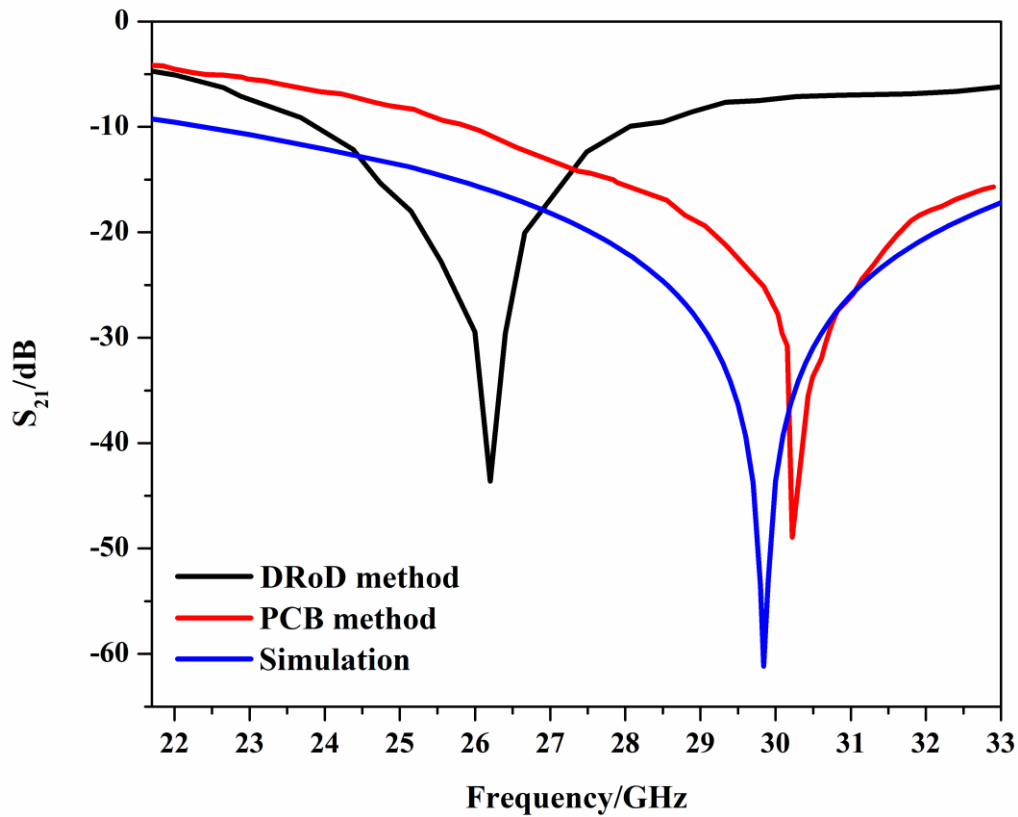


Figure 69 Comparison of S_{21} curve between the DRoD made sample, PCB made sample and simulation.

The EM wave selective reflection performance was measured by the network analyzer and horn antenna. The measured curves were fitted to eliminate the influence of background noise. To have a better comparison, we get the PCB method fabricated sample from the factory with the same design parameters. The resonate frequency of PCB made sample shifts slightly compared with the simulation results. But it proved that our simulation result is reasonable and the designed metasurface can work as a bandstop EM wave filter at 30 ± 1 GHz when all the parameters are ideal. Compared with PCB sample and simulation results, the DRoD printed samples had a smaller resonance frequency at 26.1 GHz, which is about 4 GHz left shift to that of simulation results, shown in Figure 69.

As a low price, portable printer, the accuracy of the Epson C88+ printer is not as high as the laser printer in the complex PCB process. The printing resolution limitation is the main reason to cause the resonance frequency shift. However, one of the most important advantages of inkjet printing is digitalization. We can print the pattern with different sizes through setting the printing parameter in the computer, without any additional hardware, like the new frame in screen printing or new Annilox cylinder in flexographic printing. According to the classical EM wave theory, we can infer that the left resonance frequency shift is induced by a wider line width than desired. To meet the designed resonance frequency, we take the strategy of reducing the printing size. The performance of the size modified sample was measured after printing. The best result was obtained when the printed metasurface is 80% of the original pattern size.

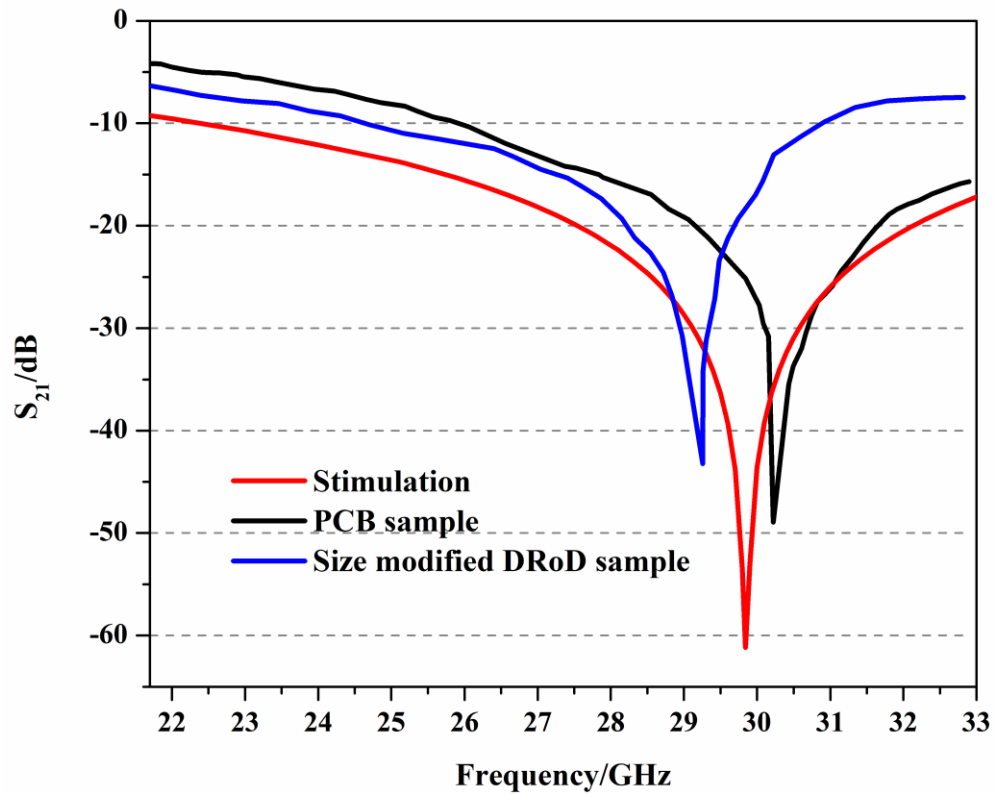


Figure 70 Comparison of S_{21} curve between size modified DRoD made sample, PCB made sample and simulation.

From **Figure 70**, the size modified sample fabricated via the DRoD method has a competitive performance with the PCB made sample. By reducing the metasurface to 80%

of the original size, the resonance frequency right shifts to the designed frequency effectively. Usually, -20 dB is the requirement transmission parameter to the EM wave filtering in the communication application. From the results, the DRoD printed sample with the peak S_{21} value of -43 dB was far beyond the required performance. For the right branch of the curve, the S_{21} parameter is approaching to -5 dB, which means such a structure can form a bandpass filter at the higher working frequency.

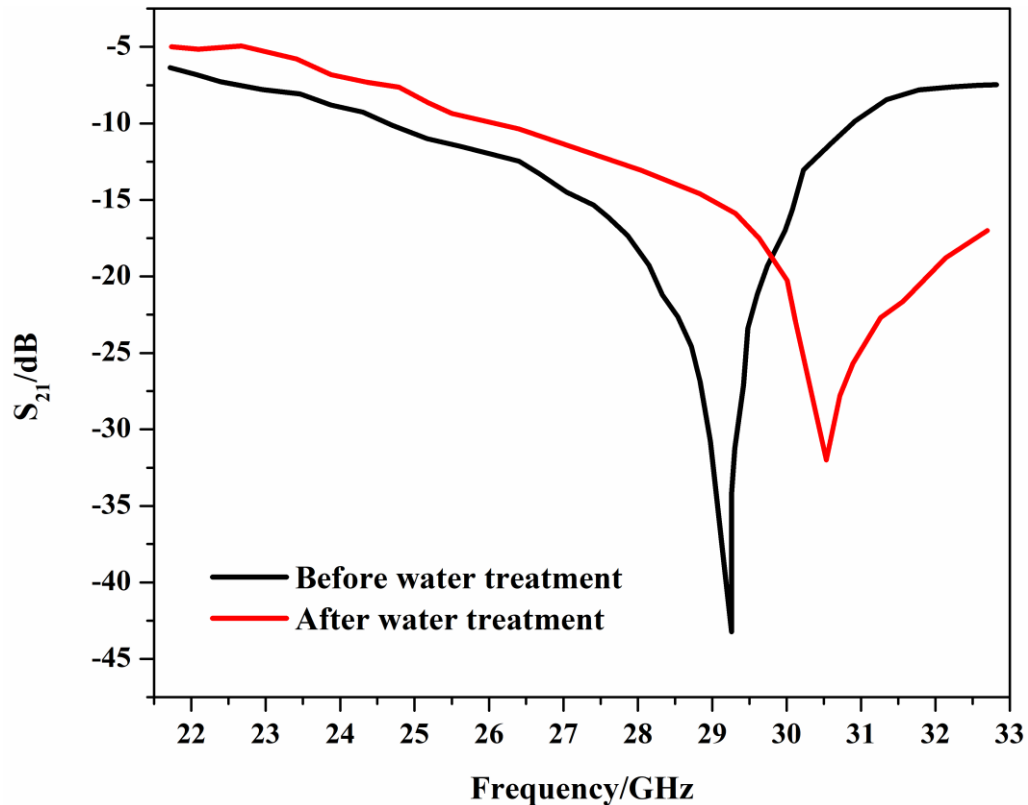


Figure 71 Comparison of S_{21} curve of size modified DRoD made sample before and after water treatment.

After the water treatment, the printed metasurface shows good stability in the conductivity. From **Figure 71**, we find the resonance frequency shift from 29.3 to 30.5 GHz after the process. The water treatment will increase the roughness because water treatment can trigger the reduction reaction and generate silver nanoparticles in random positions. The increase of the structure roughness can result in the resonance frequency shift in both sides. Since the resonance frequency of the PCB sample is 30.2 GHz, the DRoD sample after water treatment shows acceptable bandstop performance at desire working frequency. However,

compared with the transmission curve before the water treatment, the shape of the curve was flattened, which means the filtering selectivity decreased.

The DRoD method shows a strong ability of modification provides flexibility in the electronic device fabrication. High-performance metasurface was fabricated with low cost, simple process, fast prototype and high stability.

4.2 Applications of metasurface on food safety

In modern society, food safety is one of the most critical concerns in our daily life. A healthy life is based on healthy food. During the whole supply chain of the food, the quality of the food should be well monitored. Physical properties of food are critical for stability and stability is the key parameter for both consumers and industry. In many cases, food degradation is accompanied by the presence of water, which has a high dielectric constant. Metasurface can be applied to monitor the food component change via detecting the dielectric constant, which is a basic physical parameter of the food. The change of the dielectric constant will lead to the resonance frequency shift of the metasurface structure. To demonstrate this concept, we take rice and soft wheat as examples, which are vital food sources in the whole world. Water was added into the rice and soft wheat to simply simulate the water generation in the storage process. We can easily stick the DRoD method fabricated metasurface onto the food package. The resonance frequency will shift with the change of water content. By find the relationship between frequency shift and water content, we can have a new method to analyze food quality as a noninvasive approach.



Figure 72 Materials used in the test: (a) rice; (b) soft wheat; (c) food container; (d) metasurface.

All the food was purchase from *food basic*. In each sample, 500 g of rice (**Figure 72(a)**) and soft wheat (**Figure 72(b)**) was packed in the container individually. We measure the resonance shift the water content by adding water into the container (**Figure 72, (c)**) from 0 ml to 20 ml. Then, we plot the relationship between resonance frequency shift and water content. The linear fit was made to explore the possibility of inferring the water content from the resonate frequency.

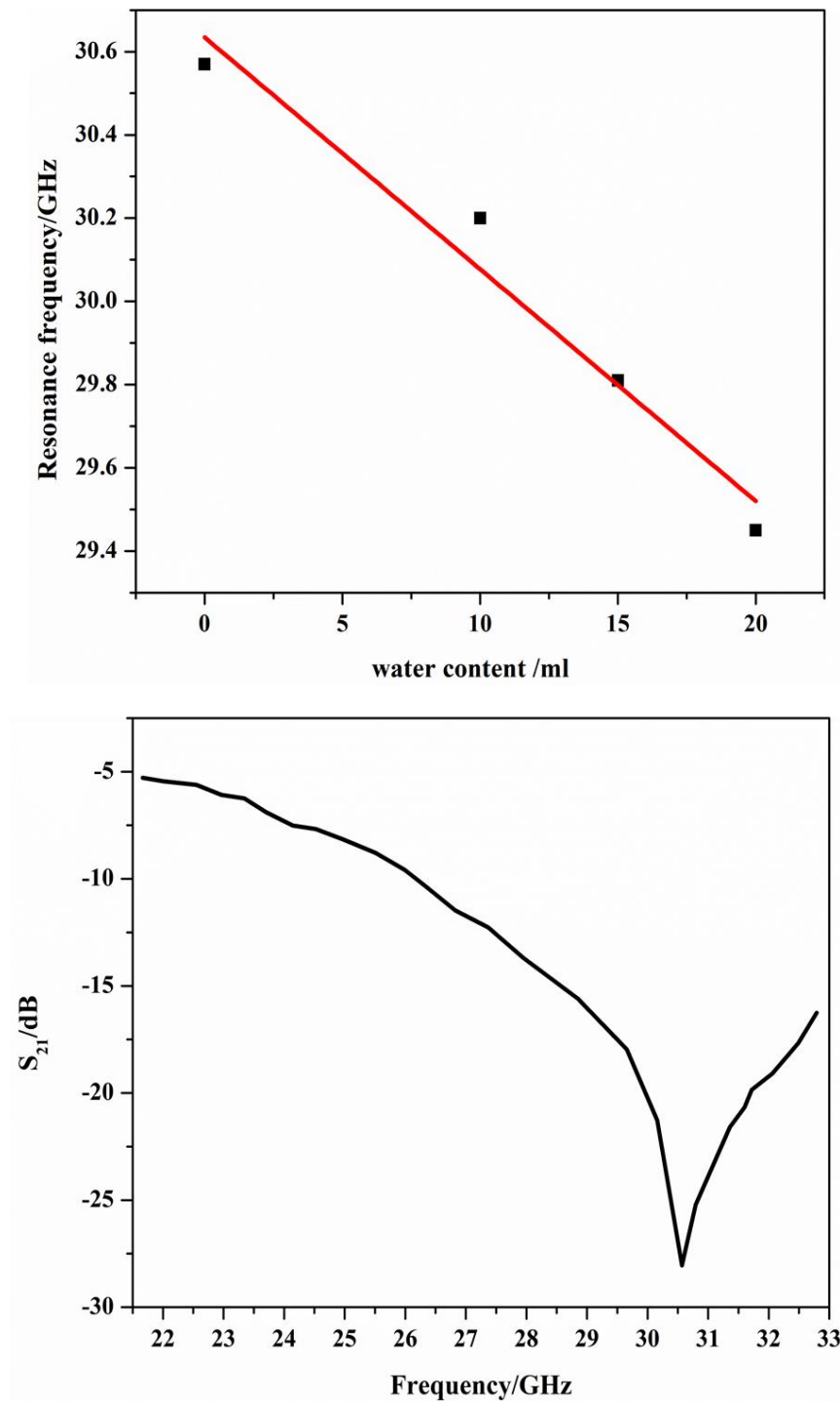


Figure 73 Resonance frequency shift for rice with the water content (up) and the S₂₁ parameter when 0 ml water was added (down).

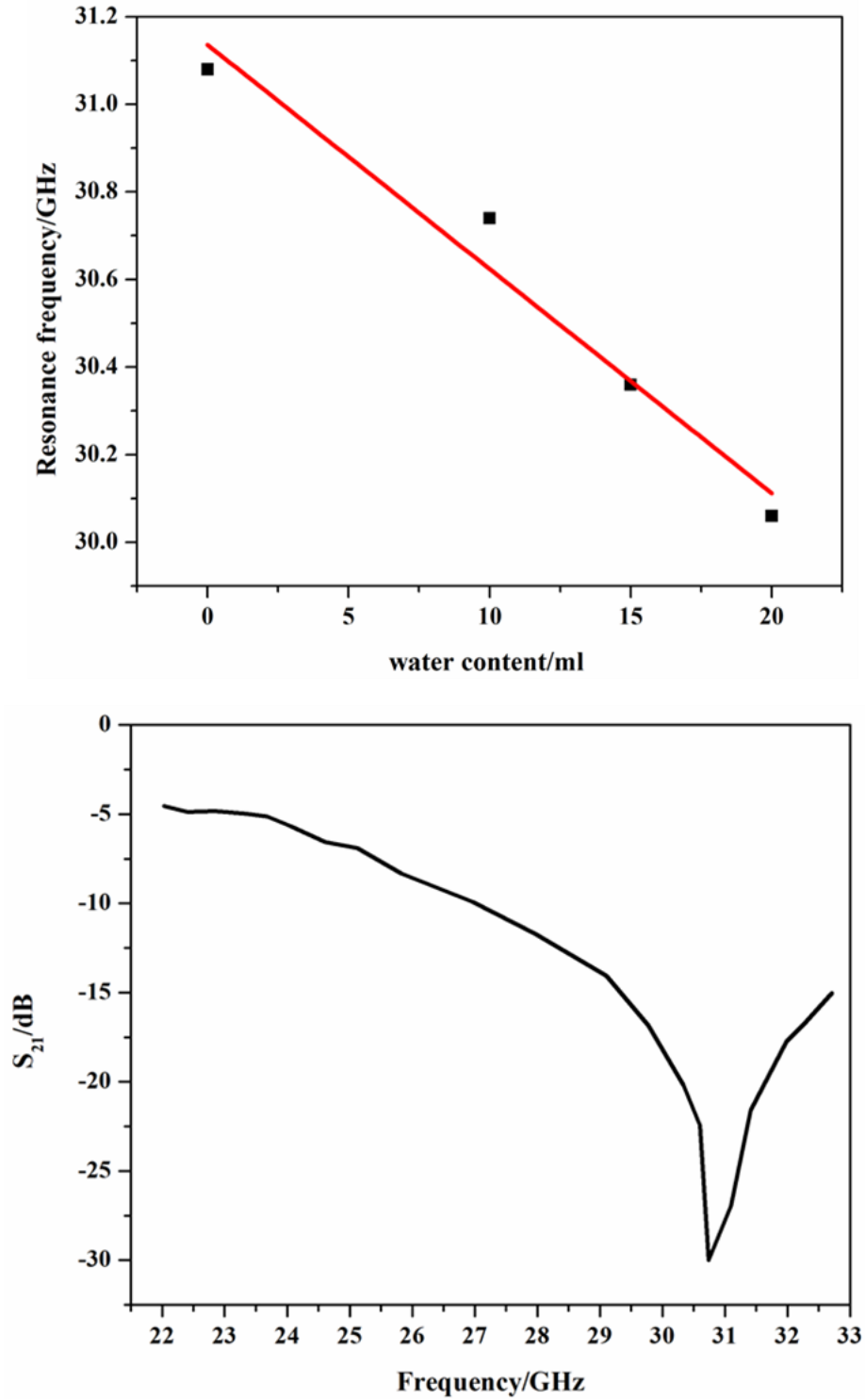


Figure 74 Resonance frequency shift for soft wheat with the water content (up) and the S_{21} parameter when 10 ml water was added (down).

In the range from 0 to 20 ml, a good linear relationship was found between the water loading and resonance frequency shift in both rice (**Figure 73**) and soft wheat (**Figure 74**) cases. For the linear fit, the standard error for the slope is 0.0075 for rice and 0.0066 for the soft wheat. In the whole measurement process, the S_{21} curve keeps a regular shape. With the increase of the water content, the dielectric constant will increase[73]. The resonance frequency of the metasurface measuring system will decrease with the increase of dielectric constant. From the results, our printed metasurface can contribute to the detect of the physical property food with the vector network analyzer based on the results above.

Catherine Bernou et al. developed a humidity sensor based on the microstrip line by measure the changing the dielectric constant of PI film will change in different humidity environments [74]. The resonance unit size of the microstrip line is large, so it mainly applied in the low-frequency range. The angular stability of the microstrip line is weaker than our meandered loop metasurface. A wider working frequency range and higher accuracy expand the application area. Ang Hu and Yonghan Fang measured the dielectric constant change of cement particles under different humidity based on the S-parameter test[75]. The sample preparation process is complex and the test equipment is expensive. The food spoilage process contains many chemical reactions. Many chemicals include, but more than water will be generated in the whole spoilage process. Metasurface with more resonance frequency can be designed and applied to make a better monitor in the actual food storage house or supply chain. It is a noninvasive method to detect the food's quality with the advantages of real-time analysis, simple operation and low cost.

The limitation of the method is that we still rely on the vector network analyzer to curve the frequency shift. The vector network analyzer is expensive. In the recent stage, such a method is possible only for the massive storage and delivery system. With the further development of EM wave frequency analyzer technology, such an approach will have more significant applications.

Chapter 5

5 Summary and perspective

5.1 Thesis summary

Printed electronics is a hot topic in research academic and industry field due to the great potential in the incoming future. A countless number of flexible and wearable electronic devices and equipment will be fabricated and applied, which will bring revolutionary changes in our lifestyles. Printed electronics is based on traditional printing technology with new method and applications are emerging almost every day. Metasurface or metamaterials as novel designed structure have shown their power in many areas. EM wave manipulation and materials detection are two of the most attractive applications. The fabrication of metasurface is still complicated, expensive and environmentally unfriendly by the traditional MEMS and PCB methods. DROD method is a simple, low cost, fast prototype and high-efficiency fabrication approach in the printed electronics field. In this thesis, the DROD method was applied to fabricate the high-performance selective reflection metasurface which can be used in EM wave filtering and the elimination of the EMI. The metasurface EM wave absorber was fabricated via 3D printing to form a complete EM wave manipulation system including the selective reflection and absorption. The application of the DROD printed metasurface was extended to monitoring food safety. We demonstrate the possibility to measure the resonance frequency shift to measure the water content difference, which is one of the critical values for food safety.

In chapter 1, the background of printed electronics and metasurface was introduced, including the mechanism, development, fabrication and applications.

In chapter 2, the numerical study of the metasurface was conducted. The geometry and parameters were optimized. The simulation results guided the fabrication and provided direction to understand the experiment results.

In chapter 3, the DROD method was proposed to fabricate the high-performance EM wave selective reflection metasurface. High loading silver ink was formulated to improve print

quality. Metasurface EM wave absorber was fabricated via 3D printing. The conductivity and stability of the printed metasurface were measured and evaluated.

In chapter 4, the EM wave filtering performance was measured via the vector network analyzer. The modification was made in the printing to overcome the limitation of the printer and meet the desired resonance frequency. The novel approach to monitoring food safety was proposed.

5.2 Perspective

The roll to roll printing of metasurface was demonstrated on the Epson C88+ printer. We can apply advanced inkjet printer to integrate the Mayer rod coating and IR heating as a whole roll to roll printing system (illustrated in Figure 75). The IR heating system can reduce drying time and avoid hurting the substrate. The fabrication of the metasurface can be conducted in a continuous process.

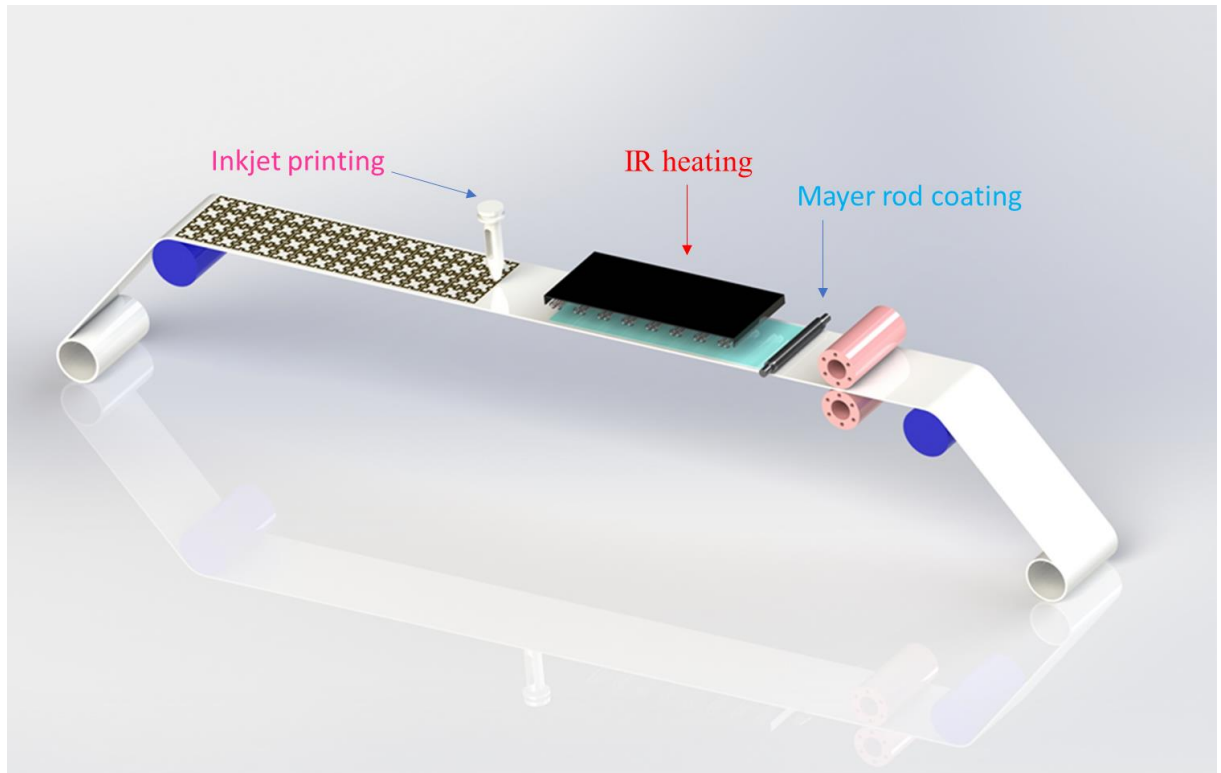


Figure 75 Roll to roll printing system based on DRoD method.

In this thesis, the function of the designed metasurface is EM bandstop element. In future research, we can design the metasurface structure with both bandstop and bandpass functions.

In the water treatment test, we realized that the cooperation of water can improve the conductivity of the printed metasurface. The control of water-assisted reaction can further promote the development of the DRoD method to reach the targets of high accuracy, high conductivity and multifunction.

Reference

- [1] Y. Zheng, Z. Z. He, J. Yang, and J. Liu, "Personal electronics printing via tapping mode composite liquid metal ink delivery and adhesion mechanism," *Sci. Rep.*, vol. 4, pp. 1–8, 2014, doi: 10.1038/srep04588.
- [2] K. Kim, B. Kim, and C. H. Lee, "Printing Flexible and Hybrid Electronics for Human Skin and Eye-Interfaced Health Monitoring Systems," *Adv. Mater.*, vol. 32, no. 15, pp. 1–22, 2020, doi: 10.1002/adma.201902051.
- [3] T. Zhang, X. Wang, T. Li, Q. Guo, and J. Yang, "Fabrication of flexible copper-based electronics with high-resolution and high-conductivity on paper via inkjet printing," *J. Mater. Chem. C*, vol. 2, no. 2, pp. 286–294, 2014, doi: 10.1039/c3tc31740d.
- [4] T. Zhang, X. Cai, J. Liu, M. Hu, Q. Guo, and J. Yang, "Facile Fabrication of Hybrid Copper-Fiber Conductive Features with Enhanced Durability and Ultralow Sheet Resistance for Low-Cost High-Performance Paper-Based Electronics," *Adv. Sustain. Syst.*, vol. 1, no. 9, p. 1700062, 2017, doi: 10.1002/adisu.201700062.
- [5] J. Perelaer *et al.*, "Printed electronics: The challenges involved in printing devices, interconnects, and contacts based on inorganic materials," *J. Mater. Chem.*, vol. 20, no. 39, pp. 8446–8453, 2010, doi: 10.1039/c0jm00264j.
- [6] J. H. Kim and S. Seo, "Fabrication of an imperceptible liquid metal electrode for triboelectric nanogenerator based on gallium alloys by contact printing," *Appl. Surf. Sci.*, vol. 509, no. January, p. 145353, 2020, doi: 10.1016/j.apsusc.2020.145353.
- [7] Y. Khan, A. Thielens, S. Muin, J. Ting, C. Baumbauer, and A. C. Arias, "A New Frontier of Printed Electronics: Flexible Hybrid Electronics," *Adv. Mater.*, vol. 32, no. 15, pp. 1–29, 2020, doi: 10.1002/adma.201905279.
- [8] B. W. Boudouris and S. Yee, "Structure, properties and applications of thermoelectric polymers," *J. Appl. Polym. Sci.*, vol. 134, no. 3, 2017, doi: 10.1002/app.44456.
- [9] W. Chang, T. Fang, H. Lin, Y. Shen, and Y. Lin, "A Large Area Flexible Array Sensors Using Screen Printing Technology," *Journal of Display Technology*, vol. 5, no. 6, pp. 178–183, 2009.
- [10] G. Cummins and M. P. Y. Desmulliez, "Inkjet printing of conductive materials: A review," *Circuit World*, vol. 38, no. 4, pp. 193–213, 2012, doi: 10.1108/03056121211280413.
- [11] C. Weber, "Zum Zerfall eines Flüssigkeitsstrahles," *ZAMM - J. Appl. Math. Mech. / Zeitschrift für Angew. Math. und Mech.*, vol. 11, no. 2, pp. 136–154, 1931, doi: 10.1002/zamm.19310110207.
- [12] H. Sirringhaus *et al.*, "High-resolution inkjet printing of all-polymer transistor circuits," *Science (80-.)*, vol. 290, no. 5499, pp. 2123–2126, 2000, doi: 10.1126/science.290.5499.2123.

- [13] C. Te Liu, W. H. Lee, and T. L. Shih, "Synthesis of ZnO nanoparticles to fabricate a mask-free thin-film transistor by inkjet printing," *J. Nanotechnol.*, vol. 2012, 2012, doi: 10.1155/2012/710908.
- [14] Y. L. Tai and Z. G. Yang, "Fabrication of paper-based conductive patterns for flexible electronics by direct-writing," *J. Mater. Chem.*, vol. 21, no. 16, pp. 5938–5943, 2011, doi: 10.1039/c0jm03065a.
- [15] A. Russo, B. Y. Ahn, J. J. Adams, E. B. Duoss, J. T. Bernhard, and J. A. Lewis, "Pen-on-paper flexible electronics," *Adv. Mater.*, vol. 23, no. 30, pp. 3426–3430, 2011, doi: 10.1002/adma.201101328.
- [16] K. G. Nair, D. Jayaseelan, and P. Biji, "Direct-writing of circuit interconnects on cellulose paper using ultra-long, silver nanowires based conducting ink," *RSC Adv.*, vol. 5, no. 93, pp. 76092–76100, 2015, doi: 10.1039/c5ra10837c.
- [17] H. Jia, J. Wang, X. Zhang, and Y. Wang, "Pen-writing polypyrrole arrays on paper for versatile cheap sensors," *ACS Macro Lett.*, vol. 3, no. 1, pp. 86–90, 2014, doi: 10.1021/mz400523x.
- [18] Y. Yu, J. Zhang, and J. Liu, "Biomedical Implementation of Liquid Metal Ink as Drawable ECG Electrode and Skin Circuit," *PLoS One*, vol. 8, no. 3, pp. 8–13, 2013, doi: 10.1371/journal.pone.0058771.
- [19] M. Hu, X. Cai, Q. Guo, B. Bian, T. Zhang, and J. Yang, "Direct pen writing of adhesive particle-free ultrahigh silver salt-loaded composite ink for stretchable circuits," *ACS Nano*, vol. 10, no. 1, pp. 396–404, 2016, doi: 10.1021/acsnano.5b05082.
- [20] Jennifer A. Lewis and B. Y. Ahn, "Three-dimensional printed electronics," *Nature*, vol. 518, pp. 42–43, 2015.
- [21] Y. L. Kong *et al.*, "3D printed quantum dot light-emitting diodes," *Nano Lett.*, vol. 14, no. 12, pp. 7017–7023, 2014, doi: 10.1021/nl5033292.
- [22] J. T. Muth *et al.*, "Embedded 3D printing of strain sensors within highly stretchable elastomers," *Adv. Mater.*, vol. 26, no. 36, pp. 6307–6312, 2014, doi: 10.1002/adma.201400334.
- [23] J. B. Pendry, D. Schurig, and D. R. Smith, "Controlling electromagnetic fields," *Science (80-.)*, vol. 312, no. 5781, pp. 1780–1782, 2006, doi: 10.1126/science.1125907.
- [24] L. Zhang, S. Mei, K. Huang, and C. W. Qiu, "Advances in Full Control of Electromagnetic Waves with Metasurfaces," *Adv. Opt. Mater.*, vol. 4, no. 6, pp. 818–833, 2016, doi: 10.1002/adom.201500690.
- [25] R. A. Shelby, D. R. Smith, and S. Schultz, "Experimental verification of a negative index of refraction," *Science (80-.)*, vol. 292, no. 5514, pp. 77–79, 2001, doi: 10.1126/science.1058847.
- [26] X. Huang, Y. Lai, Z. H. Hang, H. Zheng, and C. T. Chan, "Dirac cones induced by accidental degeneracy in photonic crystals and zero-refractive-index materials," *Nat. Mater.*, vol. 10, no. 8, pp. 582–586, 2011, doi: 10.1038/nmat3030.

- [27] R. W. Wood, "On a remarkable case of uneven distribution of light in a diffraction grating spectrum," *Proc. Phys. Soc. London*, vol. 18, no. 1, pp. 269–275, 1901, doi: 10.1088/1478-7814/18/1/325.
- [28] A. Hessel and A. A. Oliner, "A New Theory of Wood's Anomalies on Optical Gratings," *Appl. Opt.*, vol. 4, no. 10, p. 1275, 1965, doi: 10.1364/ao.4.001275.
- [29] Thomas B. A. Senior, "Approximate Boundary Conditions," *IEEE Trans. Antennas Propag.*, vol. 5, pp. 826–829, 1981, doi: 10.1007/978-94-007-2739-7_100029.
- [30] A. B. Numan and M. S. Sharawi, "Extraction of material parameters for metamaterials using a full-wave simulator [education column]," *IEEE Antennas Propag. Mag.*, vol. 55, no. 5, pp. 202–211, 2013, doi: 10.1109/MAP.2013.6735515.
- [31] S. Chen, Z. Li, Y. Zhang, H. Cheng, and J. Tian, "Phase Manipulation of Electromagnetic Waves with Metasurfaces and Its Applications in Nanophotonics," *Adv. Opt. Mater.*, vol. 6, no. 13, pp. 1–25, 2018, doi: 10.1002/adom.201800104.
- [32] X. Liu, M. Jia, X. Zhang, and W. Lu, "A Novel Multichannel Internet of Things Based on Dynamic Spectrum Sharing in 5G Communication," *IEEE Internet Things J.*, vol. 6, no. 4, pp. 5962–5970, 2019, doi: 10.1109/JIOT.2018.2847731.
- [33] D. Li *et al.*, "A Low-Profile Broadband Bandpass Frequency Selective Surface with Two Rapid Band Edges for 5G Near-Field Applications," *IEEE Trans. Electromagn. Compat.*, vol. 59, no. 2, pp. 670–676, 2017, doi: 10.1109/TEMC.2016.2634279.
- [34] A. Baniya, "Assessment of Frequency Selective Surface for Improving Indoor Cellular Network," Tampere University of Technology, 2014.
- [35] W. G. Whittow, Y. Li, R. Torah, K. Yang, S. Beeby, and J. Tudor, "Printed frequency selective surfaces on textiles," *Electron. Lett.*, vol. 50, no. 13, pp. 916–917, 2014, doi: 10.1049/el.2014.0955.
- [36] V. Sanchez-Romaguera *et al.*, "Inkjet printed paper based frequency selective surfaces and skin mounted RFID tags: The interrelation between silver nanoparticle ink, paper substrate and low temperature sintering technique," *J. Mater. Chem. C*, vol. 3, no. 9, pp. 2132–2140, 2015, doi: 10.1039/c4tc02693d.
- [37] J. Huo, L. Wang, and H. Yu, "Polymeric nanocomposites for electromagnetic wave absorption," *J. Mater. Sci.*, vol. 44, no. 15, pp. 3917–3927, 2009, doi: 10.1007/s10853-009-3561-1.
- [38] N. I. Landy, S. Sajuyigbe, J. J. Mock, D. R. Smith, and W. J. Padilla, "Perfect metamaterial absorber," *Phys. Rev. Lett.*, vol. 100, no. 20, pp. 1–4, 2008, doi: 10.1103/PhysRevLett.100.207402.
- [39] A. K. Azad *et al.*, "Metasurface Broadband Solar Absorber," *Sci. Rep.*, vol. 6, pp. 6–11, 2016, doi: 10.1038/srep20347.
- [40] W. Jiang *et al.*, "Electromagnetic wave absorption and compressive behavior of a

- three-dimensional metamaterial absorber based on 3D printed honeycomb,” *Sci. Rep.*, vol. 8, no. 1, pp. 1–7, 2018, doi: 10.1038/s41598-018-23286-6.
- [41] W. Xin, Z. Binzhen, W. Wanjun, W. Junlin, and D. Junping, “Design, Fabrication, and Characterization of a Flexible Dual-Band Metamaterial Absorber,” *IEEE Photonics J.*, vol. 9, no. 4, 2017, doi: 10.1109/JPHOT.2017.2722010.
- [42] Y. J. Yoo *et al.*, “Flexible and elastic metamaterial absorber for low frequency, based on small-size unit cell,” *Appl. Phys. Lett.*, vol. 105, no. 4, 2014, doi: 10.1063/1.4885095.
- [43] D. S. Wang, B. J. Chen, and C. H. Chan, “High-Selectivity Bandpass Frequency-Selective Surface in Terahertz Band,” *IEEE Trans. Terahertz Sci. Technol.*, vol. 6, no. 2, pp. 284–291, 2016, doi: 10.1109/TTHZ.2016.2526638.
- [44] J. Cai, C. Lv, and A. Watanabe, “Laser Direct Writing and Selective Metallization of Metallic Circuits for Integrated Wireless Devices,” *ACS Appl. Mater. Interfaces*, vol. 10, no. 1, pp. 915–924, 2018, doi: 10.1021/acsami.7b16558.
- [45] Z. Zhao *et al.*, “Multispectral optical metasurfaces enabled by achromatic phase transition,” *Sci. Rep.*, vol. 5, pp. 1–9, 2015, doi: 10.1038/srep15781.
- [46] J. Luo *et al.*, “Fabrication of anisotropically arrayed nano-slots metasurfaces using reflective plasmonic lithography,” *Nanoscale*, vol. 7, no. 44, pp. 18805–18812, 2015, doi: 10.1039/c5nr05153c.
- [47] P. Hallbjörner, “The significance of radiation efficiencies when using S-parameters to calculate the received signal correlation from two antennas,” *IEEE Antennas Wirel. Propag. Lett.*, vol. 4, no. 1, pp. 97–99, 2005, doi: 10.1109/LAWP.2005.845913.
- [48] L. Kong *et al.*, “Electromagnetic wave absorption properties of graphene modified with carbon nanotube/poly(dimethyl siloxane) composites,” *Carbon N. Y.*, vol. 73, pp. 185–193, 2014, doi: 10.1016/j.carbon.2014.02.054.
- [49] R. J. Langley and E. A. Parker, “Double-square frequency-selective surfaces and their equivalent circuit,” *Electron. Lett.*, vol. 19, no. 17, pp. 675–677, 1983, doi: 10.1049/el:19830460.
- [50] K. Bao, J. Zhou, L. Wang, A. Sun, Q. Zhang, and Y. Shen, “A 29-30GHz 64-element Active Phased array for 5G Application,” *IEEE MTT-S Int. Microw. Symp. Dig.*, vol. 2018-June, pp. 492–495, 2018, doi: 10.1109/MWSYM.2018.8439209.
- [51] H. C. Huang, Y. Wang, and X. Jian, “Influence Analysis of Popular Dielectric Materials for Cellular Phones on 5G mm-Wave Antenna Performance,” *2019 Int. Work. Antenna Technol. iWAT 2019*, no. 255, pp. 77–80, 2019, doi: 10.1109/IWAT.2019.8730815.
- [52] H. Ullah, F. A. Tahir, and M. El-Hadidy, “FSS based Hexo-Fractal Dual Passband Filter for 28 and 380Hz 5G Millimeter-Wave Communications,” *2018 IEEE Antennas Propag. Soc. Int. Symp. Usn. Natl. Radio Sci. Meet. APSURSI 2018 - Proc.*, pp. 2365–2366, 2018, doi: 10.1109/APUSNCURSINRSM.2018.8608229.

- [53] S. Maci, M. Caiazzo, A. Cucini, and M. Casaletti, "A Pole-zero matching method for EBG surfaces composed of a dipole FSS printed on a grounded dielectric slab," *IEEE Trans. Antennas Propag.*, vol. 53, no. 1 I, pp. 70–81, 2005, doi: 10.1109/TAP.2004.840520.
- [54] D. Ferreira, I. Cuinas, R. F. S. Caldeirinha, and T. R. Fernandes, "3-D Mechanically tunable square slot FSS," *IEEE Trans. Antennas Propag.*, vol. 65, no. 1, pp. 242–250, 2017, doi: 10.1109/TAP.2016.2631131.
- [55] S. Khajevandi, H. Oraizi, and M. Poordaraee, "Design of planar dual-bandstop FSS using square-loop-enclosing superformula curves," *IEEE Antennas Wirel. Propag. Lett.*, vol. 17, no. 5, pp. 731–734, 2018, doi: 10.1109/LAWP.2018.2812698.
- [56] M. Hosseini and M. Hakkak, "Characteristics estimation for jerusalem cross-based artificial magnetic conductors," *IEEE Antennas Wirel. Propag. Lett.*, vol. 7, pp. 58–61, 2008, doi: 10.1109/LAWP.2008.917605.
- [57] S. Perhirin and Y. Auffret, "A low consumption electronic system developed for a 10km long all-optical extension dedicated to sea floor observatories using power-over-fiber technology and SPI protocol," *Microw. Opt. Technol. Lett.*, vol. 55, no. 11, pp. 2562–2568, 2013, doi: 10.1002/mop.
- [58] E. A. Parker and A. N. A. El Sheikh, "Convolved array elements and reduced size unit cells for frequency-selective surfaces," *IEE Proc. H Microwaves, Antennas Propag.*, vol. 138, no. 1, pp. 19–22, 1991, doi: 10.1049/ip-h-2.1991.0004.
- [59] X. D. Hu, X. L. Zhou, L. S. Wu, L. Zhou, and W. Y. Yin, "A novel dual-band frequency selective surface (FSS)," *APMC 2009 - Asia Pacific Microw. Conf. 2009*, vol. 1, no. c, pp. 1227–1230, 2009, doi: 10.1109/APMC.2009.5384433.
- [60] A. Chauraya *et al.*, "Inkjet printed dipole antennas on textiles for wearable communications," *IET Microwaves, Antennas Propag.*, vol. 7, no. 9, pp. 760–767, 2013, doi: 10.1049/iet-map.2013.0076.
- [61] W. Yin, D. H. Lee, J. Choi, C. Park, and S. M. Cho, "Screen printing of silver nanoparticle suspension for metal interconnects," *Korean J. Chem. Eng.*, vol. 25, no. 6, pp. 1358–1361, 2008, doi: 10.1007/s11814-008-0223-y.
- [62] A. Chiolerio *et al.*, "Inkjet printing and low power laser annealing of silver nanoparticle traces for the realization of low resistivity lines for flexible electronics," *Microelectron. Eng.*, vol. 88, no. 8, pp. 2481–2483, 2011, doi: 10.1016/j.mee.2010.12.099.
- [63] D. Wakuda, M. Hatamura, and K. Suganuma, "Novel method for room temperature sintering of Ag nanoparticle paste in air," *Chem. Phys. Lett.*, vol. 441, no. 4–6, pp. 305–308, 2007, doi: 10.1016/j.cplett.2007.05.033.
- [64] T. Zhang, J. Li, J. Liu, and J. Yang, "React-on-Demand (RoD) Fabrication of Highly Conductive Metal–Polymer Hybrid Structure for Flexible Electronics via One-Step Direct Writing or Printing," *Adv. Funct. Mater.*, vol. 28, no. 4, pp. 1–11, 2018, doi: 10.1002/adfm.201704671.

- [65] T. Zhang, X. Li, E. Asher, S. Deng, X. Sun, and J. Yang, "Paper with Power: Engraving 2D Materials on 3D Structures for Printed, High-Performance, Binder-Free, and All-Solid-State Supercapacitors," *Adv. Funct. Mater.*, vol. 28, no. 37, pp. 1–12, 2018, doi: 10.1002/adfm.201803600.
- [66] B. M. Amoli, S. Gumfekar, A. Hu, Y. N. Zhou, and B. Zhao, "Thiocarboxylate functionalization of silver nanoparticles: Effect of chain length on the electrical conductivity of nanoparticles and their polymer composites," *J. Mater. Chem.*, vol. 22, no. 37, pp. 20048–20056, 2012, doi: 10.1039/c2jm33280a.
- [67] Y. Levin and J. E. Flores-Mena, "Surface tension of strong electrolytes," *Europhys. Lett.*, vol. 56, no. 2, pp. 187–192, 2001, doi: 10.1038/140464b0.
- [68] Y. F. Liu, M. H. Tsai, Y. F. Pai, and W. S. Hwang, "Control of droplet formation by operating waveform for inks with various viscosities in piezoelectric inkjet printing," *Appl. Phys. A Mater. Sci. Process.*, vol. 111, no. 2, pp. 509–516, 2013, doi: 10.1007/s00339-013-7569-7.
- [69] M. J. Qazi, R. W. Liefferink, S. J. Schlegel, E. H. G. Backus, D. Bonn, and N. Shahidzadeh, "Influence of Surfactants on Sodium Chloride Crystallization in Confinement," *Langmuir*, vol. 33, no. 17, pp. 4260–4268, 2017, doi: 10.1021/acs.langmuir.7b00244.
- [70] Y. Huang, J. Chen, Z. Yin, and Y. Xiong, "Roll-to-roll processing of flexible heterogeneous electronics with low interfacial residual stress," *IEEE Trans. Compon., Packag. Manuf. Technol.*, vol. 1, no. 9, pp. 1368–1377, 2011, doi: 10.1109/TCPMT.2011.2157692.
- [71] M. Hösel *et al.*, "High-volume processed, ITO-free superstrates and substrates for roll-to-roll development of organic electronics," *Adv. Sci.*, vol. 1, no. 1, pp. 1–12, 2014, doi: 10.1002/advs.201400002.
- [72] Z. P. Yin, Y. A. Huang, N. Bin Bu, X. M. Wang, and Y. L. Xiong, "Inkjet printing for flexible electronics: Materials, processes and equipments," *Chinese Sci. Bull.*, vol. 55, no. 30, pp. 3383–3407, 2010, doi: 10.1007/s11434-010-3251-y.
- [73] S. J. Park, S. A. N. Yoon, and Y. H. Ahn, "Dielectric constant measurements of thin films and liquids using terahertz metamaterials," *RSC Adv.*, vol. 6, no. 73, pp. 69381–69386, 2016, doi: 10.1039/c6ra11777e.
- [74] C. Bernou, D. Rebière, and J. Pistré, "Microwave sensors: a new sensing principle. Application to humidity detection," *Sensors Actuators, B Chem.*, vol. 68, no. 1, pp. 88–93, 2000, doi: 10.1016/S0925-4005(00)00466-4.
- [75] A. Hu, Y. Fang, J. F. Young, and Y. J. Oh, "Humidity dependence of apparent dielectric constant for DSP cement materials at high frequencies," *J. Am. Ceram. Soc.*, vol. 82, no. 7, pp. 1741–1747, 1999, doi: 10.1111/j.1151-2916.1999.tb01994.x.

Curriculum Vitae

Name: Jishu Gao

Post-secondary Education and Degrees: South University of Science and Technology of China
Shenzhen, Guangdong, China
2014-2018 B.A.

The University of Western Ontario
London, Ontario, Canada
2018-2020 M.E.Sc

Honours and Awards: Western Graduate Research Scholarship
2018-2020

Related Work Experience

Teaching Assistant
The University of Western Ontario
2019-2020

Research Assistant
The University of Western Ontario
2018-2020